

INFORMATION TO USERS

This manuscript has been reproduced from the microfilm master. UMI films the text directly from the original or copy submitted. Thus, some thesis and dissertation copies are in typewriter face, while others may be from any type of computer printer.

The quality of this reproduction is dependent upon the quality of the copy submitted. Broken or indistinct print, colored or poor quality illustrations and photographs, print bleedthrough, substandard margins, and improper alignment can adversely affect reproduction.

In the unlikely event that the author did not send UMI a complete manuscript and there are missing pages, these will be noted. Also, if unauthorized copyright material had to be removed, a note will indicate the deletion.

Oversize materials (e.g., maps, drawings, charts) are reproduced by sectioning the original, beginning at the upper left-hand corner and continuing from left to right in equal sections with small overlaps.

Photographs included in the original manuscript have been reproduced xerographically in this copy. Higher quality 6" x 9" black and white photographic prints are available for any photographs or illustrations appearing in this copy for an additional charge. Contact UMI directly to order.

**Bell & Howell Information and Learning
300 North Zeeb Road, Ann Arbor, MI 48106-1346 USA
800-521-0600**

UMI[®]

Antiprotons and other nuclear matters

by

Brett Steven Fadem

**A dissertation submitted to the graduate faculty
in partial fulfillment of the requirements for the degree of
DOCTOR OF PHILOSOPHY**

Major: Nuclear Physics

Program of Study Committee:

John C. Hill, Major Professor

John Lajoie

Marzia Rosati

David Carter Lewis

Jianwei Qiu

Gary Tuttle

Iowa State University

Ames, Iowa

2002

Copyright © Brett Steven Fadem, 2002. All rights reserved.

UMI Number: 3051460

UMI[®]

UMI Microform 3051460

Copyright 2002 by ProQuest Information and Learning Company.
All rights reserved. This microform edition is protected against
unauthorized copying under Title 17, United States Code.

ProQuest Information and Learning Company
300 North Zeeb Road
P.O. Box 1346
Ann Arbor, MI 48106-1346

**Graduate College
Iowa State University**

**This is to certify that the Doctoral dissertation of
Brett Steven Fadem
has met the dissertation requirements of Iowa State University**

Signature was redacted for privacy.

Major Professor

Signature was redacted for privacy.

For the Major Program

DEDICATION

Buddhists teach that one of the most basic truths is that suffering is unavoidable, and while I find the validity of this observation indisputable, it also serves to remind me of the opposite. Happiness is sometimes also unavoidable, and I credit my relationship with my mother for much of the happiness I have experienced.

My daughter lives far away, but she is always in my heart. Since I can't always be there for her, I hope that whatever little I am able to accomplish will serve to inspire her in some way.

I never would have gone to college had it not been for Roy and Ute Tellini. They took me under their wing and paid for the excellent (and very expensive) education I received at Grinnell College. I can never thank them enough for their love and support. Obviously, this thesis, and my graduate education would never have existed without them.

So, I dedicate my thesis to my mother, my daughter, and Roy and Ute Tellini.

TABLE OF CONTENTS

ABSTRACT	xvii
CHAPTER 1. OVERVIEW	1
1.1 Introduction: \bar{p} 's in the Context of Relativistic Heavy Ion Collisions.	1
1.1.1 Relativistic heavy ion physics.	1
1.1.2 The quark-gluon plasma.	3
1.1.3 Quantifying collective effects	5
1.1.4 Antiprotons in particular	7
1.2 Measured Distributions	9
1.3 Experimental Overview	13
1.4 Previous Measurements and Other Experimental Results	14
1.4.1 Prominent accelerators and colliders	14
1.4.2 BEVALAC data for sub-threshold \bar{p} production.	16
1.4.3 BNL-AGS experiment E802 and CERN Allaby data.	17
1.4.4 Other older experiments and analysis.	21
1.4.5 E910	22
CHAPTER 2. THE EXPERIMENT	24
2.1 The Alternating Gradient Synchrotron	24
2.2 Layout	25
2.2.1 Coordinate system	26
2.3 Detectors	28
2.3.1 Magnets, collimator and plug	28
2.3.2 Beam counters	31

2.3.3	Straw tubes	32
2.3.4	Hodoscopes	34
2.3.5	Calorimeter	36
2.4	Trigger	38
2.5	Data Acquisition System	40
2.6	Design and Construction of MULT	44
CHAPTER 3.	CALIBRATIONS	49
3.1	Introduction.	49
3.1.1	Computing	49
3.2	Time of Flight Calibrations Using the Tracking System	50
3.2.1	ADC pedestals for hodoscopes and beam counters	51
3.2.2	Slew time offset corrections for hodoscopes and beam counters	51
3.2.3	Time zero calibrations for hodoscopes	53
3.3	Y Offset Calibrations for Hodoscopes	55
3.4	Steps Used to Derive the Calibration Constants	55
CHAPTER 4.	INVARIANT MULTIPLICITIES	58
4.1	Reconstructing Tracks and Determining Masses.	58
4.2	Creating Ntuples.	59
4.2.1	Charge.	59
4.2.2	Quality of the track fit.	60
4.2.3	Kinematic cuts	61
4.2.4	Calorimeter cuts	64
4.2.5	Sample mass plot from the ntuples	64
4.3	Mass Histograms and Peak Fitting	64
4.3.1	Fitting the mass peaks	66
4.4	Corrections	84
4.4.1	Events sampled	86
4.4.2	Delta ray corrections: $\frac{N_d}{N}$	87

4.4.3	Empty target correction.	88
4.4.4	Acceptance and efficiency corrections.	88
4.5	Invariant Multiplicities.	90
CHAPTER 5. MODELING RESULTS		97
5.1	Quantifying Annihilation.	97
5.2	Modeling the Absolute p+Be Yield	101
CHAPTER 6. DISCUSSION AND CONCLUSIONS		105
6.1	Energy Dependence.	105
6.2	Target Dependence in p-A.	107
6.3	Antiproton Production and Annihilation in A-A.	108
6.4	Conclusions	113
BIBLIOGRAPHY		114
ACKNOWLEDGEMENTS		117

LIST OF TABLES

Table 1.1	Events sampled as a function of target. The 12 GeV/c Cu data were not analyzed for the purposes of this thesis, so that row was marked N/A.	13
Table 1.2	Typical operating energies for the BEVALAC, AGS, SPS, and the RHIC collider. Since these accelerators usually used heavy ion beams, the momenta and energies listed are per nucleon.	15
Table 1.3	E802 results: Multiplicity densities and particle ratios. Columns 2, 3, and 4 give $\frac{dn}{dy}$ for π^- , K^- , and \bar{p} production in the fiducial rapidity interval obtained from the average p_T procedure (see text). The last two columns quote the $\frac{dn}{dy}$ ratios between \bar{p} and π^- and \bar{p} and K^- in the fiducial rapidity interval.	19
Table 1.4	Allaby data, dn/dy , for 19.2 GeV/c protons incident upon targets of Be and Pb. These numbers were obtained by reading off the plot in Fig. 3 in reference (12).	20
Table 2.1	Particle species whose acceptance is optimized by the above field settings.	31
Table 2.2	Specifications for the straw chambers.	34
Table 2.3	Hodoscope slat dimensions.	36
Table 2.4	Summary of calorimeter characteristics and performance. Table reproduced from reference(25). See this reference and Reference (26) for details on construction and performance and for a complete explanation of the quantities in the table.	39

Table 4.1	χ^2 cuts. Most tracks put hits in 5 detectors. Since only two detector hits are required for a linear fit, the number of degrees of freedom in the fits were equal to the number of detectors used minus the 2 points needed for fitting. The χ^2 cuts were set at 3 for all of the fits except y vs. pathlength. This cut was loose because it was not independent of the other 3 χ^2 cuts.	61
Table 4.2	Table showing maximum beta for each y and p_T . Notice that the beta cut placed on the ntuple 0.9995 exceeds the kinematic range in which β was measured.	64
Table 4.3	Second round cuts, namely those performed at the time of the creation of mass histograms.	66
Table 4.4	Invariant multiplicities for the three targets analyzed at a 19 GeV/c beam momentum: Pb, Cu, and Be. For each invariant multiplicity listed, the statistical error and lower and upper systematic errors are also listed. The invariant multiplicities and errors are multiplied by 10^4 in units of GeV^{-2}	91
Table 4.5	Invariant multiplicities for the Be target at 12 GeV/c. The invariant multiplicities, statistic, and lower and upper systematic errors are quoted. All numbers are multiplied by 10^5 in units of GeV^{-2}	92
Table 5.1	Model calculated total inelastic cross sections as compared to those found in the literature.	100
Table 5.2	\bar{p} -nucleon in medium annihilation cross section. The error bars of the experimental ratio are not carried through. The model prediction errors listed are simply the errors on fitting the particular experimental ratios to within 0.02.	101

Table 6.1	Energy scaling for the \bar{p} cross section in E941 p-Be data, and the predicted scaling using Eqn. 6.1 and Eqn. 6.2. Due to some uncertainty in the E941 beam momentum, scaling for both 12 GeV/c to 19 GeV/c and 11.5 GeV/c to 19 GeV/c are given. Since E941 does not measure the cross section but rather the differential cross section, the E941 data were compared at $\frac{y}{y_{beam}} = 0.57$, and $p_T = 125$ MeV/c for both the 19 and 12 GeV/c beam data.	106
-----------	---	-----

LIST OF FIGURES

Figure 1.1	Contemporary phase diagram of nuclear matter.	4
Figure 1.2	Phase space coverage of E941 and some other experiments. The boxed region represents E941's coverage. Note that just because data points overlap those of E941's coverage, they are not necessarily comparable because they were not, in general obtained, using the same beam momenta.	23
Figure 2.1	Perspective view of the E941 spectrometer. The vacuum tank and the upstream beam counters are not shown.	25
Figure 2.2	Plan and elevation views of the E941 spectrometer. The vacuum tank and the upstream beam counters are not shown.	27
Figure 2.3	A close up elevation view of the region of the magnets, collimator and plug.	29
Figure 2.4	A close up plan view of the region of the magnets, collimator and plug.	30
Figure 2.5	Drawing of a straw tube station. Each station consisted of three planes	33
Figure 2.6	One slat of the hodoscopes.	35
Figure 2.7	Part of the array of slats on hodoscope H1.	37
Figure 2.8	E941 pre-trigger logic diagram.	41
Figure 2.9	E941 trigger logic diagram continued.	42
Figure 2.10	Data acquisition system configuration.	45
Figure 2.11	Specifications for the scintillator and lucite light pipe from one MULT quadrant. The units on the specifications are in inches.	47

Figure 2.12	Specifications for one entire MULT quadrant, including the photomultiplier tube and base. The bases were spring loaded and came equipped with soft iron casings to surround the PMT's and part of the light pipe.	48
Figure 3.1	This is a plot of the mean TDC values from top and bottom phototubes of the MITCH detector. The TDC values for each tube were first "slew" corrected. The next step consisted of determining offsets for each tube that would shift the mean position to 0. This calibration constant was referred to as the MITCH "slew time offsets". The word slew is included because the TDC values were slew corrected.	52
Figure 3.2	The schematic above illustrates how the fixed time of two features of the TDC spectra was used to calibrate runs with respect to each other. The raw values were corrected for "slewing" effects, and for run to run variations in the signal transit times between the detectors and the TDC electronics. The peaks of the mean TDC spectra were shifted to zero. Once the offset for the distributions was determined, it remained to determine the value of a new constant that when added to the slew corrected slew time offset corrected hit TDC's, yielded a number proportional to the time of flight.	54
Figure 3.3	This figure shows the 60 Hz noise on the the MITCH beam counter. ADC values from pedestal events are binned according to the phase of the cycle in which the event was taken. Similar noise affected the MULT counter ADC readouts.	57
Figure 4.1	Plots of χ^2 distributions of fits to tracks from one ntuple containing tracks from the Pb, 19 GeV/c, -0.2 T data.	62
Figure 4.2	Comparison of the vertical position of tracks at the location of the target in an ntuple (y-pl intercept) before final cuts and after final cuts.	63

Figure 4.3	Typical mass plot of the combined Be data at 19 GeV/c. The \bar{p} , kaon, and (truncated) pion peaks are easily discerned.	65
Figure 4.4	Mass histograms and fits for \bar{p} 's with rapidities from 1.4-1.6. The plot on the top is for $p_T = 50-100$ MeV/c. The plot on the bottom is for $p_T = 100-150$ MeV/c. These fits are for the 19 GeV/c, -0.2 T data with the Pb target.	68
Figure 4.5	Mass histograms and fits for \bar{p} 's with rapidities from 1.6-1.8. The plot on the top is for $p_T = 50-100$ MeV/c. The middle plot is for $p_T = 100-150$ MeV/c, and the bottom plot is for $p_T = 150-200$ MeV/c. These fits are for the 19 GeV/c, -0.2 T data with the Pb target.	69
Figure 4.6	Mass histograms and fits for \bar{p} 's with rapidities from 1.8-2.0 and transverse momenta of 50-100 MeV/c through 300-350 MeV/c in 50 MeV/c increments. These fits are for the 19 GeV/c, -0.2 T data with the Pb target.	70
Figure 4.7	Mass histograms and fits for \bar{p} 's with rapidities from 2.0-2.2 and transverse momenta of 50-100 MeV/c through 300-350 MeV/c in 50 MeV/c increments. These fits are for the 19 GeV/c, -0.2 T data with the Pb target.	71
Figure 4.8	Mass histograms and fits for \bar{p} 's with rapidities from 2.2-2.4 and transverse momenta of 50-100 MeV/c through 300-350 MeV/c in 50 MeV/c increments. These fits are for the 19 GeV/c, -0.2 T data with the Pb target.	72
Figure 4.9	Mass histograms and fits for \bar{p} 's with rapidities from 1.4-1.6 and transverse momenta of 50-100 MeV/c and 100-150 MeV/c. These fits are for the 19 GeV/c, -0.2 T data with the Be target.	73
Figure 4.10	Mass histograms and fits for \bar{p} 's with rapidities from 1.6-1.8 and transverse momenta of 50-100 MeV/c, 100-150 MeV/c, and 150-200 MeV/c. These fits are for the 19 GeV/c, -0.2 T data with the Be target.	74

Figure 4.11	Mass histograms and fits for \bar{p} 's with rapidities from 1.8-2.0 and transverse momenta of 50-100 MeV/c through 300-350 MeV/c in 50 MeV/c increments. These fits are for the 19 GeV/c, -0.2 T data with the Be target.	75
Figure 4.12	Mass histograms and fits for \bar{p} 's with rapidities from 2.0-2.2 and transverse momenta of 50-100 MeV/c through 300-350 MeV/c in 50 MeV/c increments. These fits are for the 19 GeV/c, -0.2 T data with the Be target.	76
Figure 4.13	Mass histograms and fits for \bar{p} 's with rapidities from 2.2-2.4 and transverse momenta of 50-100 MeV/c through 300-350 MeV/c in 50 MeV/c increments. These fits are for the 19 GeV/c, -0.2 T data with the Be target.	77
Figure 4.14	Mass histograms and fits for \bar{p} 's with rapidities from 1.4-1.6 and transverse momenta of 50-100 MeV/c and 100-150 MeV/c. These fits are for the 12 GeV/c, -0.2 T data with the Be target.	78
Figure 4.15	Mass histograms and fits for \bar{p} 's with rapidities from 1.6-1.8 and transverse momenta of 50-100 MeV/c, 100-150 MeV/c, and 150-200 MeV/c. These fits are for the 12 GeV/c, -0.2 T data with the Be target.	79
Figure 4.16	Mass histograms and fits for \bar{p} 's with rapidities from 1.8-2.0 and transverse momenta of 50-100 MeV/c through 150-200 MeV/c in 50 MeV/c increments. These fits are for the 12 GeV/c, -0.2 T data with the Be target.	80
Figure 4.17	Mass histograms and fits for \bar{p} 's with rapidities from 2.0-2.2 and transverse momenta of 100-150 MeV/c and 150-200 MeV/c in 50 MeV/c increments. These fits are for the 12 GeV/c, -0.2 T data with the Be target.	81

Figure 4.18	Mass histograms and fits for \bar{p} 's with rapidities from 2.2-2.4 and transverse momenta of 150-200 MeV/c. These fits are for the 12 GeV/c, -0.2 T data with the Be target.	82
Figure 4.19	Position of the mass peaks in the various histograms.	83
Figure 4.20	Widths used to create fits.	85
Figure 4.21	Plot of the invariant multiplicities $\frac{d^2\sigma}{\sigma_{inel}2\pi p_T dp_T dy}$ vs. p_T in MeV of \bar{p} 's from 19 GeV/c protons incident on a Be target. There are six panels. Each panel represents a different rapidity interval, starting with 1.4-1.6 and going to 2.4-2.6. The invariant multiplicities are plotted versus transverse momentum for each plot. Each invariant multiplicity is multiplied by a factor of 10^4	93
Figure 4.22	Plot of the invariant multiplicities $\frac{d^2\sigma}{\sigma_{inel}2\pi p_T dp_T dy}$ vs. p_T in MeV of \bar{p} 's from 19 GeV/c protons incident on a Cu target. There are six panels. Each panel represents a different rapidity interval, starting with 1.4-1.6 and going to 2.4-2.6 (moving first across and then down). The invariant multiplicities are plotted versus transverse momentum for each plot. Each invariant multiplicity is multiplied by a factor of 10^4	94
Figure 4.23	Plot of the invariant multiplicities $\frac{d^2\sigma}{\sigma_{inel}2\pi p_T dp_T dy}$ vs. p_T in MeV of \bar{p} 's from 19 GeV/c protons incident on a Pb target. There are six panels. Each panel represents a different rapidity interval, starting with 1.4-1.6 and going to 2.4-2.6 (moving first across and then down). The invariant multiplicities are plotted versus transverse momentum for each plot. Each invariant multiplicity is multiplied by a factor of 10^4	95

Figure 4.24	Plot of the invariant multiplicities $\frac{d^2\sigma}{\sigma_{inel}2\pi p_T dp_T dy}$ vs. p_T in MeV of \bar{p} 's from 19 GeV/c protons incident on a Be target. There are six panels. Each panel represents a different rapidity interval, starting with 1.4-1.6 and going to 2.4-2.6 (moving first across and then down). The invariant multiplicities are plotted versus transverse momentum for each plot. Each invariant multiplicity is multiplied by a factor of 10^5	96
Figure 5.1	Primordial distribution of \bar{p} 's in transverse momentum. The inverse slope parameters were taken from Allaby data.	98
Figure 5.2	Primordial distribution of \bar{p} 's in rapidity. Fit to E802's estimate of Allaby's dn/dy distributions. The points are the estimates of dn/dy from Allaby.	99
Figure 5.3	A parameterization for the annihilation cross section of \bar{p} 's in free space vs. that same quantity in nuclear matter. There are 2 E941 models employed. In the one with the greater annihilation cross section \bar{p} creation was allowed on collisions subsequent to the first collision of the incident nucleon. In the second, the \bar{p} could only be created in the first N-N collision.	102
Figure 5.4	Model \bar{p} 's from p-p collisions compared to the actual E941 p-Be data at 19 GeV/c. Invariant multiplicity, $\frac{d^2\sigma}{\sigma_{inel}2\pi p_T dp_T dy}$, is plotted vs. p_T in MeV. The invariant multiplicities are multiplied by a factor of 10^4 . The agreement is quite good. The overall normalization of the model was obtained from Eqn. 1.17.	103
Figure 5.5	Model \bar{p} 's from p-p collisions compared to the actual E941 p-Be data at 19 GeV/c. Invariant multiplicity, $\frac{d^2\sigma}{\sigma_{inel}2\pi p_T dp_T dy}$, is plotted vs. y . Plotting the invariant multiplicities this way suggests that the Gaussian fit to rapidity may not match. The higher rapidity \bar{p} 's appear to be suppressed.	104

Figure 6.1	Two parameterizations of the energy scaling of the \bar{p} creation cross section in p-p collisions. Notice that these are given with the total inelastic cross sections divided out.	106
Figure 6.2	Invariant multiplicities for Pb, Cu and Be targets as a function of rapidity at fixed p_T of 125 MeV/c. The beam momentum for all three targets was 19 GeV/c.	108
Figure 6.3	Ratio of \bar{p} invariant multiplicities Pb/Be. The data are presented as a function of rapidity. The beam momentum for all three targets was 19 GeV/c, and the transverse momentum for each data point is 125 MeV/c. The error bars include both statistical and systematic contributions. The data are consistent with an Pb/Be ratio that is at most one, and in all likelihood less than one.	109
Figure 6.4	Comparison of the production of other species of particles in p-A collisions to the production of \bar{p} 's. These data were taken from Reference (22) and from E941. In the plots there is no target dependence in the π spectra or K spectra, but \bar{p} 's show at least a small target dependence in both the Eichten data and E941.	111
Figure 6.5	On the top panel, the target dependence of the invariant multiplicities for \bar{p} 's produced in p-A collisions is shown. Below that, the invariant multiplicities for p + several targets is compared to Au+Au collisions in 4 centrality bins. The Au-Au data are divided by the estimated number of first collisions. The plots are for data at $y=1.9$ and $p_T = 125$ MeV/c	112

ABSTRACT

We present antiproton invariant multiplicities from Experiment 941 using 12 and 19 GeV/c proton beams incident upon targets of *Pb*, *Cu* and *Be*. Since we are currently unable to calculate antiproton yields in this regime from first principles, we must rely on empirical data in order to answer questions involving antibaryon production at these energies. Typically, the motivation for studying this topic using proton-nucleus (p-A) collisions is to shed light on antiproton production in the more complicated collisions between heavy nuclei (A-A). For this reason, this thesis will use the measured target dependence to illuminate issues relating to annihilation of antiprotons in the nuclear medium. It is found that, at 19 GeV/c beam momentum, the ratio of the antiproton invariant multiplicities in lead divided by those in beryllium is less than one and suggests strong antiproton annihilation in the lead target. Furthermore, the target dependence does not disappear as the antiproton's relative momentum with respect to the nucleus increases, which may suggest that the antiproton often rescatters without annihilating in the heavier target. A simple Glauber model is employed to quantify the absorption in the nucleus. In addition, comparisons will be made with the antiproton production in E941's predecessor experiment, E864. The energy scaling observed by E941 will assist in the comparison of our data to E864 and other experiments.

CHAPTER 1. OVERVIEW

“I was more frightened of my thesis defense than I was of brain surgery” – Dan Smith

The goals of this chapter are twofold. The first is to place the specific topic of antiprotons (\bar{p} 's) in the context of relativistic heavy ion collisions in general, and the second is to provide an overview of subject matter that will be addressed more completely in subsequent chapters. The first goal speaks to the relevance of this particular research, while the second is intended to give the reader a sense of the structure and scope of this thesis.

1.1 Introduction: \bar{p} 's in the Context of Relativistic Heavy Ion Collisions.

1.1.1 Relativistic heavy ion physics.

The study of relativistic heavy ion collisions is motivated by the desire to understand the nature of nuclear matter under extreme conditions. In order to achieve this understanding experimentally, atomic nuclei (each consisting of many “nucleons”, i.e., protons and neutrons) are smashed together. The analysis of these collisions amounts to a very complicated many-body problem. This field is dedicated to the study of the environment created by this process. It is, largely, the study of the bulk properties of nuclear matter.

Before the establishment of the quark model, nuclear matter would have been taken to mean the nucleons that comprise nuclei. The properties of nuclei are governed by the interactions between these constituent nucleons. At a more fundamental level, however, the nucleus can be considered to be the quarks and gluons of which the nucleons are constructed. Ultimately, nuclear matter consists of these more fundamental units (1).

Under conditions common on earth today (and, apparently, in almost all of the known universe) quarks and gluons bind together to form hadrons. There are two families of hadrons: baryons and mesons. Baryons are three quark objects, examples of which include protons and neutrons. Mesons, on the other hand, consist of quark-antiquark pairs. Family members include pions (π 's) and kaons (K 's). The reason that quarks tend to bind together to form these composite objects is related to the nature of the force that binds them. We call this force the "strong force" or the "color force". Rather than simply having two charges, (positive and negative) as in the electromagnetic case, the force that binds quarks can be described in terms of 6 states. We term these "color" states, and assign them values "red", "green" and "blue" and "anti-red", "anti-green", and "anti-blue". Every quark has a color, and one of the most fundamental rules regarding their interactions is that the net color charge must be zero. There must be either equal numbers of each color (giving rise to the 3 quark baryons), or equal amounts of color and anti-color (as in the case of the mesons). Any hadronic object found in nature must be "colorless". This rule was devised to codify the observation that free quarks are never observed. This constraint has been dubbed "confinement" because the quarks are confined to hadrons (2).

The mesons are unstable, but often have relatively long lifetimes (on the order of 10^{-8} seconds). For this reason, the average non-expert is more familiar with protons and neutrons. Protons are stable, and neutrons, which can be stable in many nuclei, have half-lives in free space of about 10.4 minutes.

Despite the fact that quarks are confined within hadrons, experimental data suggests that quarks interact very little within the confines of their hadrons. As the distance between quarks increases, however, they interact more intensely. The fact that this interaction tends towards zero as their separations become small is termed "asymptotic freedom". Mathematically, asymptotic freedom is described by the size of the "coupling constant" (a constant which is not at all constant) that links quarks to the "strong" field through which they interact. As quark separations increase, and the coupling constant grows, new quark-antiquark pairs are created. This phenomenon gives rise to various phenomena, such as the "jets" that are

routinely observed in high energy particle physics experiments.

The theory which describes the interactions between quarks and gluons is called quantum chromodynamics (QCD). One of the techniques for making numerical predictions using this theory, called "lattice QCD," has been used to justify predictions that under the proper conditions, confinement breaks down, and quarks are no longer bound in hadrons (3). A limit to the stability of hadrons had been discussed at least as early as 1965 (4). In 1974, T.D. Lee was already considering the possibility of eliminating confinement over a small region of space-time by exciting the physical vacuum (5) (6).

1.1.2 The quark-gluon plasma.

It is believed that if one or both of the temperature and particle density of nuclear matter are high enough, the protons and neutrons contained therein will transform into a plasma of quarks and gluons (7). The most probable means for creating the conditions necessary for the formation of this quark-gluon plasma (QGP) is through the collision of heavy ions (such as lead or gold nuclei) at high energies. Experiments have been carried out at various collision energies to determine the nature of the changes that may take place in the equation of state (EOS) of nuclear matter as a function of 'temperature' and density. (The term "temperature" is in quotes because the meaning of a concept defined for large numbers of particles is open to debate in the context of the comparatively sparsely populated heavy ion systems.) Early efforts focused on colliding the heavy ions at beam momenta that would stop the colliding material most effectively in the center of mass reference frame. The reason for attempting to use high particle density rather than high temperature in the initial attempts was because high temperature/low density conditions require higher beam energies than were available before the advent of RHIC (Relativistic Heavy Ion Collider). Experiments at RHIC attempt to create the QGP by exciting the physical vacuum in a region of space that is nearly baryon free. The experimental data in this thesis, however, were gathered at lower beam energies which were characteristic of attempts to create the QGP at high particle densities.

As far as the theory goes, there is a canonical phase diagram of nuclear matter often

shown at talks on the topic of the QGP. Originally, this diagram showed only two possible phases: a normal matter phase, in which quarks bind together to form hadrons, and the QGP phase, in which the quarks are deconfined within the plasma. Now, as theories have developed, the proposed set of plausible phase diagrams have become considerably more intricate. For example, it has been suggested that there may be a color superconducting phase at the high particle density, low temperature end of the spectrum (8). The possible existence of a critical point has also been proposed (9). A phase diagram showing both the original two predicted phases, and some of the new predictions is given in Fig. 1.1. Also included in this schematic are the relative paths in phase space probed by the AGS and RHIC accelerators.

The point made here isn't so much whether these particular new propositions turn out to be true, but that nuclear matter may turn out to have many phases. To paraphrase a comment made by Jack Sandweiss, the spokesman of the E864 Collaboration, if water, which consists simply of two species of atoms interacting through a relatively simple two charge force, has dozens of phases, then surely nuclear matter, interacting with a force denoted by three colors and several of the six species of quarks must be much more complicated. In any event, our field is devoted to the study of such questions.

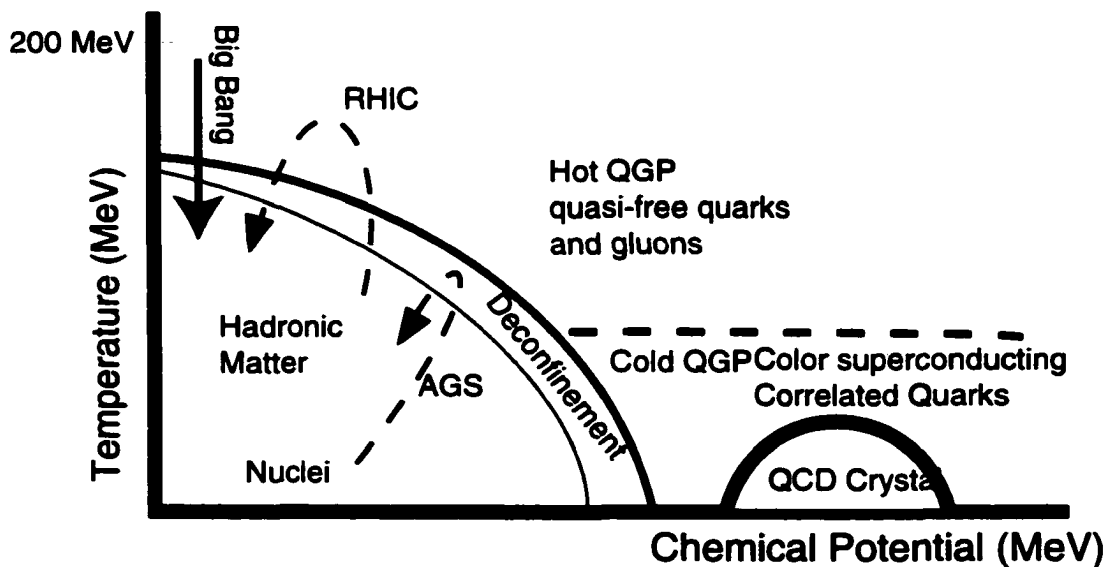


Figure 1.1 Contemporary phase diagram of nuclear matter.

Although the QGP is, perhaps, one of the more interesting changes that might occur in nuclear matter, there are many other phenomena that occur in relativistic heavy ion collisions that make the identification of the QGP phase difficult to ascertain. The thing which makes the identification the most difficult is the fact that by the time we are able to make any observations, any possible QGP has long since “hadronized”. As a result of such complexities, one must consider the ways that a potential signal for the QGP could be mimicked in a hadronic environment. Rather than considering these competing mechanisms as a hindrance to discovering the QGP phase, they should be considered as interesting phenomena in their own right. They represent the bulk properties of nuclear matter to no less extent than the proposed QGP. In any event, measurements of particle production in ultra-relativistic collisions are difficult to interpret because of the variety of mechanisms responsible for the particle yields we observe.

1.1.3 Quantifying collective effects

One problem with regard to the analysis of data from nuclear collisions is that, regardless of whether or not phase transitions occur, nucleus-nucleus collisions are not just superpositions of nucleon-nucleon collisions. (The short-hand term for a nucleon-nucleon collision is “N-N”. Nucleon-nucleus collisions are referred to as “N-A” collisions, and nucleus-nucleus collisions are termed “A-A” collisions. In practice, however, when the nucleons are protons, the letter “N” is replaced with a “p”. “p-A” collisions are nucleon-nucleus collisions in which the “p” informs us that the nucleon striking the nucleus is a proton. “A-A” is a term used to denote the collision of two nuclei, each with atomic number greater than one.)

One proof of the assertion that A-A collisions are not just superpositions of N-N collisions is that \bar{p} production occurs in A-A collisions in which the energy available for particle creation per nucleon in each of the nuclei is below the threshold level necessary for \bar{p} creation (10). Since the total energy of any two nucleon collision is, in that case, below the threshold energy for the creation of \bar{p} 's, it must be the case that some kind of multiple collision or many-body interaction is responsible for the creation of the \bar{p} 's. Therefore, the nucleus-nucleus case is

both qualitatively and quantitatively different than the nucleon-nucleon case. For example, a given nucleon may suffer an initial collision, causing it to go into an excited energy state, and then suffer subsequent collisions. This situation can not be described by the collision of two nucleons in their ground states. Another effect is the development of a dynamical pressure in the collision. This leads to so-called “flow” effects. These and other collective effects lead to particle yields that differ (in any given region of phase space) from the N-N case. For that matter, the number of N-N collisions that might characterize a given A-A collision is difficult to ascertain, and is, in any event, necessarily a model dependent quantity. The colliding systems are, after all, quantum systems. It may be that considering the collisions as superpositions of N-N collisions is too “classical” a picture to invoke, and the wave function of the nuclei is more complicated than such a simple picture suggests. One caveat to these conclusions must be made. One would expect some sub-threshold production of \bar{p} 's even without collective effects. This is because the Fermi distribution that describes the velocities of nucleons within the nucleus has a high momentum tail. The size of these tails, however, are a subject of debate. Occasionally, a nucleon with an extremely large Fermi momentum will possess enough energy to create \bar{p} 's. This effect of this mechanism has been calculated and it has been found that the subthreshold production far exceeds the level one might expect from the effects of Fermi motion alone. Reference (11) makes this point.

One way of attempting to better understand the A-A case is to study the intermediary p-A case. In a p-A collision, some of the collective effects characteristic of A-A collisions are present, yet the situation is simpler than in the A-A case. The central player in a p-A collision is the projectile proton and the products of the collision reflect the history of that proton's initial collision and subsequent development in the nuclear medium. In this case, the incident nucleon may often suffer several collisions and might often be in an excited state when it does so. These considerations suggest that as one studies the scaling from p-p collisions to A-A collisions, the p-A case is very useful. In particular, a complete analysis of all three regimes may help to sort out which deviations from expected scaling are due to normal hadronic mechanisms and which are due to a possible QGP.

1.1.4 Antiprotons in particular

The content of this thesis amounts to the measurement and analysis of \bar{p} production in p-A collisions at two collision energies and over a restricted range of resulting \bar{p} kinematics. In a fixed target experiment, the collision energy is constrained by the beam energy, and the detected \bar{p} kinematics are constrained by the geometry and performance of the detector.

While the dynamics of any physical system would presumably be of interest to the most curious minded physicist, a legitimate question is, “what use will these measurements be with regard to the stated purpose of the relativistic heavy ion community? Will the analysis of \bar{p} ’s produced in p-A collisions teach us anything about the bulk properties of matter under extreme conditions?”

One might expect that the yields of all particle species would be affected both by phase transitions and by other mechanisms as well. Noting how the yields change as a function of the number of nucleons involved in the collision, i.e., as a function of “centrality” is one possible way of identifying a regime in which something unusual occurs. Examining the yields as a function of their kinematic properties provides another perspective from which to analyze the collision process. Furthermore, the consistency of observed trends among various species of identified particles should provide important clues regarding the mechanisms at work in the collisions. For example, kaon yields reflect the number of strange quarks created in the collision, and \bar{p} yields reflect the production of antiquarks. Measurement of each of these species helps us to understand strange quark production and antibaryon production, respectively.

The \bar{p} measurements presented in this thesis will be compared to \bar{p} ’s produced in both p-p and A-A collisions. The scaling from p-A to A-A will be analyzed as a function of rapidity (y) which is related to the longitudinal momentum. Using data from other experiments, the scaling of other particle species as a function of similar kinematic variables will also be examined.

As mentioned above, accomplishing comparisons between p-p, p-A, and A-A collisions is complicated by the model dependence of the estimate of the number of nucleon-nucleon collisions in A-A collisions. Typically, this is accomplished by folding some kind of multiplicity measurement in with a simple geometric (“Glauber”) model. One very simple implementation

of this program is the “first collision model”. In it, it is assumed that any given nucleon only collides (at most) once. In A-A collisions, the number of first collisions is difficult to estimate experimentally, but in p-A collisions, the number is, by assumption, one. Of course, this assumption is clearly incorrect. A measure of just how incorrect can be inferred from the extent to which p-A collisions differ from p-p collisions.

When comparing the yields of \bar{p} 's from p-p to p-A to A-A regimes, there are two particular properties of \bar{p} 's that allow us to probe nuclear matter under extreme conditions. First off, they have a high annihilation cross section with ordinary matter. To be more precise, their annihilation cross section becomes very large as their momentum relative to other nucleons becomes small (screening mechanisms have been proposed that would inhibit this effect (13)). This makes them an excellent probe of the baryon density in a baryon rich environment (14). Secondly, if the available energy for particle creation is not significantly higher than the production threshold for \bar{p} 's, then their initial production is also very sensitive to the environment of their creation. Collective effects at these energies are very significant.

If A-A collisions can both enhance production over the nucleon-nucleon case and either increase or decrease annihilation (depending on the mechanism that is actually at work) then the total observed yield becomes a complicated interplay of all the various collective effects that influence the final outcome. Currently, the term “collective effects” refers to effects caused by the collective movement of nucleons in the nucleus, but the earlier papers written on the subject seem to include multiple collisions and the formation of resonances that subsequently interact as collective effects as well. In this thesis, the term “collective effects” refers to this broader class of phenomena. If these effects can be quantified in the p-A case, where there is not expected to be any QGP, then the A-A production can be estimated in the absence of a QGP. Then, the p-A to A-A comparisons mentioned above will become more meaningful. In fact, it has been suggested that enhanced antibaryon production may itself be a signal for the existence of a QGP. Kahana states that, “the dense plasma should contain a much higher concentration of antiquarks than represented by the sea quarks seen in proton-proton interactions (13).”

In line with the desire to disentangle the production mechanisms from the annihilation mechanisms, an attempt will be made (using the data in this thesis) to estimate an in-medium annihilation cross section for \bar{p} 's.

1.2 Measured Distributions

Since the bulk of this thesis is concerned with the measure of various distributions relating to \bar{p} 's, a discussion of some common distributions follows.

In order to derive expressions for the various differential cross sections commonly encountered in the literature on relativistic heavy ion physics, we start with the simple expression for the number of a given particle species produced as a function of the number of incident beam particles ($N_{produced}$), the number per unit area of scatterers (n_T) and the cross section for particle production (σ). The relation is given by Eqn. 1.1. Defined this way, the term “cross section” is the probability of producing the particle (or particles) of interest per incident unit of beam flux.

$$N_{produced} = N_{beam} n_T \sigma \quad (1.1)$$

Often, however, we are interested in the numbers of particles produced as a function of various kinematic parameters. The probability of creating a particle in a given region of phase space is termed a “differential cross section”. We thus create a differential from Eqn. 1.1. Eqn. 1.2 results.

$$dN_{produced}(\vec{p}) = N_{beam} n_T \frac{d^3\sigma}{dp^3} dp^3 \quad (1.2)$$

Eqn. 1.2 can be manipulated to produce a differential cross section. In addition, it is convenient to express the differential cross section in terms of the inelastic cross section, or equivalently, the number of inelastic events. This obviates the need to consider the elastic part of the total cross section, and simplifies matters experimentally, because, it is somewhat straightforward to design a detector to measure the number of inelastic events. The resultant differential cross section, eqn. 1.3, is referred to as the multiplicity.

$$multiplicity = \frac{1}{\sigma_{inel}} \frac{d^3\sigma}{dp^3} = \frac{1}{\sigma_{inel}} \frac{1}{N_{beam} n_T} \frac{d^3 N_{produced}}{dp^3} \quad (1.3)$$

Defining $n = \frac{1}{N_{inel}} N_{produced}$ leads to an expression for the multiplicity which is given by 1.4.

$$\frac{d^3 n}{dp^3} = \frac{1}{\sigma_{inel}} \frac{1}{N_{beam} n_T} \frac{d^3 N_{produced}}{dp^3} = \frac{1}{N_{inel}} \frac{d^3 N_{produced}}{dp^3} \quad (1.4)$$

Although we have derived an expression for the “multiplicity”, the distribution has some undesirable characteristics. For one thing, the phase space differential volume $dp_x dp_y dp_z$ is not relativistically invariant. Starting from the multiplicity, however, one can derive an expression for an “invariant” multiplicity.

First off, we note that whether we express $\frac{d^3 n}{dp^3}$ in spherical or in cartesian coordinates, the value will be the same at any given point in phase space. Therefore,

$$\frac{d^3 n}{dp^3} = \frac{d^3 n}{dp_x dp_y dp_z} = \frac{d^3 n}{P^2 dP \sin\theta d\theta d\phi} \quad (1.5)$$

Or, since $d\Omega = \sin\theta d\theta d\phi$

$$\frac{d^3 n}{dp^3} = \frac{d^3 n}{dp_x dp_y dp_z} = \frac{d^3 n}{P^2 dP d\Omega} \quad (1.6)$$

Several of the older papers that will be discussed, measured the multiplicity using the form of the multiplicity given by Eqn. 1.6, except that they multiplied the distribution by ‘E’. They did this because, it has the effect of forming a quantity with simple properties under Lorentz transformation. Before discussing the invariant multiplicity, however, let us note that the differential cross-section should be equivalently expressible in cylindrical momentum coordinates.

$$\frac{d^3 n}{dp^3} = \frac{d^3 n}{dp_x dp_y dp_z} = \frac{d^3 n}{p_T dp_T dp_\phi dp_z} \quad (1.7)$$

In Eqn. 1.7, p_T is commonly referred to as transverse momentum. In the case of azimuthal symmetry,

$$\frac{d^3n}{dp^3} = \frac{d^3n}{dp_x dp_y dp_z} = \frac{d^2n}{2\pi p_t dp_T dp_z} \quad (1.8)$$

Note that these cylindrical coordinates are desirable from the perspective of analysis of collisions because p_z is along the beam line and $p_T = \sqrt{p_x^2 + p_y^2}$ is perpendicular to it. These are symmetries that are naturally suited to the construction of most detectors, and are easy to visualize.

It is still necessary to construct a distribution that is relativistically invariant (or that only shifts by a constant). This is accomplished by multiplying the multiplicity by E . It can be shown that the phase space element $\frac{E}{dp_x dp_y dp_z}$ is an invariant. The argument for this assertion is based on the observation that:

$dp_x dp_y dp_z$ can be considered as the 0th component of an element of the hypersurface defined by the equation $p^i p_i = m^2 c^2$. The element of hypersurface is a four-vector directed along the normal to the hypersurface: in our case the direction of the normal obviously coincides with the direction of the 4 vector p_i . From this, it follows that $\frac{dp_x dp_y dp_z}{E}$ is an invariant quantity, since it is the ratio of corresponding components of two parallel four-vectors. (15)

It only remains to convert from p_z to rapidity. Rapidity is a commonly used kinematic variable that is related to the longitudinal velocity of a particle. It is popular because it has simple properties under Lorentz transformations. The transformation of a set of rapidities from one inertial reference frame to another is effected by the addition of a single constant for all rapidities. Rapidity is defined according to Eqn. 1.9 or, equivalently, Eqn. 1.10.

$$y = \ln \frac{E + p_z}{E - p_z} \quad (1.9)$$

$$y = \tanh^{-1}(\beta_z) \quad (1.10)$$

Using the above identity, one can show that $\frac{dy}{dp_z} = \frac{1}{E}$. Finally, we are left with

$$E \frac{d^3n}{dp^3} = \frac{d^2n}{2\pi p_t dp_T dy}$$

The invariant multiplicity, then, is given by Eqn. 1.11. Any time the term “invariant multiplicity” is used in this thesis, Eqn. 1.11 is implied.

$$\text{Invariant Multiplicity} = \frac{1}{2\pi p_T} \frac{d^2 n}{dy dp_T} \quad (1.11)$$

The distribution of invariant multiplicities as a function of p_T for many particle species are often fit with an exponential of the form $A \exp(-(m_T - m)/B)$, where A and B are the fit parameters. In particular, “B” is called the inverse slope parameter. It has a rich history, because it has been linked to the notion of a temperature. In fact, when physicists in this field are not being careful, they often refer to the parameter as the temperature. They do so, because, this exponential fit to the data is analagous to a Maxwell-Boltzmann distribution in which “B” really is interpreted to be the temperature. The problem here is that “temperature” is typically a concept defined in the context of a large number number of particles (such an $n_A = 6.02 \times 10^{23}$). One might debate the meaning of temperature in the context of heavy ion collisions, in which the particle number is relatively small. In recent years, many physicists have backed off of referring to this parameter as temperature, and leave it at “inverse slope parameter”. Still, one often gets the feeling that “behind shut doors” everyone still thinks of it as temperature. Furthermore, one suspects that this is the parameter that theorists use when incorpating temperature into their models. It should be noted that even particle distributions produced in $e^+ - e^-$ collisions can be fit with the above exponential. In that case the multiplicities are rather small, and the attribution of the notion of a temperature to the parameter becomes even more suspicious. At the Quark Matter 2001 conference, there were comments made to the effect that these Maxwell-Boltzmann distributions are a natural consequence of phase space arguments.

Given a large enough acceptance in p_T , it is possible both to find inverse slope parameters and integrate invariant multiplicities over all p_T . Doing so produces the $\frac{dn}{dy}$ distributions.

$$\frac{dn}{dy} = \int_0^\infty \left(\frac{1}{2\pi p_T} \frac{d^2 n}{dy dp_T} \right) 2\pi p_T dp_T \quad (1.12)$$

Table 1.1 Events sampled as a function of target. The 12 GeV/c Cu data were not analyzed for the purposes of this thesis, so that row was marked N/A.

Target	Events Sampled -0.2 T
19 GeV/c	
Pb 8.53%	114 M
Cu 9.61%	65 M
Be 3.68%	63 M
12 GeV/c	
Pb 8.53%	134 M
Cu 9.61%	N/A
Be 3.68%	176 M

1.3 Experimental Overview

While it may seem more reasonable to discuss previous experiments before coming to the subject of this analysis, it is useful to provide some of the experimental details regarding E941 first. The reason for this is so that the reader, when going over the background, can understand in which ways E941 can both extend and be compared to previous experiments and analyses. The E941 experiment was conducted at Brookhaven National Laboratory (BNL) in the fall of 1998. The \bar{p} 's were produced in a fixed target experiment using a proton beam provided by the Alternating Gradient Synchrotron (AGS) operating at beam momenta of 12 GeV/c and 19 GeV/c. Targets of lead, copper, aluminum and beryllium were used. The experiment was designated "E941" by BNL and its stated purpose was to measure leading particles in p-A collisions. The acceptance of the detector for \bar{p} 's ranged from about 1.4 to 2.6 in rapidity, and from 50 to 350 MeV/c in transverse momentum. The portion of the data set analyzed in this thesis is represented in Table 1.1.

The number of events sampled is greater than the number of events written to tape because we employed a second level trigger to determine which inelastic events were likely to have put tracks in our acceptance.

1.4 Previous Measurements and Other Experimental Results

This section will discuss some of the previous measurements of \bar{p} production in p-p, p-A, and A-A collisions and some of the theoretical implications of these data.

1.4.1 Prominent accelerators and colliders

Much of the research performed in the field of ultra-relativistic heavy ion physics has been done using one of three accelerators: the BEVALAC accelerator, the Alternating Gradient Synchrotron (AGS), and the European Organization for Nuclear Research (CERN) Super Proton Synchrotron (SPS). In the last year, the Relativistic Heavy Ion Collider (RHIC) has come online. The cutting edge research in relativistic heavy ion physics is now being pursued at this facility. It should also be emphasized that while the first three machines supplied the beam for the fixed target experiments, RHIC is a colliding beam machine (hence, the term "collider"). Colliding beam accelerators provide much more center of mass energy in collisions than their fixed target counterparts, because a lot of the energy in the fixed target experiments simply serves to increase the velocity of the center of mass of the system relative to the lab, rather than providing pure increases in available energy for particle production. In the case of a collider, the lab frame and the center of mass frame are often identical, whereas, for a fixed target experiment, the target is at rest in the lab frame, and the beam momentum is measured relative to that frame. The relationship between the energy available in the center of mass frame vs. that of the lab frame for a projectile nucleon incident upon a nucleon at rest in the lab is given by Eqn. 1.13. In the formula, factors of the speed of light (c) are suppressed for simplicity.

$$E_{cm} = \sqrt{2m(E_{lab} + m)} \quad (1.13)$$

E_{lab} is defined by Eqn. 1.14.

$$E_{lab} = \sqrt{p_{beam}^2 + m_N^2} \quad (1.14)$$

In order to get a feeling for the amount of energy that is necessary to conduct relativistic heavy ion research, consider the energy that must be available in the center of mass frame in order to create a $p\bar{p}$ pair from two colliding nucleons in the reaction:

$$N + N \rightarrow p + \bar{p} + N + N \quad (1.15)$$

In the center of mass reference frame, there must be enough energy to create the \bar{p} and three nucleons from the two original nucleons. The total available energy of the collision must be at least the rest mass of the final particles, or 3.75 GeV (equal to $4 \cdot m_N$, where m_N is the mass of a nucleon, neglecting the difference between protons and neutrons, i.e., 0.938 GeV). So, one might expect a typical relativistic heavy ion collider to operate with energies of at least that order of magnitude. Using equation 1.13, we find that 3.75 GeV in the center of mass frame requires a total beam energy of 6.57 GeV (which corresponds to a beam kinetic energy of 5.63 GeV) in the lab reference frame. Using equation 1.14, we find that we need a beam momentum of at least 6.50 GeV/c to be above threshold for the creation of \bar{p} 's in N-N collisions.

Table 1.2 lists typical operating energies and momenta for the BEVALAC, AGS, SPS, and RHIC. Clearly, moving to a collider was absolutely essential in order to get to a significantly higher amount of available energy in the center of mass.

Table 1.2 Typical operating energies for the BEVALAC, AGS, SPS, and the RHIC collider. Since these accelerators usually used heavy ion beams, the momenta and energies listed are per nucleon.

Accelerator	Lab beam momentum	Center of mass available energy
BEVALAC	2.9 GeV/c	2.7 GeV
AGS	10-20 GeV/c	4.5-6.3 GeV
SPS	200-450 GeV/c	19-29 GeV
RHIC	200 GeV/c total	200 GeV

Note that the BEVALAC's colliding energy per nucleon is below threshold for the creation of \bar{p} 's, and yet, experiments at that location still observed \bar{p} 's in A-A collisions. As mentioned above, these measurements proved that collective effects contribute to the creation of \bar{p} 's, since

their creation is impossible in any single nucleon-nucleon collision when the nuclei collide. So, we must take it as given that there is some enhancement in \bar{p} creation in heavy ion collisions close to threshold.

With this brief discussion of N-N to \bar{p} production thresholds and famous accelerators in heavy ion physics in hand, let's look at some of the previous measurements of \bar{p} production in p-A and A-A collisions.

1.4.2 BEVALAC data for sub-threshold \bar{p} production.

Koch and Dover were among those who provided analysis of \bar{p} production in A-A collisions from BEVALAC data (11). They stated that the BEVALAC data "suggest that a considerable degree of equilibration and collective interaction between the colliding nucleons takes place." They then pointed out that to test the hypothesis that collective effects are relevant, searches for sub-threshold production of particles were needed. These searches produced the result that \bar{p} 's were measured at levels 3 orders of magnitude higher than expected from the first collision model based on Fermi motion alone and not including annihilation. The authors noted that while several possible mechanisms could be responsible for the enhancement (such as decreasing mass gaps between positive and negative states with increasing nuclear density or the formation of a quark-gluon plasma) they were able to explain the enhancement by considering the effects of the combination of a multiple collision scenario and the production of resonances early in the collisions. Koch and Dover suggested that these resonances freeze up the mesonic degrees of freedom and force the production of \bar{p} 's. Their model was based on the following assumptions:

1. Thermal and chemical equilibrium (for nucleons and δ 's).
2. High baryon density. They suggested that creation should go as density squared while annihilation should only go as density.
3. Large part of available energy goes into delta resonances.

Following up on their notion that most of the mesonic degrees of freedom are frozen by the nucleonic resonances, in addition to the simplest \bar{p} mechanism:

$$NN \rightarrow NN + X\bar{X} \quad (1.16)$$

where X can be either a K or \bar{K} . Koch and Dover also consider reactions that include delta resonances in the initial state. The authors suggested that the rates for these processes grow quadratically with baryon density. Using their model, they were able to explain the BEVALAC data. They also pointed out that both formation times and absorption processes may strongly affect the \bar{p} yields.

1.4.3 BNL-AGS experiment E802 and CERN Allaby data.

Subthreshold production of \bar{p} 's at BEVALAC prompted researchers working at the BNL-AGS to further investigate \bar{p} production in relativistic heavy ion collisions. In 1993, experiment E802 at the BNL-AGS (experiments conducted at BNL receive designations beginning with the letter "E" and ending with a number) published an article on \bar{p} production. In it they reported the results of their p-A induced \bar{p} yields (12). These p-A data were follow up measurements to their A-A induced \bar{p} yields using the same detector. A theoretical analysis based on the combined E802 data set was performed by Kahana, Pang and Dover and was published concurrently in the same journal (13). Although the statistics of the E802 measurements were relatively low, this was an important set of measurements because the p-A and A-A data were taken using the same detector. Many systematic errors in the comparison of the p-A and A-A data were, of course, reduced because of this.

In their p-A data, the E802 sample consisted of only about 300 \bar{p} 's for all 4 targets: Be, Al, Cu, and Pb. Their data were taken with a proton beam momentum of 14.6 GeV/c and their kinematic acceptance for \bar{p} 's ran from $y = 1.0$ to 1.6 . Note that the nucleon-nucleon center of mass rapidity (y_{NN}) for this beam momentum is 1.71 , so all of their measurements were below beam rapidity. Their acceptance in transverse momentum (p_T) began at 300 MeV/c. The upper bound on their p_T measurements was set by the limited statistics of the experiment as opposed to the geometric acceptance of the detector. The large reach in p_T was useful to them

in calculating the inverse slope parameters of their invariant multiplicities. On the other hand, they were still limited by poor statistics. The E941 data analyzed in this thesis suffer from the opposite problem. While the statistics are much better, the reach in p_T is fairly limited. Because of E941's limited acceptance in p_T , calculation of an inverse slope parameter for our \bar{p} data would be imprecise. On the other hand, it will be possible for E941 to estimate $\frac{dn}{dy}$ by using our data to normalize an exponential fit, along with the inverse slope measured by some other experiment (at the same beam momentum). This exercise will be useful as a consistency check amongst various data sets.

E802 claimed that they could identify \bar{p} 's up to a momentum of 3.7 GeV/c. It will be seen that for most of the p-A experiments conducted before the E802 experiment began, \bar{p} particle identification (PID) was limited to momenta above about 4 GeV/c. Therefore, the total momenta of the particles measured by the older p-A experiments started where E802 left off. Although E941 was able to identify \bar{p} 's with slightly higher total momentum than E802, the cut off was similar to E802. Therefore, when comparing our E941 data to the older experiments, we are often forced to use our lowest quality data points, because our kinematic reach only overlaps slightly. With regard to comparing E941 to E802, there are similar sorts of problems. The low transverse momentum cut off for E802 overlaps the high transverse momentum cut off for E941, and the high rapidity cut off of E802 corresponds to the low rapidity cut off of E941. See Fig. 1.2 for clarification. To reiterate, E802 measured \bar{p} 's over the kinematic range $y = 1.0$ to 1.6 and $p_T = 300$ to 800 MeV/c.

E802 also measured the inverse slope parameters in their p-A data. Using their 14.6 GeV/c beam, E802 measured an inverse slope for \bar{p} 's of 93 ± 18 MeV/c averaged over all three targets. Their inverse slope for K^- was 129 ± 5 MeV/c, and for π^- was 147 ± 1 MeV/c. They also calculated $\frac{dn}{dy}$ for their yields. The results are reproduced in Table 1.3. Note that if E941 were capable of measuring our inverse slopes, our higher beam momentum data should yield larger inverse slope parameters.

Kahana *et al.* analyzed the E802 p-A results as well as E802's previous A-A results and managed to form a self-consistent model only when they included a screening mechanism to

Table 1.3 E802 results: Multiplicity densities and particle ratios. Columns 2, 3, and 4 give $\frac{dn}{dy}$ for π^- , K^- , and \bar{p} production in the fiducial rapidity interval obtained from the average p_T procedure (see text). The last two columns quote the $\frac{dn}{dy}$ ratios between \bar{p} and π^- and \bar{p} and K^- in the fiducial rapidity interval.

Collision system		$\frac{dn}{dy}(1.0 \leq y \leq 1.6)$			$10^3 \bar{p}/\pi^-$	\bar{p}/K^-
		$10^1 \pi^-$	$10^2 K^-$	$10^1 \bar{p}$		percent
p+Be	Min. bias	3.89 ± 0.03	0.92 ± 0.05	3.8 ± 0.8	1.0 ± 0.2	4.2 ± 0.8
p+Al	Min. bias	4.40 ± 0.03	1.17 ± 0.05	4.7 ± 1.0	1.1 ± 0.2	4.0 ± 0.9
p+Cu	Min. bias	5.22 ± 0.05	1.25 ± 0.08	4.9 ± 1.4	1.0 ± 0.3	3.9 ± 1.1
p+Au	Min. bias	5.36 ± 0.04	1.34 ± 0.06	4.9 ± 1.1	0.9 ± 0.2	3.7 ± 0.8

inhibit \bar{p} annihilation in the A-A collisions (13). The idea is that the baryons and antibaryons are screened from each other by the presence of intervening mesons. They claimed that the only other option would be to ascribe an unacceptably large formation time to the \bar{p} . It should be noted that in their analysis, they utilized a hadronic cascade model, ARC, to fit the E802 data. The version of ARC employed utilized resonances. This is consistent with the Dover's earlier suggestion to consider such resonances.

When modeling the E802 data using ARC, the authors claimed that the only inputs were the fundamental hadron-hadron cross sections for both the production and annihilation of antinucleons. The annihilation cross section in free space for \bar{p} 's was quite well known (16). For the production cross section, however, the lowest energy p-p data for the production of \bar{p} 's available were those of J.V. Allaby from a CERN experiment (17). These data were taken with a proton beam momentum of 19.2 GeV/c, still considerably higher than the E802 beam momentum. Although the Allaby data were never formally published in a refereed journal, E802 and Kahana *et al.* relied on the Allaby data to estimate the \bar{p} production cross section at the beam momentum used by E802. Costales (18) developed a parameterization of the production cross section from the data of Allaby and Amaldi so that they could scale the production cross section from 19.2 GeV/c to E802's 14.6 GeV/c (17) (19). The parameterization is shown in Eqn. 1.17.

$$\frac{\sigma_{pp \rightarrow \bar{p}X}}{\sigma_{inel}} = (0.3696\epsilon + 0.2301\epsilon^2) \times 10^{-3} \quad (1.17)$$

In trying to explain the E802 p+Be using this parameterization with the ARC cascade model, Kahana *et al.* obtained abundances that were 30 percent higher than the E802 p+Be data. Using the E802 p+Be data to adjust the parameterization, they obtained eqn. 1.18.

$$\frac{\sigma_{pp \rightarrow \bar{p}X}}{\sigma_{inel}} = (0.3645\epsilon^2 + 1.478\epsilon^3) \times 10^{-4} \quad (1.18)$$

Since the E941 data were taken at 12 and 19 GeV/c, it will be possible to test these parameterizations over a small \bar{p} kinematic range for p+Be (but, unfortunately, not for p+p) collisions. This test is important because it will reflect on the accuracy of the E802 analysis, as well as other important heavy ion analyses. One such example is the E864 estimate of the $\frac{\bar{N}}{p}$ ratio. E864 used Eqn. 1.18 to scale their data to the energy range of E878. We will return to these parameterizations later in this thesis. For example, they will be used in the modeling presented in chapter 5.

Table 1.4 Allaby data, dn/dy , for 19.2 GeV/c protons incident upon targets of Be and Pb. These numbers were obtained by reading off the plot in Fig. 3 in reference (12).

Rapidity	pp	pBe	pPb	Pb/Be
1.45	3.2×10^{-5}			
2.23	1.6×10^{-3}	1.6×10^{-3}		
2.52	7.0×10^{-4}	7.1×10^{-4}	5.0×10^{-4}	0.7
2.78	1.9×10^{-4}	1.8×10^{-4}	1.0×10^{-4}	0.55
2.98	3.2×10^{-5}	3.0×10^{-5}	1.5×10^{-5}	0.5
3.13	2.8×10^{-6}	2.0×10^{-6}	9.0×10^{-7}	0.45

E802 reported no target dependence in their data. The Allaby data, however, displayed a Pb/Be ratio of about 0.7 in dn/dy (12) at $y=2.52$. This can be seen in Table 1.4. Furthermore, The target dependence in the Allaby data shows a rapidity dependence as well. At y_{nn} rapidity for the Allaby experiment, there is little target dependence, but as one goes to higher rapidities, the target dependence becomes more pronounced.

To summarize, E802 observed no target dependence in their p-A data to the precision of their measurement. On the other hand, their small statistical sample led to large error bars, so, unless the target dependence is large, they would have missed it. Allaby did observe some target dependence. In order to explain the \bar{p} production in the A-A data, Kahana invoked a screening mechanism for the \bar{p} 's in nuclear matter. Later in this thesis, an effective in-medium annihilation cross section will be derived. If this cross section is smaller than the free space annihilation cross section, than any of the suggestions for decreased annihilation or increased initial production gain credibility. Finally, E802 reported that while they measured an inverse slope parameter of 93 ± 18 MeV, slightly lower energy experiments reported inverse slopes in the range of 65 to 82 MeV. Slightly higher energy experiments, such as that of Allaby, recorded observations of inverse slopes of about 110-130 MeV/c in p-p and 130-170 MeV/c in p-A. E941 will have the opportunity to compare energy scaling, and target dependence to these experiments and will be able to compare some other results as a consistency check.

1.4.4 Other older experiments and analysis.

Kahana *et al.* are not the only ones who have suggested mechanisms that inhibit the annihilation of \bar{p} 's in nuclear collisions. Spieles *et al.* argued that the real part of an antinucleon-nucleus optical potential depresses the annihilation cross section relative to the free space annihilation cross section of \bar{p} 's (20).

CERN experiment NA44 also measured \bar{p} production in p-A and A-A collisions, albeit at collision energies well above those of the AGS. Using beam momenta of 200 and 450 GeV/c, they found that while the cascade model RQMD did a reasonable job of fitting the p-A \bar{p} yields, it underestimated the A-A yields, perhaps another indication that \bar{p} annihilation is suppressed in the A-A case.

There were other early measurements of \bar{p} production in p-A experiments that observed the same sort of target dependence seen by Allaby. Eichten *et al.* also observed target dependence at a level comparable to that of Allaby, although Eichten *et al.* utilized a 24 GeV/c proton beam instead of the 19.2 GeV/c proton beam used by Allaby. See reference (22) for details of

the Eichten experiment.

In some regards, the evidence from these experiments (Allaby, E802, NA44, and Eichten) paints a somewhat self-consistent picture. It seems to be the case that \bar{p} yields are typically enhanced in A-A collisions. While \bar{p} production seems to decrease with increasing target size in the p-A regime, the dependence is not as strong as one might think given the size of the free space annihilation cross section of \bar{p} 's. This becomes even more evident when one examines the A-A regime.

1.4.5 E910

The final experiment to be mentioned at the BNL-AGS is E910. They ran at two beam momenta, 12.3 and 17.5 GeV/c and measured \bar{p} 's produced in the collision of protons with Au, Cu, and Be. In the reference given, they attempted to calculate an effective in-medium annihilation cross section for \bar{p} 's as well. They did this using a centrality measurement based on the number of slow protons (or "grey tracks") produced in their collisions. While this is certainly a novel and impressive technique, it should be noted that they had a small sample size of \bar{p} 's with which to work, and they used a rapidity bin that ranged from $y=1.0$ to 2.0 . Therefore, their effective annihilation cross section is a sort of mean effective annihilation cross section. It turned out to be more than a factor of 5 lower than that of the free space annihilation cross section. Although Brian Cole has stated that the only way to obtain such a measurement is using the centrality measurement available to E910, we will attempt to measure a similar quantity using the E941 minimum bias data.

The phase space coverage of E941, Eichten, E802 and E910 is given in Fig. 1.2

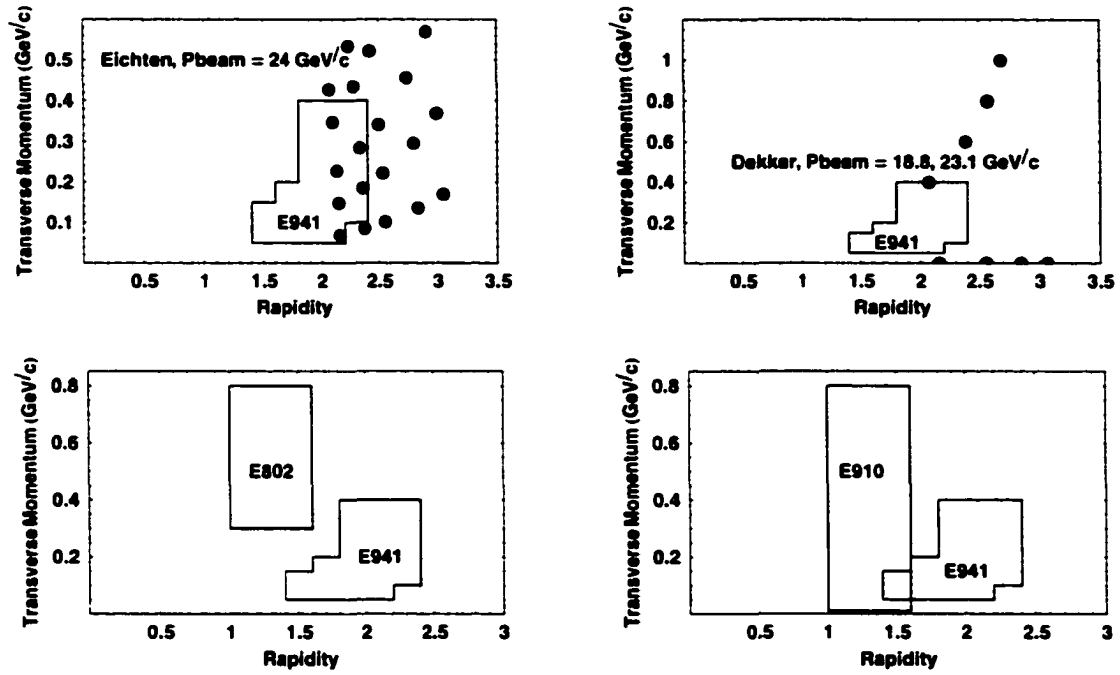


Figure 1.2 Phase space coverage of E941 and some other experiments. The boxed region represents E941's coverage. Note that just because data points overlap those of E941's coverage, they are not necessarily comparable because they were not, in general obtained, using the same beam momenta.

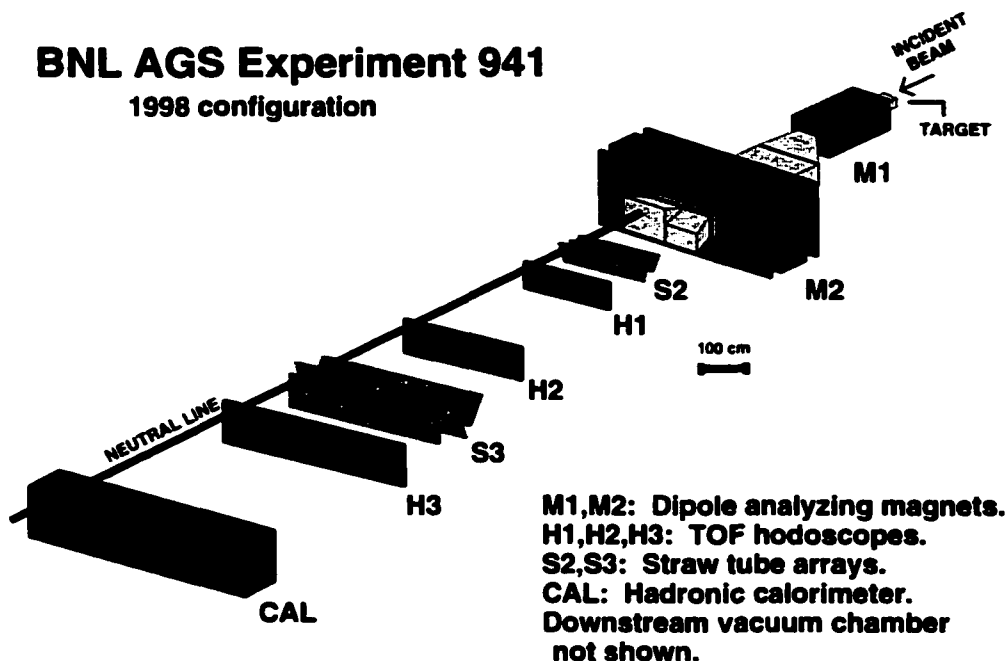
CHAPTER 2. THE EXPERIMENT

E941 was a fixed target experiment in which protons were collided with targets of Pb, Cu, Al, and Be. The beam momenta used were 19 and 12 GeV/c. This chapter will describe the experimental layout and apparatus. It should be noted that when the term “detector” is used in this thesis, it either refers to a particular subsystem of the experimental apparatus, such as the hodoscope system, or it refers to the experimental apparatus as a whole. The intended meaning should be clear from the context of the usage.

2.1 The Alternating Gradient Synchrotron

A proton beam was provided by the Alternating Gradient Synchrotron at Brookhaven National Laboratory in September and October of 1998. The E941/E864 detector was located on the A3 beam line of the accelerator. Records of the output of our experiment’s beam counter indicate that an average of 800,000 beam protons were provided per beam “spill”, where a given spill lasted 4 seconds with a 2 second duty cycle.

Given the 800,000 protons per spill, an 8 percent target would yield 64,000 inelastic interactions. Rejection factors from our LET trigger tended to vary between about 5 and 15. Assuming a factor of 10, 6,400 inelastic events placing tracks in our acceptance would occur per spill, so the data acquisition system (DAQ) would need to be capable of recording as many of these as possible. The E941 DAQ tended to record about 2000 such inelastic interactions per spill. In cases where the number of minimum bias interactions exceeded the rate of our data acquisition system, we simply applied a prescale factor, say “n”, to our 1st level trigger, so that only 1 out of every n events was considered for a second level trigger.



J.K.Pope November 21, 1997

Figure 2.1 Perspective view of the E9-41 spectrometer. The vacuum tank and the upstream beam counters are not shown.

2.2 Layout

The E9-41 detector was inherited from the E86-4 collaboration. The personnel for the two experiments were also nearly identical. The E86-4 collaboration had been formed to search for “strangelets”, a novel state of matter characterized by nearly equal numbers of up, down and strange quarks (23) (24). Rather than being bound up into hadrons, these quarks were imagined to clump up into a single color singlet state. One expected property of such an entity would be a low charge to mass ratio. These particles would therefore be expected to have relatively stiff trajectories. Therefore, the detector was envisioned to measure tracks of particles with forward kinematic properties. The E86-4 detector was optimized to search for metastable or stable forms of these particles, so it was designed to be able to identify particles with proper lifetimes τ greater than or equal to about 40 ns. Since sensitivity was the most important single criterion for the experimental apparatus, the detector needed to perform with a high data rate. The design sensitivity of the detector for rare composite objects was 1 in

10^{11} collisions. This was accomplished by having a high-speed data acquisition system, and an arrangement for rejecting events that lacked the desired characteristics. The later requirement was fulfilled by the creation of a Late Energy Trigger (LET), which will be discussed later in the chapter. A schematic diagram of the overall detector is presented in Fig. 2.1.

The elevation view in Fig. 2.2 shows that the beamline and target were above the detectors. The detector tracked those collision products that travelled downward into the detector area. Uninteracted beam travelled in vacuum to a beam dump, as shown in the elevation view. The plan view in the figure shows that the detectors were angled slightly with respect to the beam axis. In every case but that of the calorimeter, this was done to maximize the probability that incident particles would intersect the detectors at right angles. The calorimeter at the end of the experiment, however, was angled so that the average particle would enter at a 3 deg angle. This was done to prevent showers from developing along the axis of the scintillating fibers.

The main purpose of the p-A run (whose \bar{p} yields are studied in this thesis) was to study leading particles (i.e., the particles that carry away the most momentum from collisions). They are believed to be associated most closely with the incident proton because their momenta most nearly matches the projectile momenta. The study of \bar{p} 's was a secondary goal in the experiment. Accordingly, the magnetic field settings used on the dipole analyzing magnets and the triggering mechanisms were chosen to optimize the study of leading particles rather than \bar{p} 's.

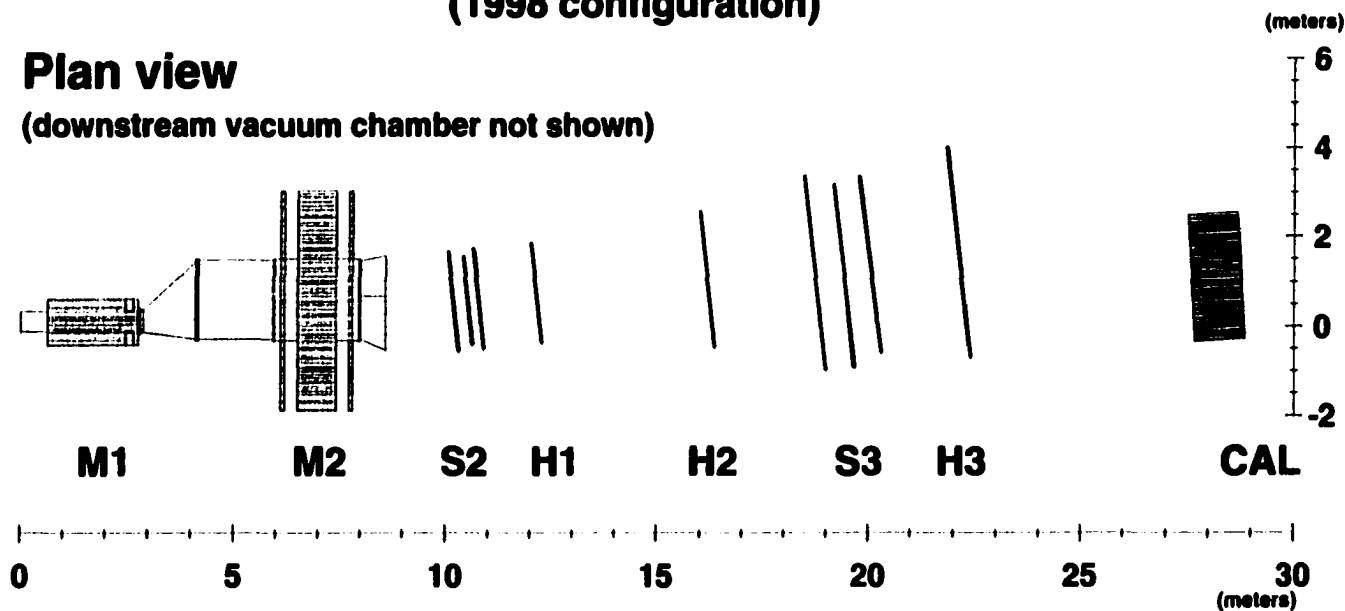
2.2.1 Coordinate system

For the purposes of this thesis, a right-handed coordinate system will be adopted such that the z axis is aligned with beam axis, and such that increasing z corresponds to the downstream beam direction. The horizontal plane (that of the floor of the experiment, for example) is defined by the x-z axes, and a vertical plane is denoted by the y-z axes. The direction of increasing x and y are chosen to be consistent with a right hand coordinate system.

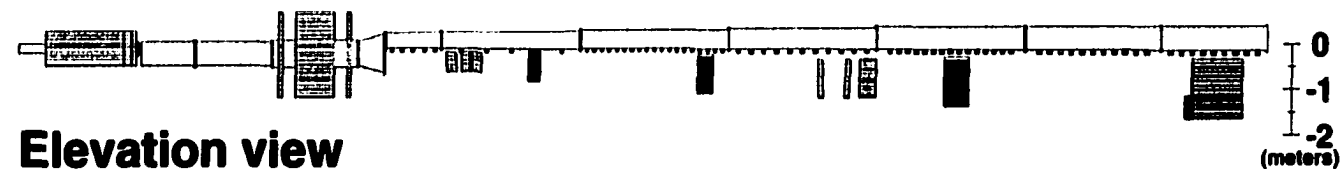
BNL AGS Experiment 941 (1998 configuration)

Plan view

(downstream vacuum chamber not shown)



Elevation view



M1,M2: Dipole analyzing magnets.
H1,H2,H3: TOF hodoscopes.

S2,S3: Straw tube arrays.
CAL: Hadronic calorimeter.

J.K.Pope May 7, 1996

Figure 2.2 Plan and elevation views of the E941 spectrometer. The vacuum tank and the upstream beam counters are not shown.

2.3 Detectors

2.3.1 Magnets, collimator and plug

The spectrometer used two dipole analyzing magnets. The first magnet (M1) was an 18 inch wide, 72 inch long dipole magnet (referred to as an AGS 18D72). The gap in the magnet was 10 inches. The second magnet (M2) was a large aperture dipole magnet obtained from SLAC (a 72D36, i.e., 72 inches wide, and 36 inches long). The two were separated by 4 meters. The motivation for using two separated magnets was to introduce a detector (in vacuum) between the two to eliminate backgrounds created away from the target. An additional straw tube station was constructed for this location, but, unfortunately, this particular straw tube station did not perform well and did not turn out to be useful for data analysis.

In order to minimize scattering off the pole tips of the magnets and other material in that vicinity, two components were installed: a brass collimator inside M1, and a plug located just before M2, as can be seen in Figs. 2.3 and 2.4. The acceptance of particles into the downstream portion of the experiment was limited by this collimator, the plug, and by the aperture of M2. As the figure shows, the collimator limited the acceptance both top and bottom and on each side.

The convention distinguishing positive field settings from negative ones was chosen such that positive fields tended to steer positively charged particles into the acceptance of the detector while negative field settings did the same for negatively charged particles. In the past, the field settings have varied between -1.5 and +1.5 Tesla. Table 2.1 matches various particle species with optimal field settings.

Notice also that the “neutral line” plotted in Fig. 2.4 does not cut through the middle of the angular acceptance. The detector was not symmetric for positive and negative particles. The sign of the field optimized the acceptance for one or the other. The vertical acceptance ranged from -17.5 mrad to -51.3 mrad. The horizontal acceptance ran from -32.0 mrad from the beamline to 171.0 mrad, where the positive angle denotes direction in which the particles of interest would bend.

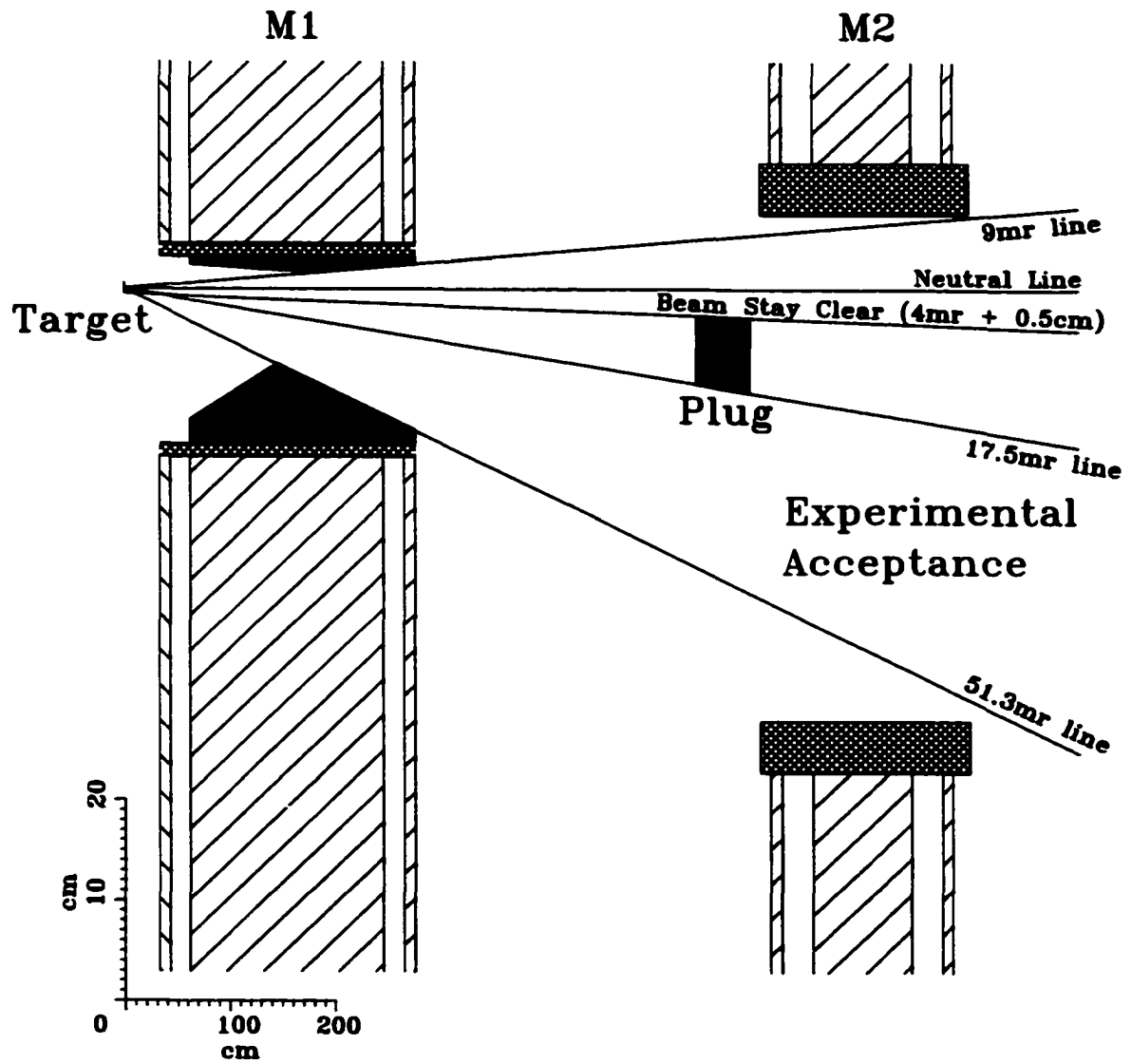


Figure 2.3 A close up elevation view of the region of the magnets, collimator and plug.

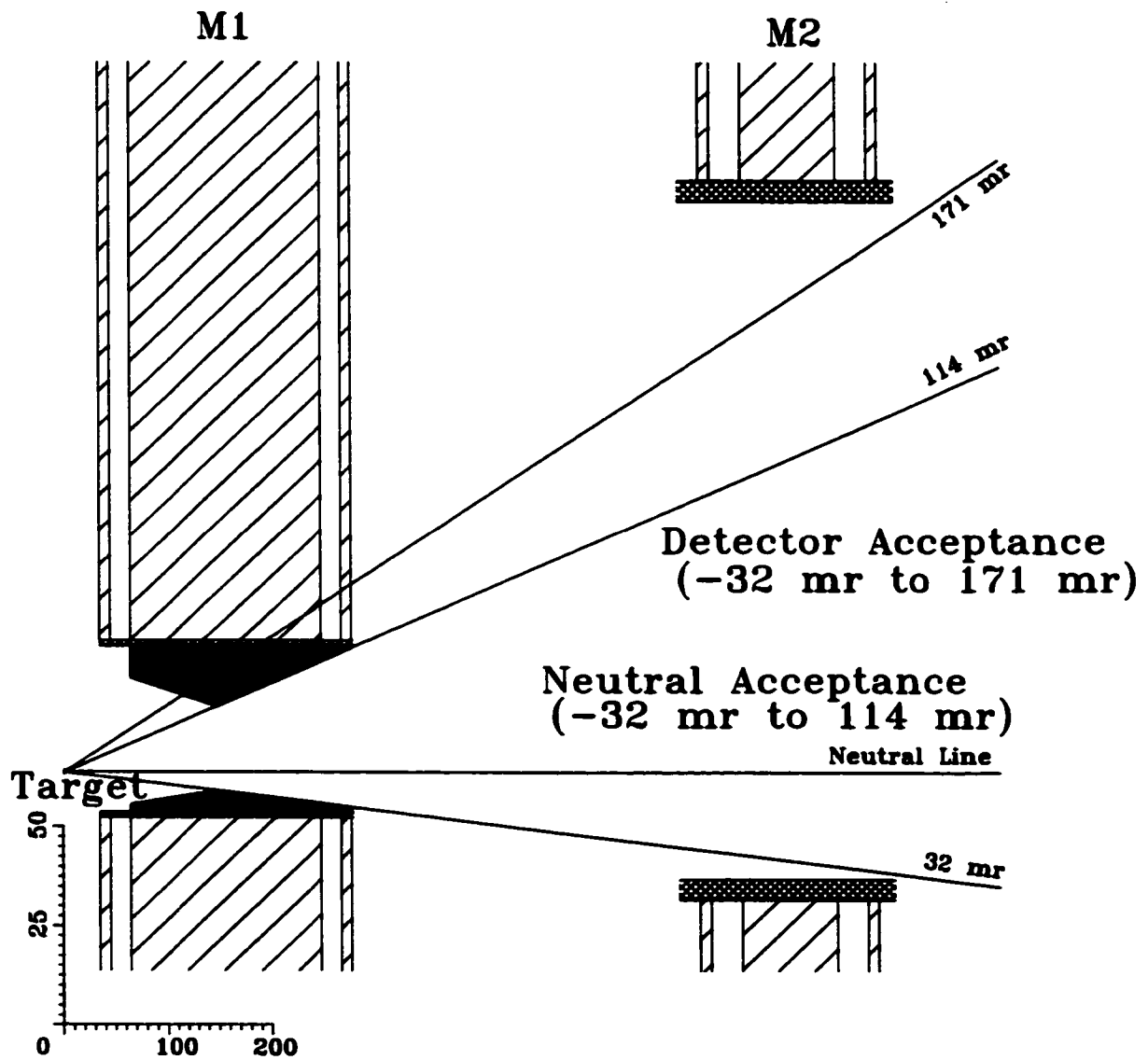


Figure 2.4 A close up plan view of the region of the magnets, collimator and plug.

Table 2.1 Particle species whose acceptance is optimized by the above field settings.

Field Setting	Particles
-0.75	Antideuterons and Negative Strangelets
-0.45	Antiprotons and Chiral Solitons
-0.20	Negative Kaons and Protons
+0.20	Positive Kaons and Protons
+0.45	Protons and Deuterons
+0.75	Light Nuclei
+1.50	Positive Strangelets and Rare Isotopes

For the 1998 p-A run, ± 0.2 T field settings were chosen to enable the measurement of pions which would be swept out of the experimental acceptance by the higher field settings.

2.3.2 Beam counters

There were several beam counters used in the experiment. Two of these were located upstream of the target, and two were located downstream of it. Of the two counters upstream of the target, the most important (from the perspective of the analysis) was a scintillator device named MITCH (MIT Cerenkov counter) which was used to count incident beam particles. For the E864 A-A experiment, MITCH was equipped with quartz plating, but for the E941 p-A experiment, the quartz was replaced with scintillator. This detector consisted of 2 pieces of scintillator, one upper and one lower. The detector was used to help aim the beam, since when well aimed, the number of counts from the upper scintillator should, roughly, equal those from the lower scintillator. In addition to counting incident beam particles, the electronics start gate and the "time zero" reference for time of flight measurements were set by the MITCH detector.

The other important beam counter upstream of the target was a gas Cerenkov detector, intended to veto events caused by incident K's rather than protons that had contaminated the beam.

As for the two counters placed downstream of the target, the first, just 13 centimeters downstream of the target, was an interaction detector (MULT). The reason for this name was

that, in the heavy ion collision regime, it's response was related to the multiplicity of the produced particles in any given collision. In the p-A regime, however, it was used purely to determine when inelastic interactions occurred, and provided no compelling centrality information. It consisted of a scintillating annulus segmented into four quadrants. Uninteracted beam traveled through the hole in the scintillating annulus, while interaction products activated the surrounding material. The angular coverage of this detector spanned 5 to 45 deg. Each quadrant had a photomultiplier tube and accompanying electronics attached to it.

Finally, at the tail end of the experiment, there was an end counter for uninteracted beam called MAC. With the target out, this detector could be used to determine the beam momentum precisely (by examining how much the uninteracted beam bent in the B field of the analyzing magnets). For p-A running, this detector also enabled us to estimate the number of times the interaction trigger was falsely activated. The source of this problem was particles that were created in the target but were not caused by interactions between the projectile and target nucleons. Rather, they were high energy electrons that resulted from the collision of projectile protons with atomic electrons in the target. This background, called "delta rays", will be discussed more thoroughly in chapter 4. MAC was useful in determining the false triggers, because it recorded the arrival of uninteracted beam at the tail end of the experiment. If a projectile proton was detected in MAC, it usually had not undergone an inelastic interaction in a nucleus.

2.3.3 Straw tubes

The straw tube stations provided precision tracking in the experiment. Roughly speaking, each straw tube was a proportional counter with a center anode wire in a mylar tube, with the tube forming the grounded cathode. Arrays of these tubes formed planes. In all, there were six straw tube planes, divided into two stations (S2) and (S3). Within a group, the planes were labeled "U", "V", and "X". The "X" plane straws were oriented vertically, while the "V" and "U" planes were angled ± 20 deg from the vertical respectively. These orientation of these angles is given from the perspective of one viewing the stations from upstream. Choosing the

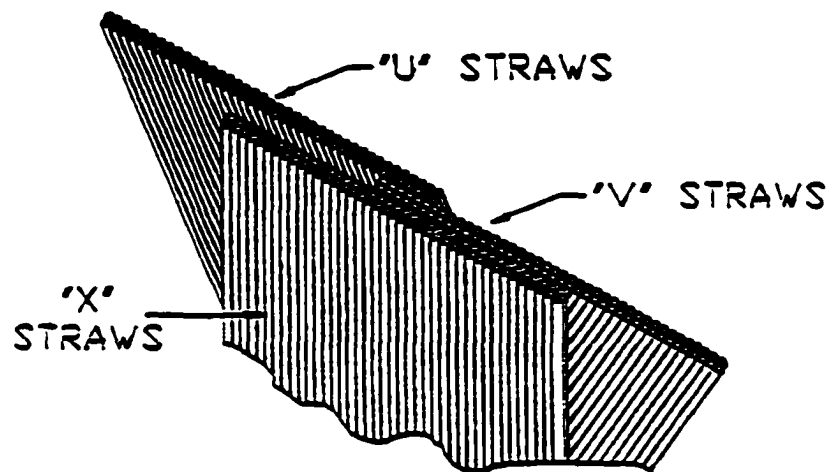
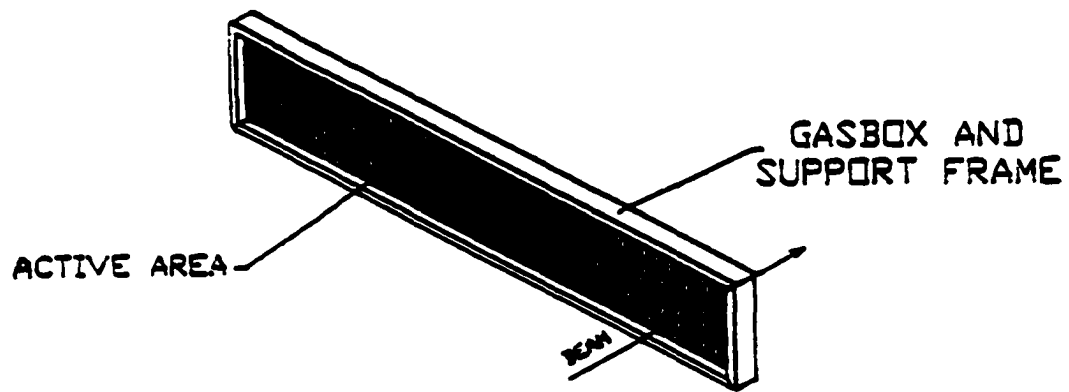


Figure 2.5 Drawing of a straw tube station. Each station consisted of three planes

planes to be angled in this way allowed three dimensional localization of the space-time points. Some of the specifications for each of the planes is given in Table 2.2. A drawing of a straw tube station is given in Fig. 2.5.

Table 2.2 Specifications for the straw chambers.

	Number of Straws	Straw Radius (cm)	Straw Length (cm)	Angle to Vertical deg
S2X	960	0.2	48.55	0.0
S2U	960	0.2	48.55	+20.0
S2V	960	0.2	48.55	-20.0
S3X	1920	0.2	90.20	0.0
S3U	1920	0.2	90.20	+20.0
S3V	1920	0.2	90.20	-20.0

The straw outputs were hit-or-miss electrical signals. They were amplified and read out with a LeCroy PCOS IV CAMAC system.

2.3.4 Hodoscopes

The scintillator time-of-flight hodoscopes were the heart of the spectrometer tracking. The system produced timing, charge, and position information on tracked particles. There were three hodoscope planes. Each plane was segmented into 206 slats. The slats were constructed from Bicron BC-404 scintillator. Each slat was wrapped in aluminized Mylar to keep external light out. Small flashes of light produced by the passage of charged particles through the scintillator were then detected by photomultiplier tubes (PMT's) mounted at the top and bottom of each slat.

Light guides were attached at the top and bottom of each scintillator slat to reflect the light through a 90 deg bend. A single slat is shown in Fig. 2.6. The wrapping of the scintillator was loose enough to allow an air interface between the scintillator and the Mylar. This assisted in producing the desired total internal reflection of light in the scintillator and lucite. The scintillator dimensions are given in Table 2.3. The light guides connected the scintillator to the PMT's. Phillips XP2972 PMT's were chosen. Cockroft-Walton base electronic systems were used to power the PMT's. The high voltages that fed the PMT's were generated from

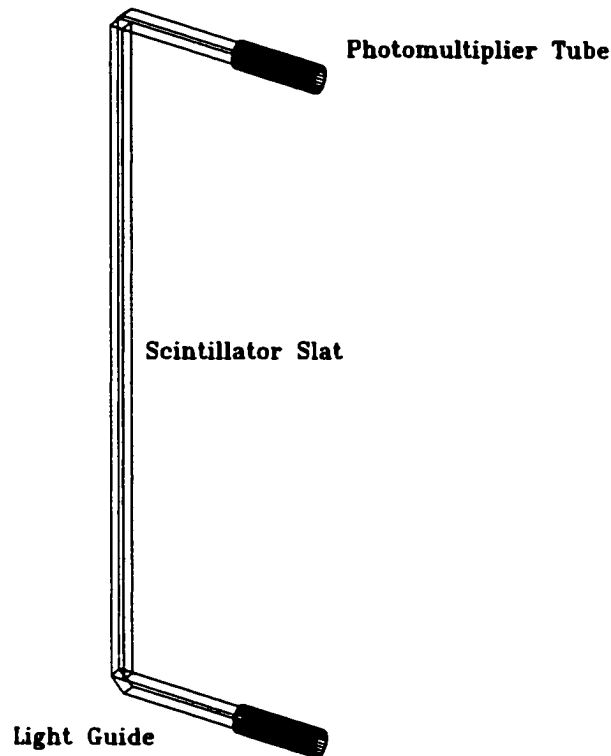


Figure 2.6 One slat of the hodoscopes.

low voltages transformed at the base. The bases also split the output signals internally, and included on-board discrimination of one of the two signals to produce timing information. Doing the discrimination on-board improved the performance of the system because the signals would have degraded when travelling through the cables to the data acquisition system. The high voltages and discriminator thresholds were controlled by a single personal computer that sent commands to the detectors using an RS232 cable.

The 90 deg bends between the slats and the light guides were alternated forwards and backwards for each adjacent slat. In addition, the slats were staggered vertically. This compactness allowed the system to be placed close to the vacuum chambers so that tracks with transverse momenta close to 0 p_T could be tracked. A portion of the H1 detector is shown in Fig. 2.7.

In addition to individually wrapping each scintillator slat (thereby isolating it from the adjacent slats) each hodoscope plane was wrapped and light tighted as a single unit. The planes were rotated at about 6 deg with respect to the xy plane to orient the detector perpendicular

to the average charged particle trajectory.

Table 2.3 Hodoscope slat dimensions.

Plane	Number of Slats	Width (cm)	Height (cm)	Thickness (cm)
H1	206	1.105	63.6	1.0
H2	206	1.506	81.3	1.0
H3	206	2.306	106.4	1.0

The x position of tracks was determined by the slat number, and the y position was determined from the difference between the top and bottom PMT signals. The time-of-flight measurement was made using the sum of the two time measurements. The difference of the PMT times was determined by the vertical position of the track, while the sum of the PMT times was independent of it. Together, the three hodoscope planes provided 3 space-time points for tracked particles.

The hodoscopes also provided three independent charge measurements via the pulse height information from energy loss (dE/dx) in the scintillator. The charge z of tracks were determined independently in each hodoscope plane using the the geometric mean of the top and bottom ADC measurements. The geometric mean was used because it did not depend on the vertical position of the hit in the slat. Specifically,

$$z^2 = \sqrt{G_{top}(ADC_{top} - PED_{top})G_{bot}(ADC_{bot} - PED_{bot})} \quad (2.1)$$

where G_i , ADC_i , and PED_i are the gain, ADC value and pedestal for the top and bottom signals, respectively. The pedestals were determined from “empty” events (taken at randomly selected times when no particles had triggered our detector). The gains were normalized for every slat by using tracked particles.

The slats were labelled such that increasing slat numbers correspond to increasing x positions using the coordinate system previously defined.

2.3.5 Calorimeter

The calorimeter was located at the downstream end of the experiment. This device utilized a “spaghetti” design, which used scintillating optical fibers embedded longitudinally in Pb.

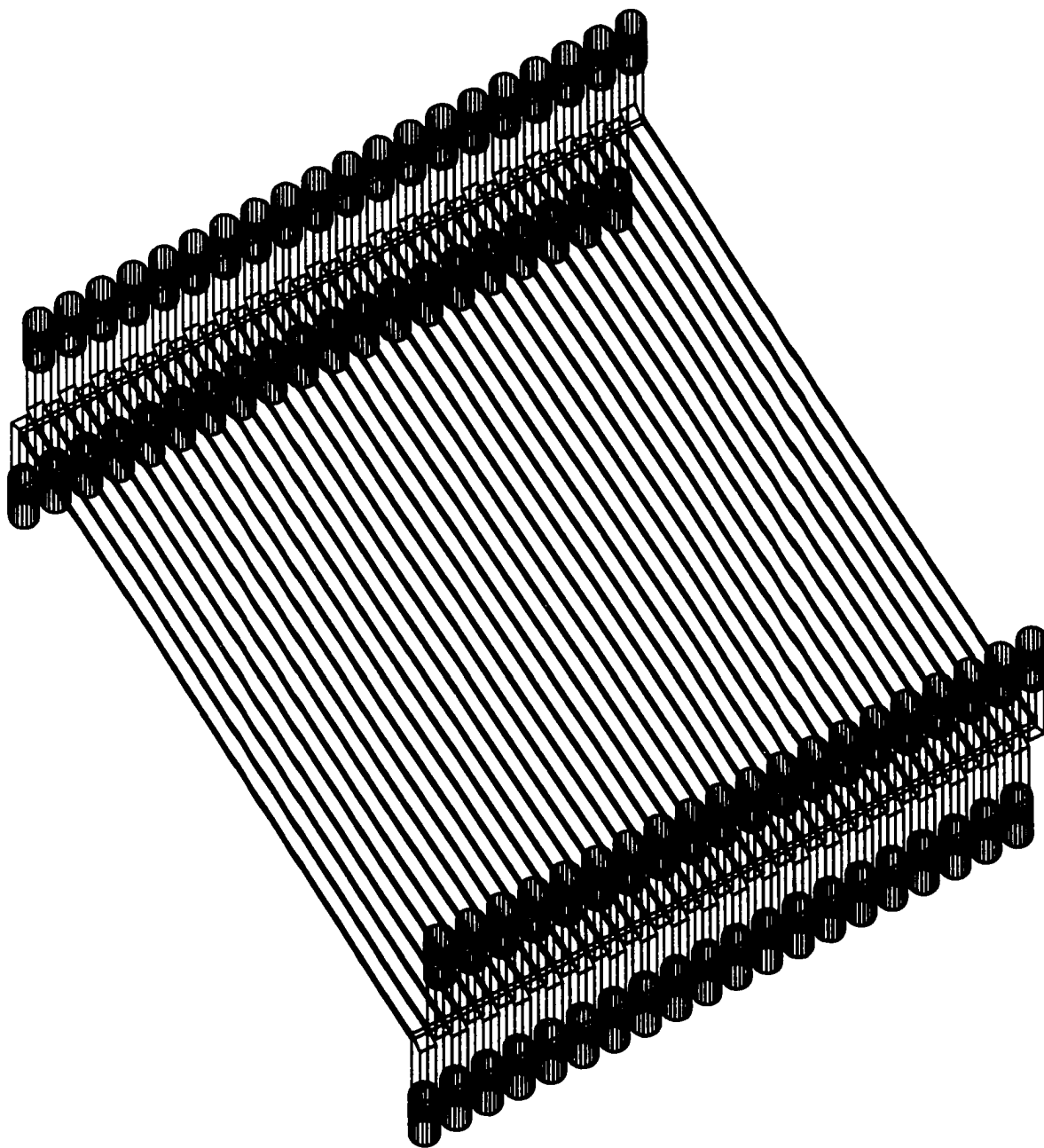


Figure 2.7 Part of the array of slats on hodoscope H1.

With it, independent estimates of mass were possible (i.e., independent of the mass measured by the tracking system). For a neutron, the mass could be found by assuming that most of the kinetic energy of the particle was converted into showers in the calorimeter. Using the relativistic expression for the kinetic energy, the mass of the particle is given by Eqn. 2.2.

$$m = \frac{E_{calo}}{\gamma - 1} \quad (2.2)$$

For \bar{p} 's, the annihilation energy would be added to the kinetic energy, yielding Eqn. 2.3.

$$m = \frac{E_{calo}}{\gamma + 1} \quad (2.3)$$

This allowed for the elimination of particles created downstream of the target that might otherwise have tricked the tracking system. It also provided the ability to measure particles of neutral charge. To do this, the tracking system was used to eliminate the charged background.

The calorimeter consisted of 58 x 13 towers (58 long and 13 high). The assembly was tilted 3.3 deg with respect to the beam direction, so that particles would not, in general, travel straight along the embedded scintillator.

The energy resolution of the calorimeter was given by Eqn. 2.4.

$$\sigma(E)/E = (3.5 \pm 0.5)\% + \frac{(34.4 \pm 0.8)\%}{\sqrt{E(GeV)}} \quad (2.4)$$

2.4 Trigger

The minimum bias experimental trigger determined the start of the gate for each event. Since collision products were already streaming through the detector by the time a trigger decision was made, delays were introduced in all the cabling so that the signals from the detectors would arrive within the interval of time that the gate was open. This is the reason, for example, that the MITCH detector's signals both contributed to the trigger decision, and recorded a non-zero TDC time. The signals had been split. Part went to the trigger decision logic, and the others were delayed, and wound up giving the stop signals to the two MITCH TDCs.

Table 2.4 Summary of calorimeter characteristics and performance. Table reproduced from reference(25). See this reference and Reference (26) for details on construction and performance and for a complete explanation of the quantities in the table.

Property	Value	Comments	Source
lead to fiber ratio	4.55:1	by volume	
# of interaction lengths	5.9		
Moliere radius	2.2 cm		
e/π	1.1	$2 < p < 4 \text{ GeV}/c$	test beam
noise equivalent	$< 18 \text{ MeV}$	per tower	1995 data
gain per ADC count	$6.33 \pm 0.11 \pm 0.12 \text{ MeV}$	$d @ 1.5 \text{ T field}$	1995 data
absolute energy scale	$\pm 3\%$		1995 data
$\sigma(E)/E$ for 5×5 array	$(3.5 \pm 0.5)\% + \frac{(34.4 \pm 0.8)\%}{\sqrt{E(\text{GeV})}}$	$1 < E_{kin} < 12 \text{ GeV}$	1995 data
containment	82%, 92%	$3 \times 3, 5 \times 5$ array	GEANT
high side tail	$e^{-1.63/\text{GeV}}$	$p @ 4\text{GeV}/c$	test beam
on deposited energy		4 orders of magnitude	
non-linearity	$< \pm 5\%$	$2 < p < 15 \text{ GeV}/c$	1995 data
$\delta m/m$	$0.026 + 0.347/\sqrt{E(\text{Gev})}$	$1 < p < 12\text{GeV}/c$	1995 data
TOF resolution	$< 400\text{ps}$	hadronic showers	1995 data
position resolution	$2.5 \pm 0.2\text{cm}$	energy weighted mean	1995 data
lateral shower profile	$r\rho(r) = B_1e^{-r/\lambda_1} + B_2e^{-r/\lambda_2}$ $B_1 = 0.055 \pm 0.021 \text{ GeV}/\text{cm}$ $\lambda_1 = 8.1 \pm 2.0 \text{ cm}$ $B_2 = 0.087 \pm 0.010 \text{ GeV}/\text{cm}$ $\lambda_2 = 3.26 \pm 0.43 \text{ cm}$	$p @ 6\text{GeV}/c$ $r = \text{radius in cm}$	test beam

E941 developed a two-level trigger system. The first level trigger was set by the MULT. The threshold on this detector was set low enough so that “any” minimum ionizing particle (MIP) could be detected. This adjustment was made by attaching an oscilloscope to the detector and setting the signal threshold below the easily observable MIP peak. In addition, the Cerenkov gas veto was not allowed to have triggered.

The second level of the two level trigger was determined by the LET electronics, but we didn’t use the LET in a very elegant manner. We ignored the timing information returned by the calorimeter, and fired whenever the energy in any calorimeter tower was above our minimum threshold. This threshold occurred at about 300 MeV.

Events that fulfilled both these criteria were termed LET triggers. “Scaler files” were kept for each run. In these scaler files information for each spill was recorded. In particular, the number of beam triggers (gbeam), number of min-bias triggers before “pre-scaling” (gint0), number of min-bias triggers after pre-scaling (gletint2), and number of those events that also satisfied the LET criteria (lettrig) were all kept for each spill. Utilizing a small program, we summed the spills to obtain for these numbers.

Roughly speaking, the rejection was equal to $gletint2/gletint0$. Unfortunately, the situation was not quite that simple because our minimum bias triggers were contaminated by a contribution from delta rays created in the target. This was the most significant correction to the total number of events sampled as obtained from the scaler files for the experiment.

The schematic of the trigger logic is displayed in Fig. 2.8 and Fig. 2.9.

2.5 Data Acquisition System

The data acquisition system (DAQ) was originally designed for A-A data runs. For these runs, the BNL-AGS supplied 4 second spills. Beam was supplied for 1 second, followed by 3 seconds of dead time (for a 1/4 duty cycle). The DAQ was therefore designed to record and buffer an entire spills data quickly, and use the dead time to process the data and build the events. A schematic drawing of the DAQ is given in Fig. 2.10.

Signals from the beam counters, hodoscopes, and calorimeters were digitized by 34 analog

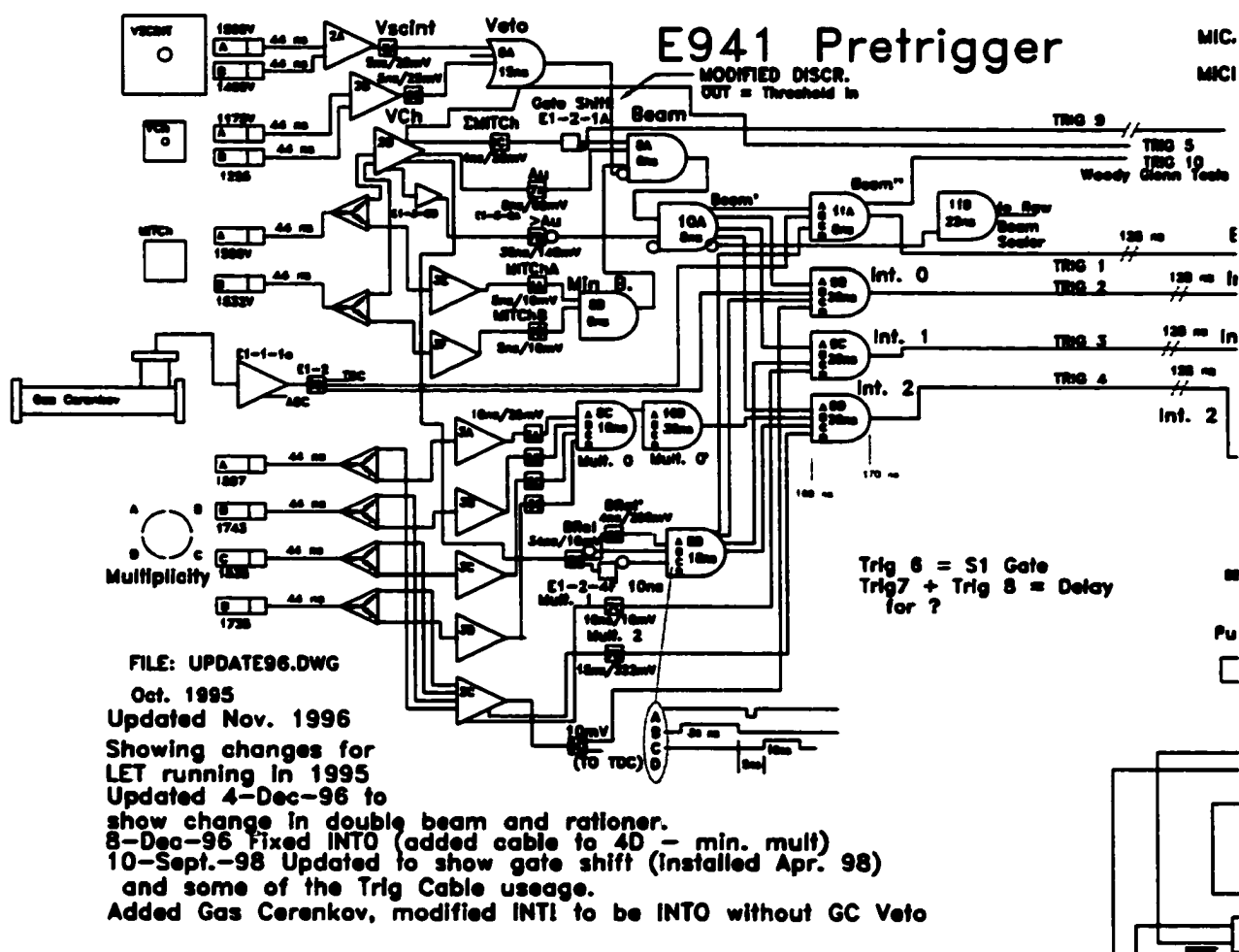


Figure 2.8 E941 pre-trigger logic diagram.

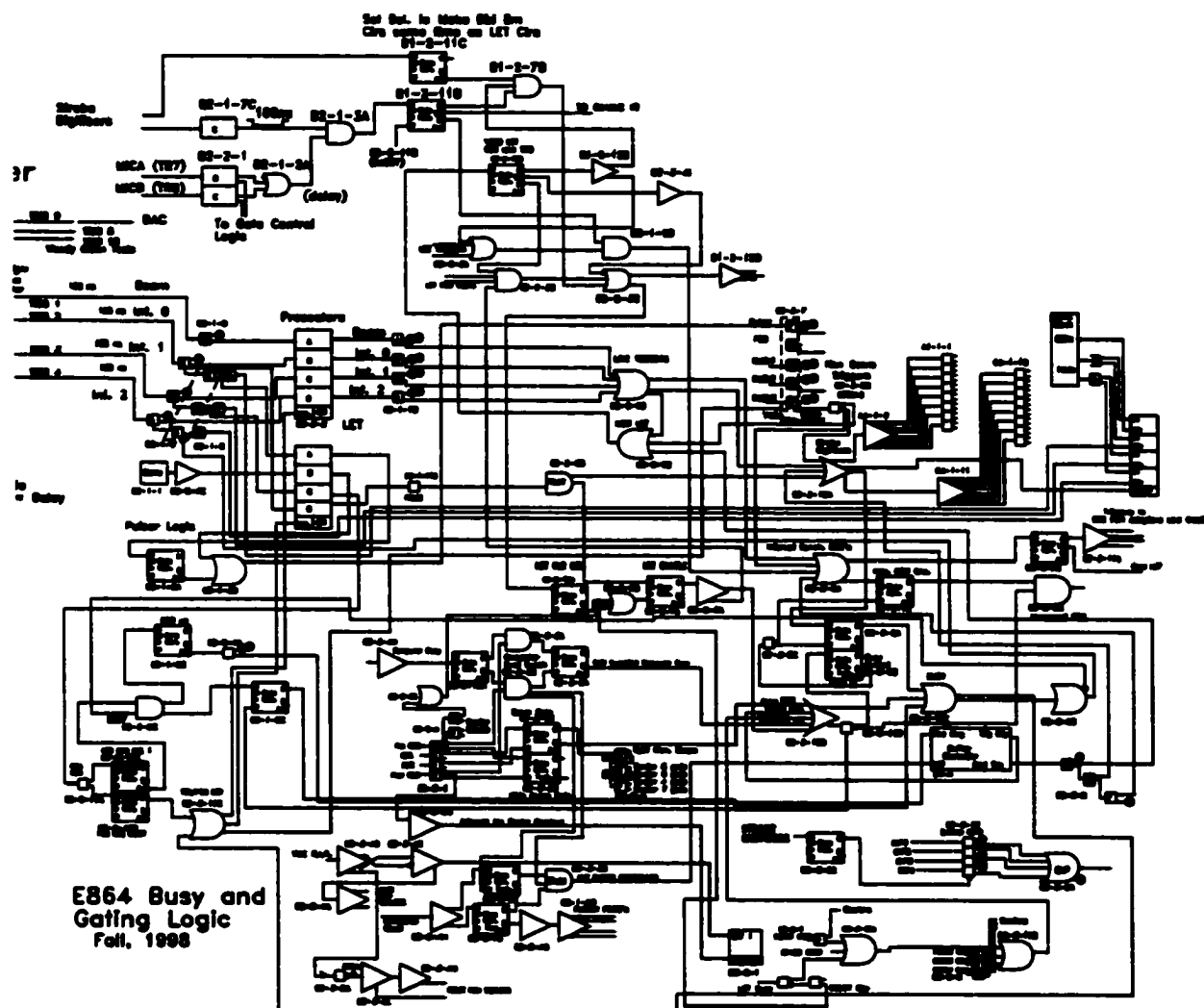


Figure 2.9 E941 trigger logic diagram continued.

to digital converter (ADC) modules and 34 time to digital converter (TDC) modules that were distributed in 4 Fastbus crates. LeCroy 1881 and 1881M ADC's and LeCroy 1872A TDC's were used for the job (29). Each of the modules had 64 channels, and each channel had 12 bit resolution (13 bits in the case of the 1881M). FASTBUS crate controllers transferred the information to separate VME memory buffers.

In parallel with this, straw tube hit information was read out with a LeCroy PCOS IV readout system (28). "Signals from the straws were shaped, discriminated and delayed (by a programmable amount) and latched on cards mounted on the detector" (27). After this, the data were collected and shipped by Fermilab SCC crate controllers to a multiplexer. The multiplexer was custom designed at Yale University. It combined the data streams from the four SCC's together and sent the stream to the VME memory buffer. In addition to the straw tube information, one of the SCC's contained trigger latch and event scaler data.

The VME system consisted of two types of VME processors: "memory buffers", and "event builders". There were 6 memory buffers attached to the data stream. Four were for the information from the Fastbus crates, one was from the multiplexer and one was from the late energy trigger.

The events were built using General Microsystems V49 modules. They were used to compile the event fragments into complete events and ship them through a SCSI port to the Exabyte 8505 8mm tape drives. One V49 module was used to control various data taking activities: starting runs, ending runs, enabling or disabling tape writing, etc.

A feature of the 1881 and 1881M ADC's that was used to decrease the overall size of the event was "zero suppression" for hodoscope ADC's. ADC digitizations below the pedestal levels for the hodoscopes were not read out. This feature was not used in the calorimeter, however, because very small signals were of potential use.

The data from events satisfying our triggering conditions were stored in the following way: Beam counter, hodoscope, and calorimeter ADC's and TDC's were read from four FASTBUS crate controllers onto separate VME memory buffers. The only subsystem whose data were not collected using the above mechanism was the straw tube stations. Straw tube information

was collected in CAMAC (along with other “descriptive” information). The CAMAC data were multiplexed into a single VME memory buffer. One final memory buffer received any information which was to be kept from the LET logic. Eight event builders gathered the event pieces from each memory buffer and output the data to individually controlled Exabyte 8mm dual density tape drives.

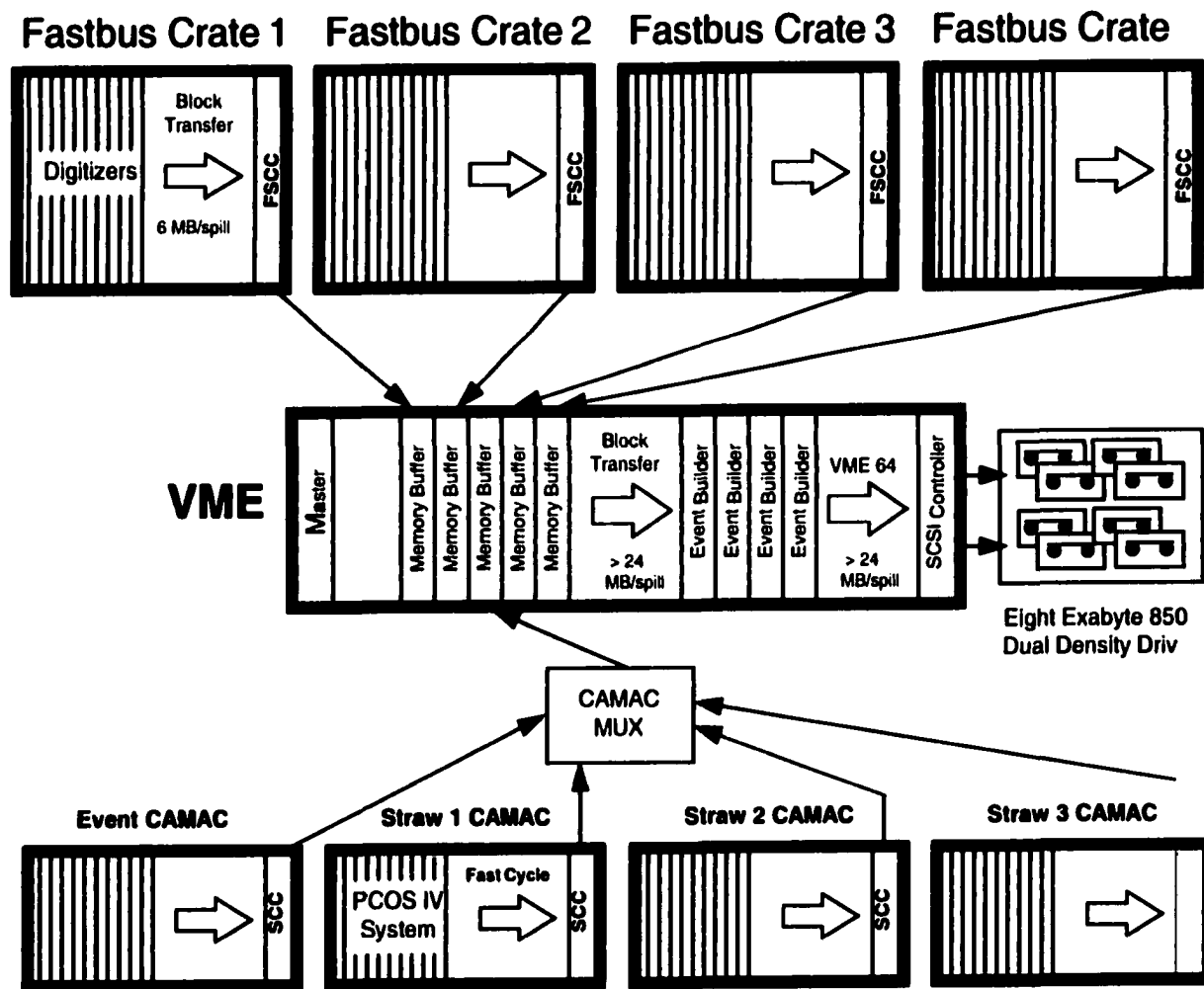
While, at the time of the design and implementation of the E864 DAQ, the 8mm tape drive system was the fastest affordable technology, they are, at this point in time, somewhat archaic. The biggest problem with the tape technology has been the degradation of the tapes with time and use. Several million events have been lost due to tape degradation in the original data tapes.

The DAQ was designed to be able to change the mixtures of event types. For the p-A running, beam triggers, int0, and lettrig events constituted the major trigger types. Taking a 19 GeV/c p+Cu run (Run 2044) for example, the ratios of trigger types for beam triggers to min bias triggers was 6.9. The ratio for prescaled min bias triggers to LET triggers was 8.1.

2.6 Design and Construction of MULT

This detector was designed and built by John Hill and me at Iowa State University. The design of the detector closely resembled the design of the multiplicity counter used in the earlier E864 A-A data runs. The reason for replacing the earlier multiplicity detector was that we wanted to detect collision products at smaller angles. The old angular coverage had run from 16.6 deg to 45.0 deg. The new multiplicity detector was designed with angular coverage between 5 deg and 45 deg. Another difference between the design parameters for the two counters was that a 90 % tungsten alloy (heavymet) shielding was placed in front of the old MULT to protect it from delta rays (defined earlier in this chapter) produced in the A-A collisions. Simulations of p-A collisions showed that this shielding was unnecessary in the p-A regime because the delta rays are a smaller effect. Furthermore, in p-A, the shielding would have adversely affected the performance of the interaction detector because the lower multiplicity environment of p-A required a more sensitive interaction detector.

Figure 2.10 Data acquisition system configuration.



As described earlier, MULT consisted of four quadrants. The design of one quadrant is shown in Fig. 2.11. Four Phillips 2 in. diameter XP2262B photomultiplier tubes were used in the construction of the counter. The bases and shields of the old MULT were used. This decision was advantageous because the old bases came with a sturdy, soft iron cases that blocked the phototubes from receiving light, and were spring loaded to press the phototubes firmly against the light pipes. BC-420 scintillator was used, just as it had been in the case of the earlier MULT detector. Care was taken to make sure that the phototubes were sensitive to the peak wavelengths emitted by the scintillator. For each quadrant, the entire phototube, light guide and scintillator were wound with electrical tape. The scintillator and the light pipe were first covered loosely with aluminum foil. The aluminum foil was not allowed to get too close to the phototubes, however, because of the risk of creating short circuits.

The detector quads were tested in several different ways. Green LED's were mounted inside each quad and run with a pulser to make sure that MULT was working. The pulser and LED's were also run for over a day to test the stability of the output. Using voltages of about -1500 V to power the tubes, the voltage necessary to keep the output pulse heights constant (to about 5 or 10 %) only varied by less than 10 V. In addition, an Sr-90 source was used to make preliminary tests. The width of the signal from Sr-90 source was about 25 ns. Stability tests using the Sr-90 source and an MCA showed the detector to be about 2 % stable over the course of an hour, but the tubes had started cold, and probably would have performed even better after some time. Finally, the two aspects of the detector were tested at BNL. First, any final light leaks were located and taped. Second, the stability of the detector was tested. This was done using secondary particles created in AGS spills. At the time, no beam was being diverted to E941, but the AGS spills created enough signal in our experimental hall to test the MULT counter. The 4 quadrants each easily detected the spills. The effect was used to gain match the 4 quadrants to each other.

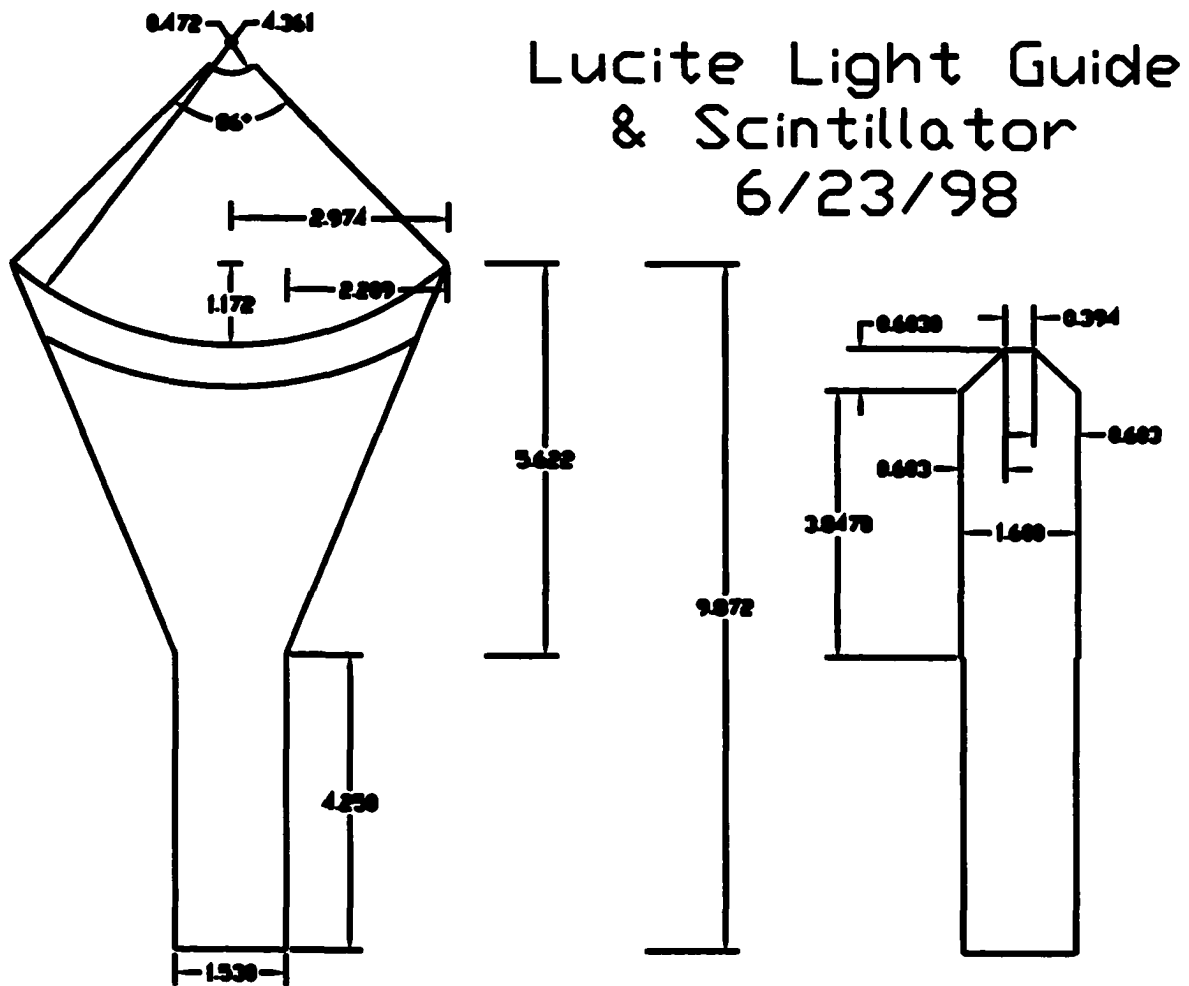


Figure 2.11 Specifications for the scintillator and lucite light pipe from one MULT quadrant. The units on the specifications are in inches.

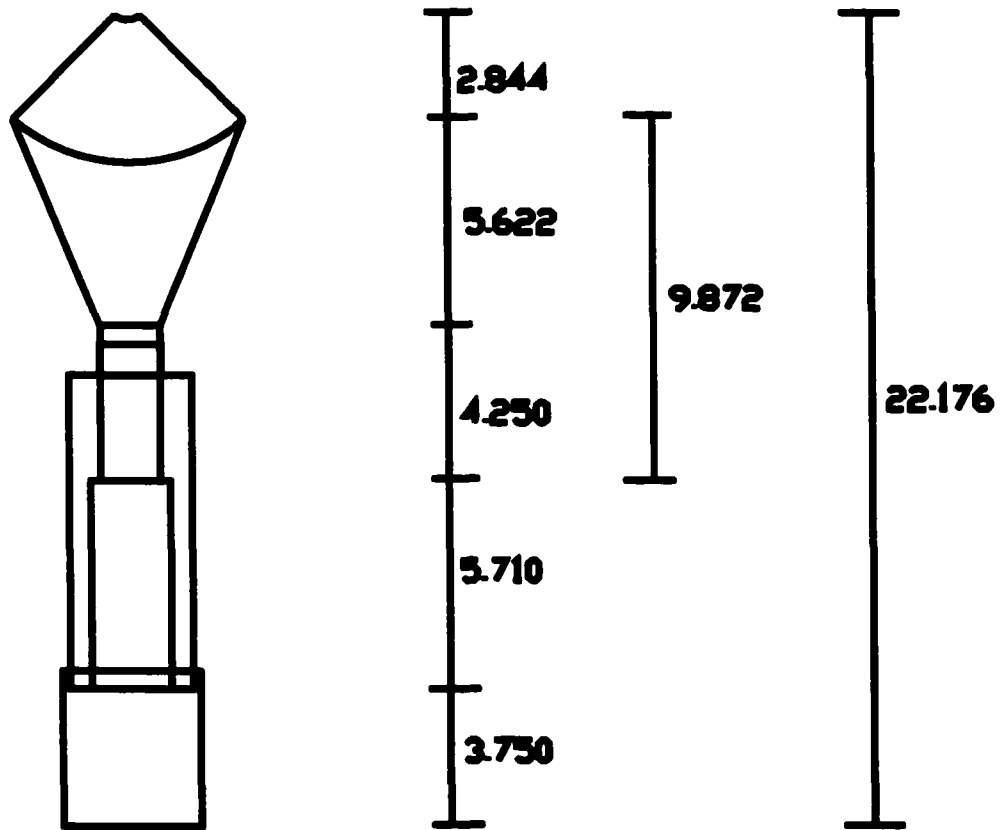


Figure 2.12 Specifications for one entire MULT quadrant, including the photomultiplier tube and base. The bases were spring loaded and came equipped with soft iron casings to surround the PMT's and part of the light pipe.

CHAPTER 3. CALIBRATIONS

3.1 Introduction.

In order to produce tracks, the detector was first calibrated. In order to calibrate the tracking system (which consisted of the beam counters, straw tube stations and hodoscope planes) only the hodoscopes and beam counters needed to be calibrated. The straw chambers did not require calibration. The straws only measured positions, and the positions that were deduced from them relied only on the geometry surveys for the experiment.

Calibrations fell into two categories: Those that needed to be done for each run, and those that only needed to be done when changing the fields on the dipole analyzing magnets. The "hodoscope slew time offsets" were particularly important since the hodoscopes were the key tracking detector, and the slew time offsets removed run to run fluctuations in the timing information.

Certain track parameters were easy to determine provided that the geometric surveys of the apparatus were correct. For example, the x position of particles traversing the hodoscope planes was determined by the slit that intersected the particle's trajectory. The segmentation of the hodoscopes provided the x position information. Timing data, on the other hand, had to be calibrated to be meaningful. The y position of tracks at the hodoscopes (which depended on the difference between the top and bottom PMT times) also had to be calibrated.

3.1.1 Computing

Both the act of calibrating the detector and analyzing the data required extensive computation. In order to accomplish this, an analysis shell called "sharc" was written in Fortran 77. The shell was implemented on both UNIX and VMS platforms. It was an extremely versatile

tool, because additional computer code could be compiled together with the basic shell to customize it for particular tasks. In addition, from within the shell, script programs (kumacs) could be run which directed the tasks performed by the shell. This analysis framework enabled the production of specific graphs and data structures. One common type of graph is the “histogram”. Histograms measure the frequency of occurrence of some quantity as a function of one or more parameters. The output of sharcs were designed to be compatible with a data analysis software package produced by CERN called Physics Analysis Workstation (PAW). This chapter describes how these various computing tools were applied to the raw data to create calibration files.

3.2 Time of Flight Calibrations Using the Tracking System

In a magical and perfect world, the TDC values returned by the electronics would always be directly proportional to times of flight. This is not, however, an ideal world, and four types of problems arose. The following timing calibration procedures were nearly the same for MITCH and the three hodoscope planes.

1. Hits that left large signals in the detector set off the discriminators before tracks that left small signals, i.e., the raw TDC values were pulse height dependent. The corrections for this effect were called, “slewing corrections”.
2. Environmental factors caused run to run differences in the amount of time that it took signals to travel from the detectors to the TDCs. This caused run to run variations in the TDC values. We called these corrections “slew time offsets” because TDC values were first slew corrected and then had an offset applied to them that made them consistent with all the other runs in the analysis.
3. The experimental gate was dependent on the amount of time it took the trigger to make a decision. This interval of time was not constant. The experimental gate did not occur at a fixed time after the collision. Fortunately, the fix for this problem was simply to

subtract the TDC time of the MITCH detector from the TDC time of any other detector. Since both times were dependent on the start of the gate, the effect was removed.

4. A constant had to be added to the slew corrected, slew time offset corrected TDC values so that they were proportional to the amount of time that has elapsed since the collision. The constants that were used for this were called t_{zeroes} .

Actually, for any given slat of the hodoscope, it was the mean time from the top and bottom PMT's that was related to the time of the hit. This is because the mean time was independent of the vertical position of the particle's hit. The TDC values from the top and bottom PMT's must both be slew corrected, and the slew time offset corrected before the t_{zeroes} can be found.

3.2.1 ADC pedestals for hodoscopes and beam counters

In order to perform the first correction, i.e., the slewing correction, the pulse heights had to be known. These were taken from the ADC values of the hits. That meant, however, that the ADC's had to be calibrated beforehand. To calibrate the ADC's, the PMT's responses were digitized when no particles were in the detector (pedestal events). The pedestals were then subtracted from the ADCs. The pedestal levels of the PMT's had to be determined before slewing corrections could be applied to the TDC values. Pedestal corrected ADC's were also used to calculate dE/dx and determine the charge of particles incident on the detectors.

3.2.2 Slew time offset corrections for hodoscopes and beam counters

Once the ADC values were pedestal subtracted, they were applied to parameterizations of the slewing effect and the raw TDC's were slew corrected. Run to run variations in the TDC values were then adjusted. This was done using features of TDC spectra from the slats and counters that were being calibrated. Features in these spectra that were caused by physical mechanisms that did not vary from run to run were used to make the TDC values from run to run consistent with each other. The calibration removed the run to run variations in the TDC measurements of these features. For example, the TDC spectrum of beam particles passing through the MITCH counter typically looks something like Fig. 3.1. In every run of

a given beam momentum, it took a fixed amount of time for a beam particle to go from the MITCH counter to the target, so the TDC spectrum should not shift position. It did, however, shift position because the environment changed the signal transit times. Shifting the peak of this distribution to zero for all runs calibrated the MITCH TDC values so that each run was consistent with the next. The same method was applied to calibrate the hodoscope slats. This procedure is illustrated in Fig. 3.2. In the figure, the two peaks represent two features in the TDC spectra of the apparatus. The first feature consists of the peak formed by the TDC mean times returned for beam particles traversing MITCH (again, as shown in Fig. 3.1). The second feature is the mean TDC spectrum of particles traversing one of the slats of one of the hodoscopes.

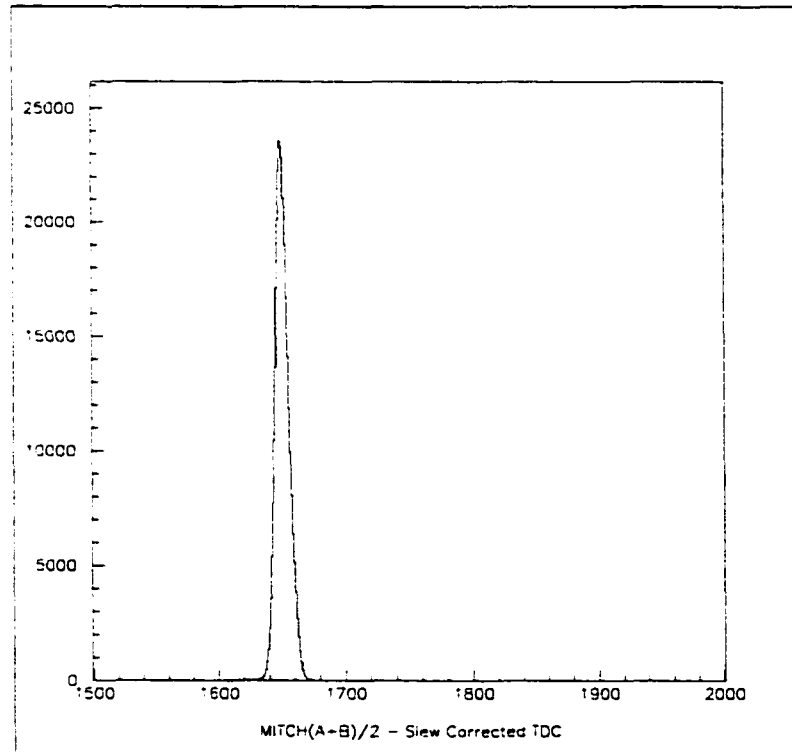


Figure 3.1 This is a plot of the mean TDC values from top and bottom phototubes of the MITCH detector. The TDC values for each tube were first "slew" corrected. The next step consisted of determining offsets for each tube that would shift the mean position to 0. This calibration constant was referred to as the MITCH "slew time offsets". The word slew is included because the TDC values were slew corrected.

Incidentally, one might wonder how the MITCH counter signal both influences the trigger decision, and yields a TDC value greater than zero. The answer is that delays are built into the cabling of the experiment so that the part of the signal that is split and goes to the TDC takes longer than the trigger decision that uses the other part of the signal. The trigger starts the TDC's running, and the arrival of the timing signal from the detectors stops them.

As long as both these features had a fixed time relationship with respect to the collisions in the target, they could be used for the slew time offset calculation. It was not important what the difference in time was between the arrival of particles at MITCH and the arrival of secondary particles at the hodoscope slat. All that mattered was that these times were fixed relative to the collisions. In fact, both peaks were offset to zero, so the time interval between the passage of beam particles through MITCH and the traversal of particles through the hodoscope slats was zero in TDC units. To that point in the calibration, all that has been achieved was to make each run consistent with the next. It still remained to add another constant to each hodoscope slat that would cause the TDC interval to be proportional to the time of flight.

The time of flight for a particle to travel from the target to a given hodoscope slat is given by Eqn. 3.1

$$t = 25ps * (\frac{TDC_{top} + TDC_{bottom}}{2} - TDC_{beam} + t_{zero}) \quad (3.1)$$

where all the TDC values are slew corrected and slew time offset corrected, and TDC_{beam} is actually the slew corrected, slew time offset corrected $\frac{TDC_{MITCHtop} + TDC_{MITCHbottom}}{2}$. The reason for subtracting off TDC_{beam} is that it has the same gate dependence as TDC_{top} and TDC_{bottom} , so that variations in the experimental gate were removed.

3.2.3 Time zero calibrations for hodoscopes

Once the slew time offsets had been applied to TDC times, all the runs were calibrated with respect to each other, but the time of flight was still unknown. The t_{zero} in Eqn. 3.1 is the additive constant that, when added to the slew corrected, slew time offset corrected TDC yields a number proportional to the actual time of flight.

Time of Flight Calibrations:

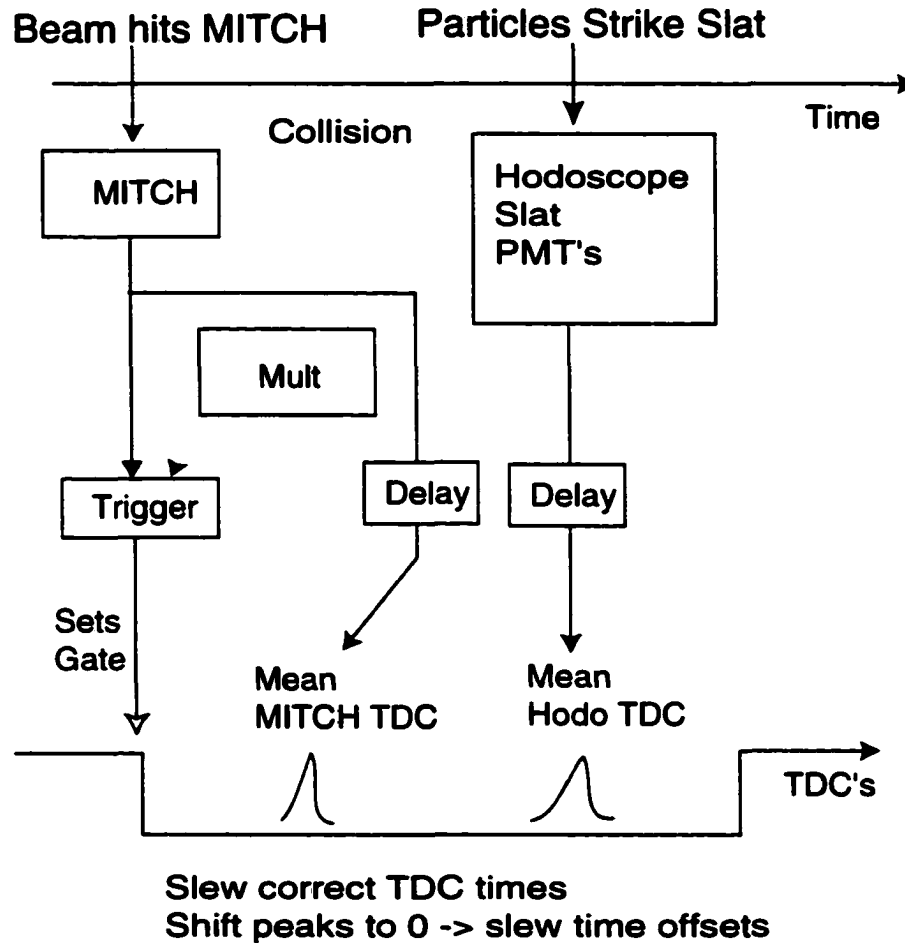


Figure 3.2 The schematic above illustrates how the fixed time of two features of the TDC spectra was used to calibrate runs with respect to each other. The raw values were corrected for "slewing" effects, and for run to run variations in the signal transit times between the detectors and the TDC electronics. The peaks of the mean TDC spectra were shifted to zero. Once the offset for the distributions was determined, it remained to determine the value of a new constant that when added to the slew corrected slew time offset corrected hit TDC's, yielded a number proportional to the time of flight.

In order to determine the t_{zero} constants for each hodoscope slat, guesses were initially made as to their proper values and then tracking using loose cuts was performed on the data. (The experiment was mature by the time that E941 started taking data, so rough t_{zeroes} were available (at least for the -0.2 T field setting of the magnets). For their first run, E864 estimated their first round of t_{zeroes} from a Monte Carlo simulation. Using rough estimates for the t_{zeroes} , some tracks were identified. Given the particle species of the track, its pathlength and momentum, the time of flight was calculated. The old t_{zeroes} were adjusted by an amount equal to the difference between the time of flight as derived from the track fit, and the time of flight used to create the track fit. This process was iterated until the difference in time became negligible. Since the slew time offsets took care of run to run variations, the t_{zeroes} only needed to be recalculated when using different field strengths on the analyzing magnets. (Actually, since the MITCH mean TDC times were subtracted from the hodoscope mean TDC times, the beam momentum, in principle, also affected the time calibrations. Higher momenta beam particles took less time to reach the target. The difference in times, however, is just 10 ps, which is a bit below the timing resolution of the experiment and can therefore be ignored.)

3.3 Y Offset Calibrations for Hodoscopes

The y position of particles as they traversed the hodoscopes remained to be calibrated. Like the t_{zero} calibrations, the y position calibrations required reconstructed tracks. Since the y positions of particles at the hodoscopes were determined using the difference in time between the top and bottom PMT signals, the TDC's had to be slew corrected and slew time offset corrected first. As in the t_{zero} case, the y offsets were determined using an iterative process. The y position of the tracks as determined from the track fit was compared to the y position used to derive the track fit and the difference was used to adjust the y offsets.

3.4 Steps Used to Derive the Calibration Constants

Earlier E864 graduate students broke the task of creating the calibration files into 6 phases. The recipe they adopted was as follows:

1. Phase 1: ADC pedestal levels. As described earlier, in order to evaluate any of the timing calibration constants, the ADC pedestal levels had to be known (so that slewing corrections to the TDC's could be applied). The pedestal levels of the ADCs on the beam counters, hodoscopes, and calorimeter were found in this first phase. Histograms were also created to eliminate the effects of 60 Hz. noise on the beam counters ADC's (see Fig. 3.3). In order to remove the effects of this noise, the beam counter ADC pedestal subtraction had to be time dependent. A microsecond counter was included in the data stream, and each cycle (lasting 1/60th) of a second was broken up into 100 bins (so, each bin was 166 μ s wide). The pedestal events were binned according to the phase in the cycle in which they were taken, and the ADC's were plotted as in the figure. A weighted average of 40 ADC bins centered on the bin with the most hits was calculated and this number was used to pedestal subtract all events that occurred at that phase in the noise.
2. Phase 2: Laser calibration of fluctuations in the calorimeter gains. These were studied by Evan Finch, and on his advice, this step was skipped because it did not substantially change the values returned.
3. Phase 3: Beam counter time offsets. Peaks in the slew corrected timing distributions of the beam counters were fit, so that the TDC levels could be offset to zero. Note that while the TDC's from the MITCH counter were slew corrected, those from the MAC counter were not. This is because the MAC counter's timing was not required to be particularly accurate, but MITCH's timing was very important. A preliminary list of bad hodoscope slats was created based on various sorts of pathological output from the ADCs or TDCs.
4. Phase 4: Hodoscope slew time offsets. Peaks in the slew corrected TDC distributions were fit (just as they had been in the beam counters). The fits to these peaks were used to create "slew time offsets" for the hodoscopes just as was done in phase 3 for the beam counters. A more complete list of bad hodoscope slats was produced, and slew time offsets were created for the calorimeter towers as well.

5. Phase 5: Fine tuning of the hodoscope slew time offsets. Histograms were created so that the slew time offsets for the top and bottom PMTs of each slat in the hodoscopes could be adjusted to yield a mean time of zero. In order to get these mean times within 100 picoseconds of zero, this phase had to be iterated 2 to 4 times. That is, the mean times from the top and bottom PMT's of each slat had to be plotted. A Gaussian was fit to the peak of each distribution, and the slew time offsets for the top and bottom PMT's were adjusted by small amounts so that the peak for the mean time would be centered closer to zero on the next iteration.
6. Phase 6: Final hodoscope t_{zeroes} and hodoscope y offsets were calculated. As described earlier, tracks were needed to adjust these calibration constants.

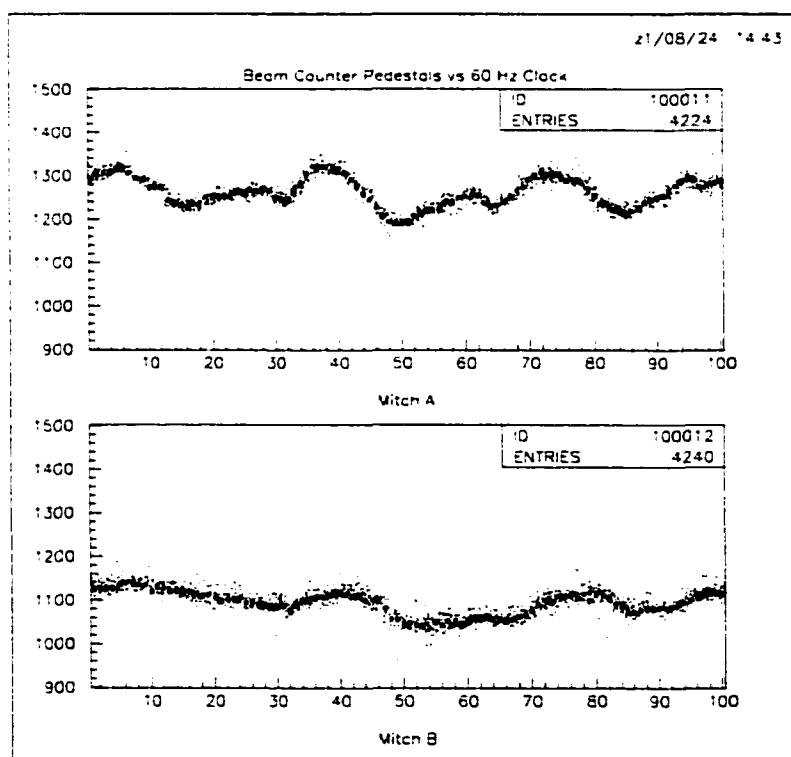


Figure 3.3 This figure shows the 60 Hz noise on the the MITCH beam counter. ADC values from pedestal events are binned according to the phase of the cycle in which the event was taken. Similar noise affected the MULT counter ADC readouts.

CHAPTER 4. INVARIANT MULTIPLICITIES

In this chapter, the method used to produce the \bar{p} invariant multiplicities will be explained and the results from the application of the method presented. Once the calibration files were created (as described in chapter 3) the raw data tapes from the experiment were examined and the trajectories of particles through the detector (tracks) were reconstructed. Various cuts were applied to the tracks to determine those that should be included in smaller files, called "ntuples". The ntuples were subjected to a final set of cuts to reduce backgrounds and the remaining tracks were divided into bins according to their y and p_T . Mass histograms were created for each y and p_T bin. The \bar{p} peak in each histogram was fit and background subtracted. The background subtracted integral of the fits yielded the number of counts in each y and p_T bin. After various corrections (which will all be explained in this chapter) these counts were used to generate the invariant multiplicities.

4.1 Reconstructing Tracks and Determining Masses.

The process of reconstructing tracks (tracking) consisted of connecting space-time hits in the detectors. Straight line fits to the hits were constructed downstream of the magnets, and the timing information and the assumption that the track originated at the target constrained the tracks upstream of the magnets. Within the region of the magnets, however, the trajectories of the charged particles were curved. The straightness of this curve is referred to as the "rigidity" (R) of the track, and it is defined by Eqn. 4.1.

$$\bar{R} = \frac{\vec{p}}{z} \quad (4.1)$$

Here, " \vec{p} " is the total 3-momentum and " z " is the charge. The rigidity required to connect

the upstream and downstream portions of each track's trajectory was deduced using a lookup table. The charge of the tracked particles was determined using the energy deposition $\frac{dE}{dx}$ in each of the hodoscope planes. Particle speeds were determined by combining the track fit with timing information from the hodoscopes and the beam counters. From the timing information and track fit, the β and γ of each track were determined, where $\beta = \frac{v}{c}$ and $\gamma = \frac{1}{\sqrt{1-\beta^2}}$. Given the measurements of the rigidity, charge, β and γ of each track, the mass was calculated, using Eqn. 4.2.

$$Mass = \frac{Rz}{\gamma\beta} \quad (4.2)$$

4.2 Creating Ntuples.

The ntuples used in this analysis are essentially tables in which each column corresponds to a track, and each row contains kinematic information about the track. The ntuple files are about 10 times smaller than the files on the raw data tapes that were analyzed to produce them. In order for tracks to be included in the ntuple they had to pass charge, quality of track fit, and kinematic cuts. In addition, the tracks had to point to towers in the calorimeter in which energy had been deposited. Each of these cuts will now be described.

4.2.1 Charge.

The ntuples used were designed to store information only on negatively charged tracks. The sign of the charge was determined by the direction of the bend of the track as it traversed the magnetic field. The magnitude of the charge was determined using the average of three independent measurements of $\frac{dE}{dx}$. One measurement was made in each hodoscope plane using Eqn. 2.1. While the magnitude of the charge was not used to determine whether the track was included in the ntuple, the values from each hodoscope plane were stored in the ntuple, and only tracks corresponding to charge measurements between -0.7 and -1.8 (where -1 corresponds to the charge of an electron) were included in the final mass histograms. The ntuples, however, only cut positively charged tracks.

4.2.2 Quality of the track fit.

In order to eliminate tracks that were reconstructed from unrelated hits in the detector or from particle trajectories that did not originate at the target, tests of the quality of the fits were designed. Recall the coordinate system defined in Chapter 2. Since straight lines were fit to the spatial part of the track downstream of the magnets, The x position vs. the z position of the track should be linearly related. The y position vs. the z position should also be linearly related in that region. The y position vs. the pathlength should be linearly related throughout the detector, because the y direction is aligned with the magnetic field and therefore is unaffected by it. Similarly, the y position vs. time should also be linearly related throughout the detector. The “goodness of fit” parameter (χ^2) returned from these linear fits gives some estimate of the quality of the track fit. In order to perform a linear fit, at least two points are needed. Any extra points constitute extra degrees of freedom in the fit. The χ^2 values returned from these fits were divided by the number of degrees of freedom in the fits. χ^2 values divided by the number of degrees of freedom are called “reduced” χ^2 ’s. Statistically, if the distance between the fit and the fit points are distributed like a Gaussian, then one would expect about 2/3 of the fit points to be within 1 standard deviation of the fit. In that case, the reduced χ^2 should be close to 1. The χ^2 cuts applied to the data are given in Table 4.1. Note that the y position vs. z position has a very loose cut on it. This is because this fit is not independent of the others and we, therefore, did not want to constrain the tracks using this parameter.

One somewhat alarming plot that was automatically created with each ntuple was the vertical distance from the target to the track projection. This plot showed a background of tracks whose y positions at the target deviated from 0, i.e., they did not point back to the target. Fortunately, most of the tracks with intercepts far from the target were eliminated by the other cuts in the analysis. The ‘before’ and ‘after’ situation is illustrated in Fig. 4.2. To create the ‘before’ plot, the intercepts from all the tracks of one ntuple were plotted. This particular ntuple came from the analysis of a few million Pb events at 19 GeV/c. The ‘after’ plot was made by plotting intercepts after the final set of tracking cuts had been executed.

Table 4.1 χ^2 cuts. Most tracks put hits in 5 detectors. Since only two detector hits are required for a linear fit, the number of degrees of freedom in the fits were equal to the number of detectors used minus the 2 points needed for fitting. The χ^2 cuts were set at 3 for all of the fits except y vs. pathlength. This cut was loose because it was not independent of the other 3 χ^2 cuts.

Parameters	Degrees of Freedom	χ^2 cut
x vs. z	Max. of 5 detectors - 2 pts. = 3	3
y vs. time	3 hodoscopes + start time - 2 pts. = 2	3
y vs. pathlength	Max of 5 detectors + target pt. - 2 pts. = 4	3
y vs. z	Max. of 5 detectors - 2 pts. = 3	10

All tracks within the kinematic range of this analysis and within 2σ of the fits to the final mass peaks were included. All the ntuples used to analyze the Pb, 19 GeV/c data were used to create the 'after' plot.

4.2.3 Kinematic cuts

A β cut was placed on the tracks of .9995. This meant that all the tracks included in the ntuple had to have speeds less than 0.9995 times the speed of light. An even more stringent kinematic restraint was that only candidates with rapidities between 1.2 and 2.4 were stored in the ntuple. Using the relationship given by eqn. 4.3 and eqn. 1.10, an \bar{p} with $y=2.4$ and $p_T=0$ GeV/c has $\beta=0.9834$, and with $p_T=400$ MeV/c has $\beta=0.9862$. These are the upper ranges of β with which I will be dealing. The β ranges for the kinematic ranges I will be measuring are given in Table 4.2. The longitudinal component of β can be found from the definition of rapidity given in Eqn. 1.10. The transverse component of β is given by Eqn. 4.3. The two components can then be combined to give the total β found in Table 4.2.

$$\beta_T = \sqrt{\frac{(1 - \beta_z^2)(p_T c)^2}{m c^2 + (p_T c)^2}} \quad (4.3)$$

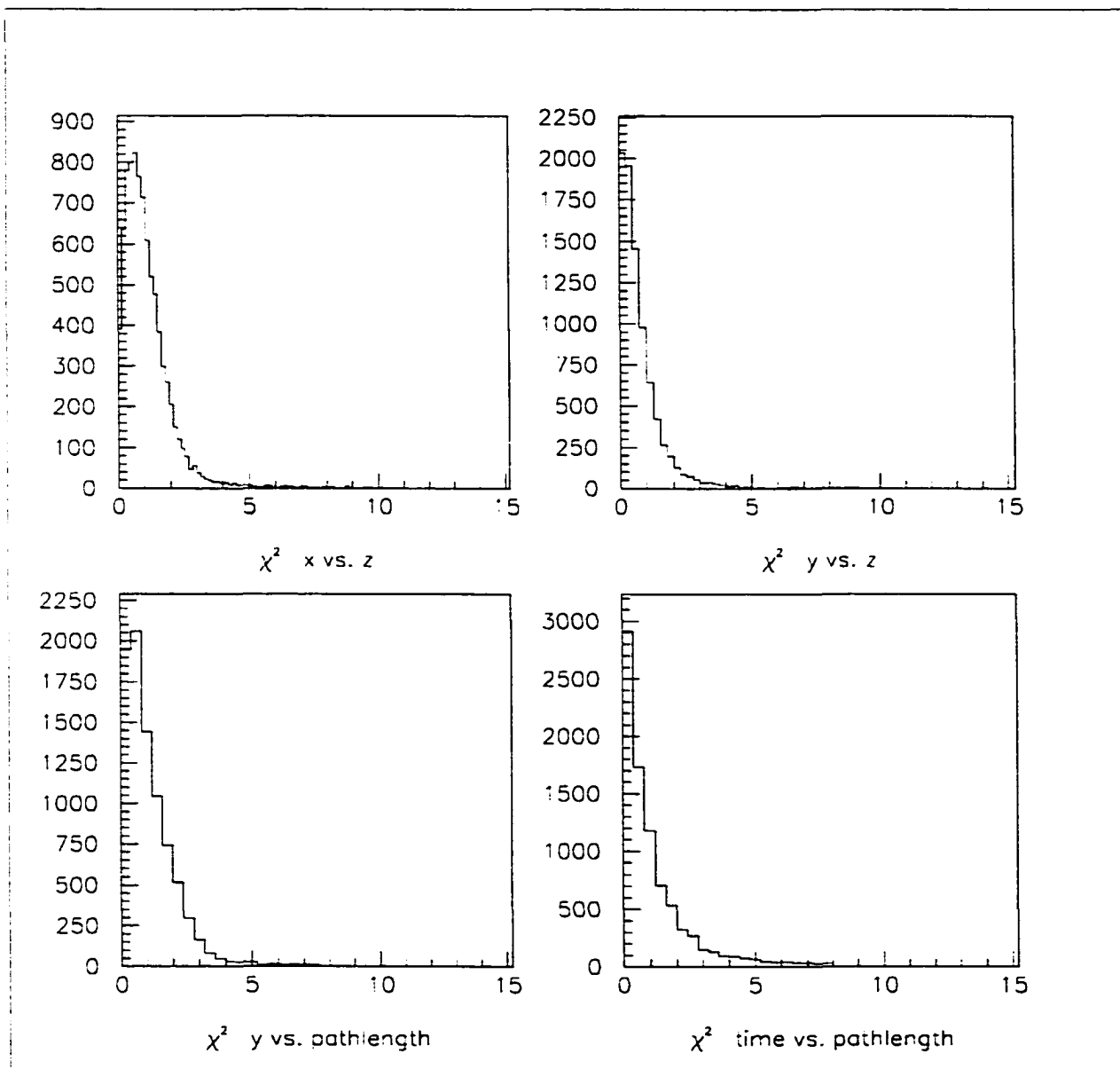


Figure 4.1 Plots of χ^2 distributions of fits to tracks from one ntuple containing tracks from the Pb, 19 GeV/c, -0.2 T data.

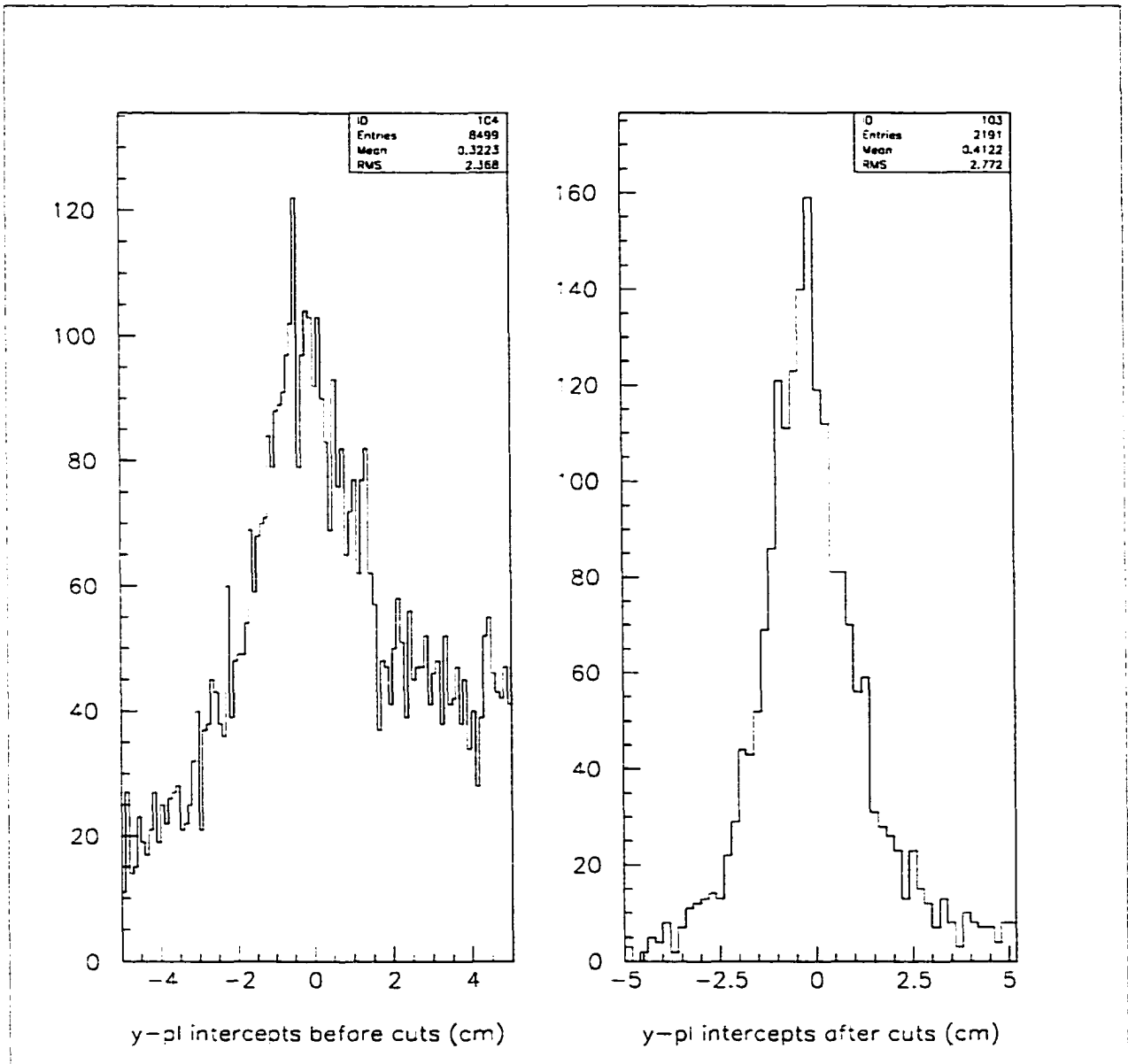


Figure 4.2 Comparison of the vertical position of tracks at the location of the target in an ntuple (y-pl intercept) before final cuts and after final cuts.

Table 4.2 Table showing maximum beta for each y and p_T . Notice that the beta cut placed on the ntuple 0.9995 exceeds the kinematic range in which I measured.

p_T in MeV/c	100	150	200	250	300	350	400
y							
1.4	0.8867	0.8884	0.8906	0.8934	0.8966	0.9001	0.9039
1.6	0.9226	0.9237	0.9252	0.9271	0.9292	0.9316	0.9341
1.8	0.9474	0.9482	0.9492	0.9504	0.9519	0.9535	0.9552
2.0	0.9644	0.9649	0.9656	0.9664	0.9674	0.9685	0.9696
2.2	0.9760	0.9764	0.9768	0.9774	0.9780	0.9787	0.9795
2.4	0.9839	0.9841	0.9844	0.9848	0.9852	0.9857	0.9862
2.6	0.9892	0.9893	0.9895	0.9898	0.9900	0.9904	0.9907

4.2.4 Calorimeter cuts

The track had to intersect the calorimeter such that the hit was within 20 cm (in each of the vertical and horizontal directions) of a shower. Also the total cluster energy was constrained to be above 900 GeV/c for both the 19 GeV/c and 12 GeV/c beam momenta.

4.2.5 Sample mass plot from the ntuples

As described above, the ntuples contained information on all negatively charged tracks. Essentially, this meant that the ntuples I created held information on the tracks from K^- , π^- , and \bar{p} 's.

An example of a mass plot produced using the entire y and p_T phase space within E941's acceptance is shown in Fig. 4.3.

4.3 Mass Histograms and Peak Fitting

After the ntuples were created, mass histograms were generated. All the ntuples for a given target, beam momentum and magnetic field setting were analyzed. Mass histograms were then generated for each y and p_T bin. The mass histograms were formed subject to the following cuts:

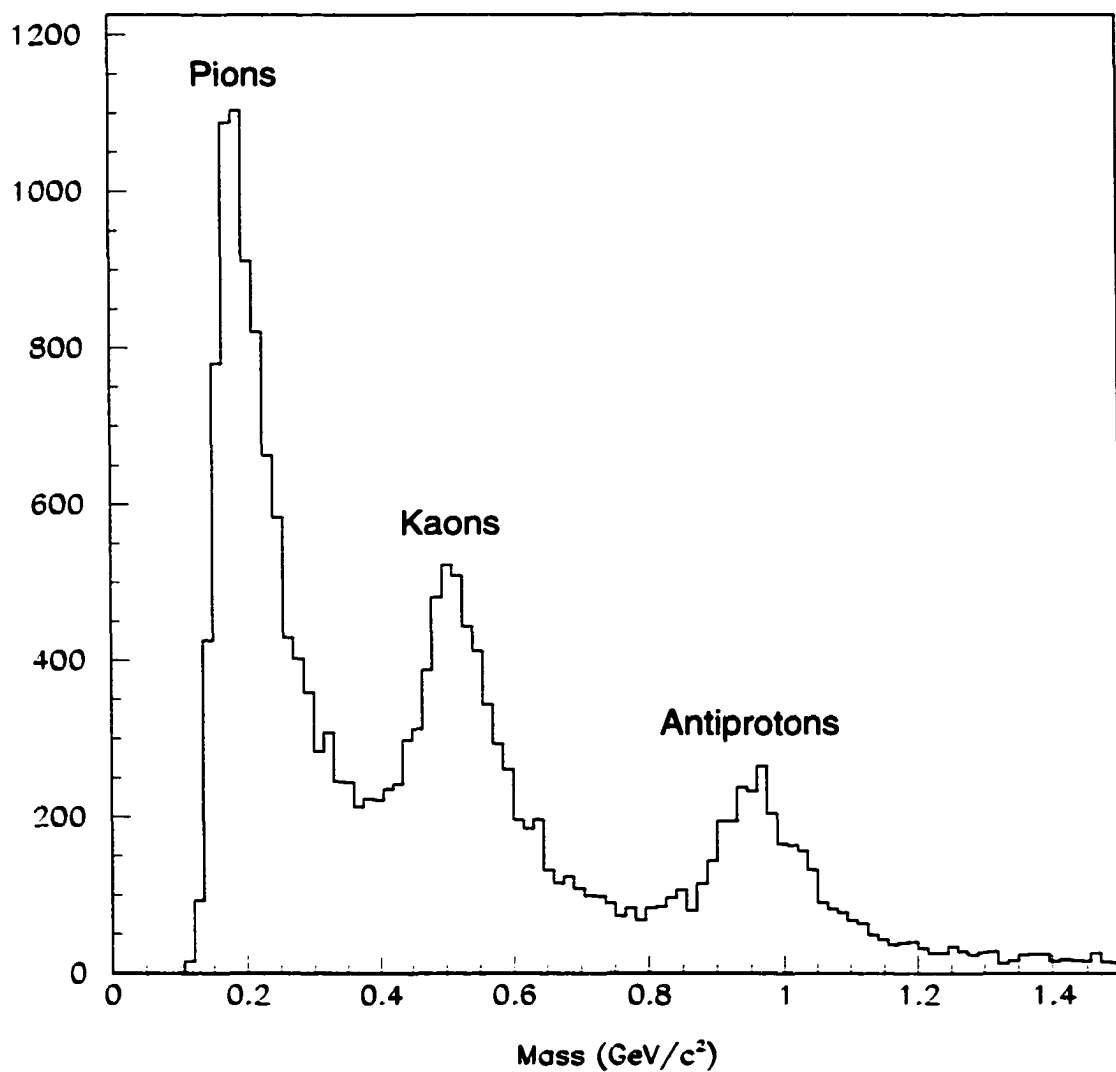


Figure 4.3 Typical mass plot of the combined Be data at 19 GeV/c. The \bar{p} , kaon, and (truncated) pion peaks are easily discerned.

Table 4.3 Second round cuts, namely those performed at the time of the creation of mass histograms.

Quantity	Cuts
y	Accept $\Delta y = 0.2, 1.4-2.4$
p_T	Accept $\Delta p_T = 0.050 \text{ GeV}/c, 50-350 \text{ GeV}/c$
χ^2 x vs. z	Cut if greater than 3
χ^2 y vs. pathlength	Cut if greater than 3
χ^2 time vs. pathlength	Cut if greater than 3
Calorimeter energy cluster	Cut if less than 900 MeV

4.3.1 Fitting the mass peaks

After the mass histograms were created from the ntuples, the \bar{p} 's were counted. Each mass histogram ranged from 0 to 1.5 GeV, and had 100 bins. Thus, the bin width for the masses was 15 MeV per bin. The widths of the mass peaks were at least twice this, so, the bin width was smaller than the mass resolution. For many of the mass histograms, the backgrounds at the \bar{p} mass were small, and, judging by the shape of the backgrounds away from the \bar{p} peaks, were fit well by a straight lines. Therefore, the peaks were fit with a composite function that consisted of a Gaussian plus a linear function. The area under the linear part of the fit was assumed to be background and the the rest of the integral was assumed to be from \bar{p} 's. For the Gaussian, there were 3 parameters: one related to the height, one for the width, and for the mean position. For the line, the parameters were the slope and the y-intercept. All together, the fits had 5 parameters. More specifically:

1. $P1 = \frac{A}{\sigma\sqrt{2\pi}}$, where A is the height, and σ is the standard deviation. Therefore, the height can be found from P1 and P3 (defined below).
2. P2 is the mean.
3. P3 is the standard deviation, σ .
4. P4 is the y-intercept of the linear fit.
5. P5 is the slope of the linear fit.

The fits are presented in Figs. 4.4 to 4.18. For rapidities 1.5 and 1.7, the statistics are comparatively good. For rapidities 1.9, 2.1, and 2.3, the statistics are best at lower p_T . Therefore, when the final invariant multiplicities were obtained from these counts, comparisons across rapidity at fixed p_T of 125 MeV/c yielded the highest precision trends.

The \bar{p} peaks in the mass histograms reveal two systematic effects. First, there was a systematic shift of the peaks to higher masses as a function of p_T . Second, there was a slight shift down in mass as a function of rapidity. These shifts are plotted in Fig. 4.19. As the plot shows, the p_T dependence was the dominant systematic. In order to investigate the source of the peak shifts, Monte Carlo simulations of \bar{p} 's created in the target were studied and tracked through our detector. It was found that peak shifts occurred in the measurement of the Monte Carlo events as well. Initially, it had been feared that the peak shifts were the result of incorrect calibration files, but since the calibrations do not affect the monte marlo simulation (so long as the same calibration files are used both to simulate the trajectories and reconstruct the faked data) the effect had to be explained by some other mechanism. The best explanation appears to be that, as we measured at higher and higher p_T , more and more of the \bar{p} 's were blocked by the collimators that limited the geometric acceptance. This cut into the mass peaks of the \bar{p} 's asymmetrically (i.e., the low mass side of the peaks was cut off more than the high mass side) and shifted them. The effect was enhanced at the extreme ends of our p_T acceptance because it is there that the collimators began to cut into our acceptance. To make matters worse, the mass peaks became a little wider at high p_T . This enhanced the peak shifting. While the analysis of the Monte Carlo showed that the acceptance calculation provided some correction for the problem, it was far from perfect because the peak shifts in the Monte Carlo were not as extreme as those in some of the data. A systematic error was estimated when the peaks were fit, but this systematic is ascribed to the fitting procedure, not inexact acceptance calculations. Still, the error bars ascribed to the high p_T data points were large and fairly conservative.

The shifts became smaller above rapidity 2.0. This was because, as particles' trajectories became more stiff, small transverse changes in the momenta had a diminishing effect on the overall trajectories. As a result, the kinematic acceptance opened up to a wider range of

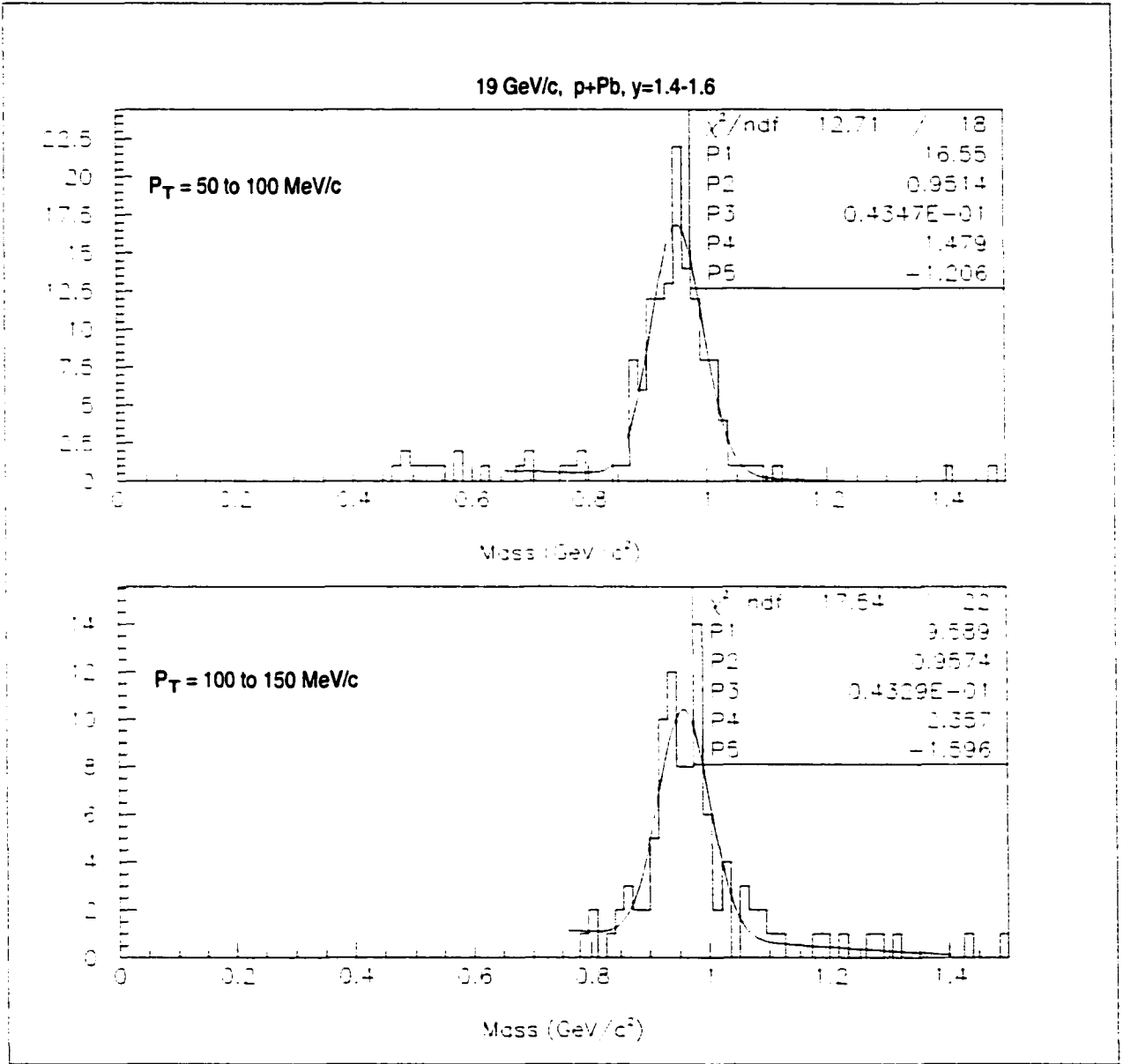


Figure 4.4 Mass histograms and fits for \bar{p} 's with rapidities from 1.4-1.6. The plot on the top is for $p_T = 50$ -100 MeV/c. The plot on the bottom is for $p_T = 100$ -150 MeV/c. These fits are for the 19 GeV/c, -0.2 T data with the Pb target.

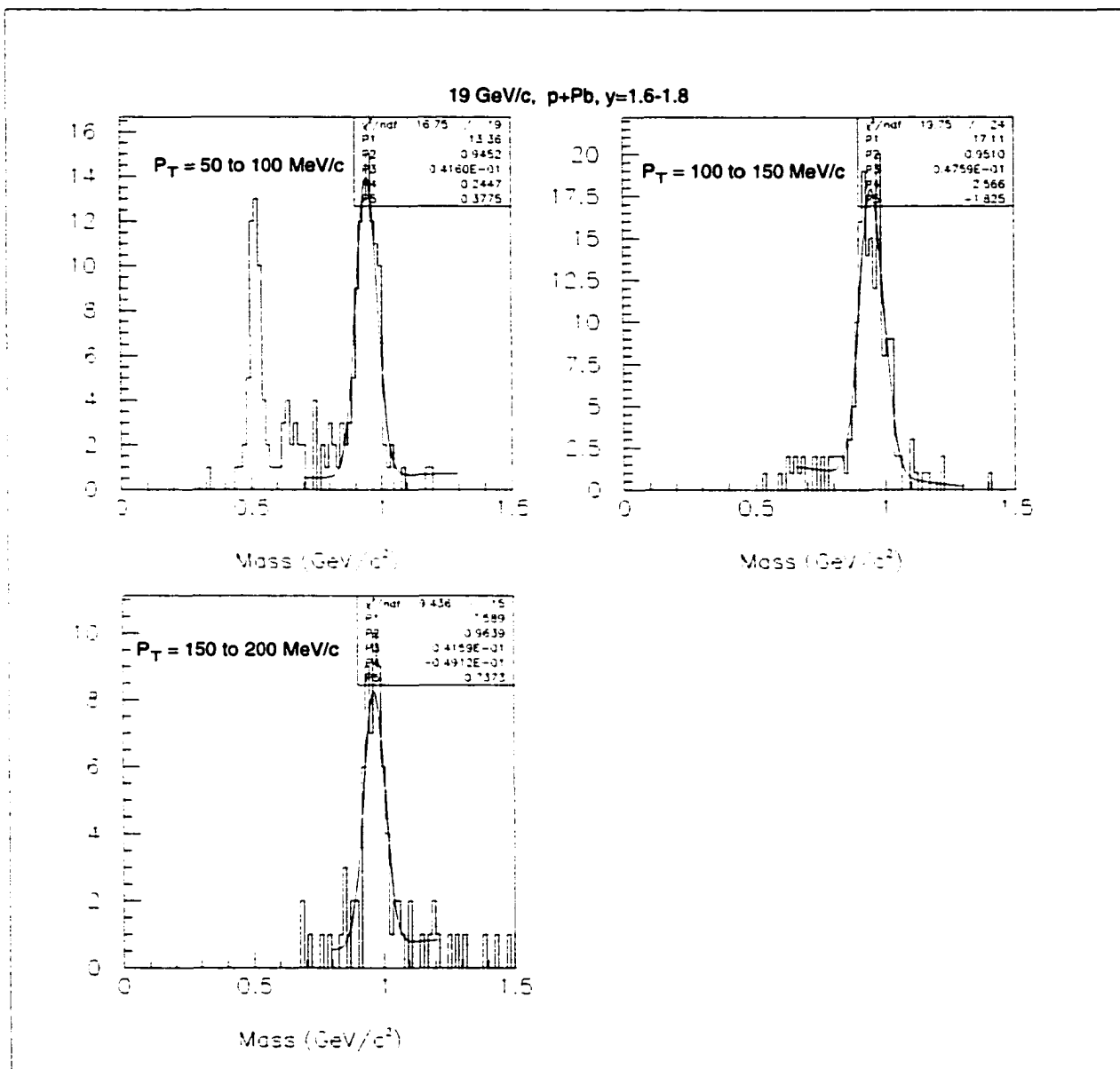


Figure 4.5 Mass histograms and fits for \bar{p} 's with rapidities from 1.6-1.8. The plot on the top is for $p_T = 50$ -100 MeV/c. The middle plot is for $p_T = 100$ -150 MeV/c, and the bottom plot is for $p_T = 150$ -200 MeV/c. These fits are for the 19 GeV/c, -0.2 T data with the Pb target.

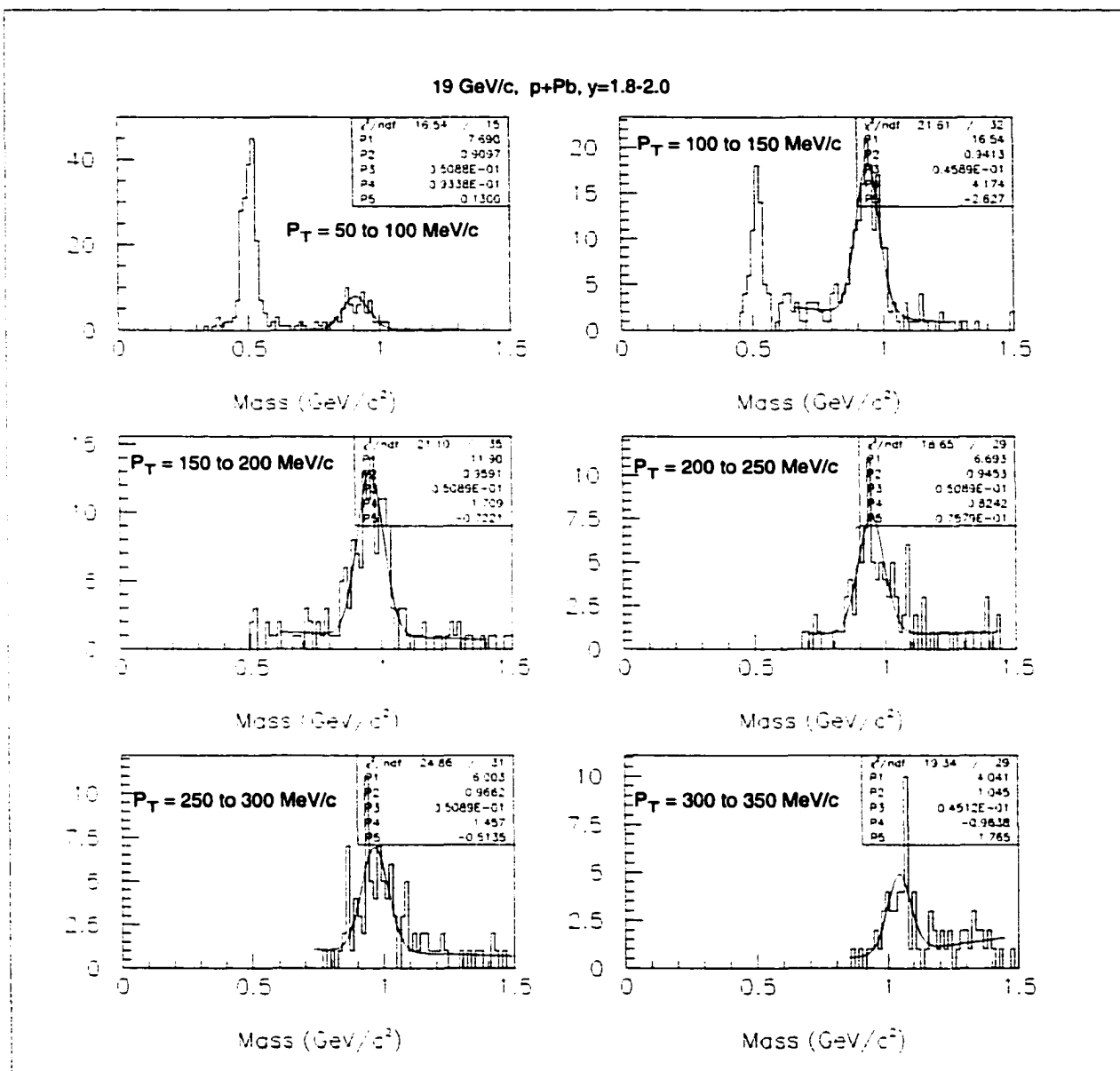


Figure 4.6 Mass histograms and fits for \bar{p} 's with rapidities from 1.8-2.0 and transverse momenta of 50-100 MeV/c through 300-350 MeV/c in 50 MeV/c increments. These fits are for the 19 GeV/c, -0.2 T data with the Pb target.

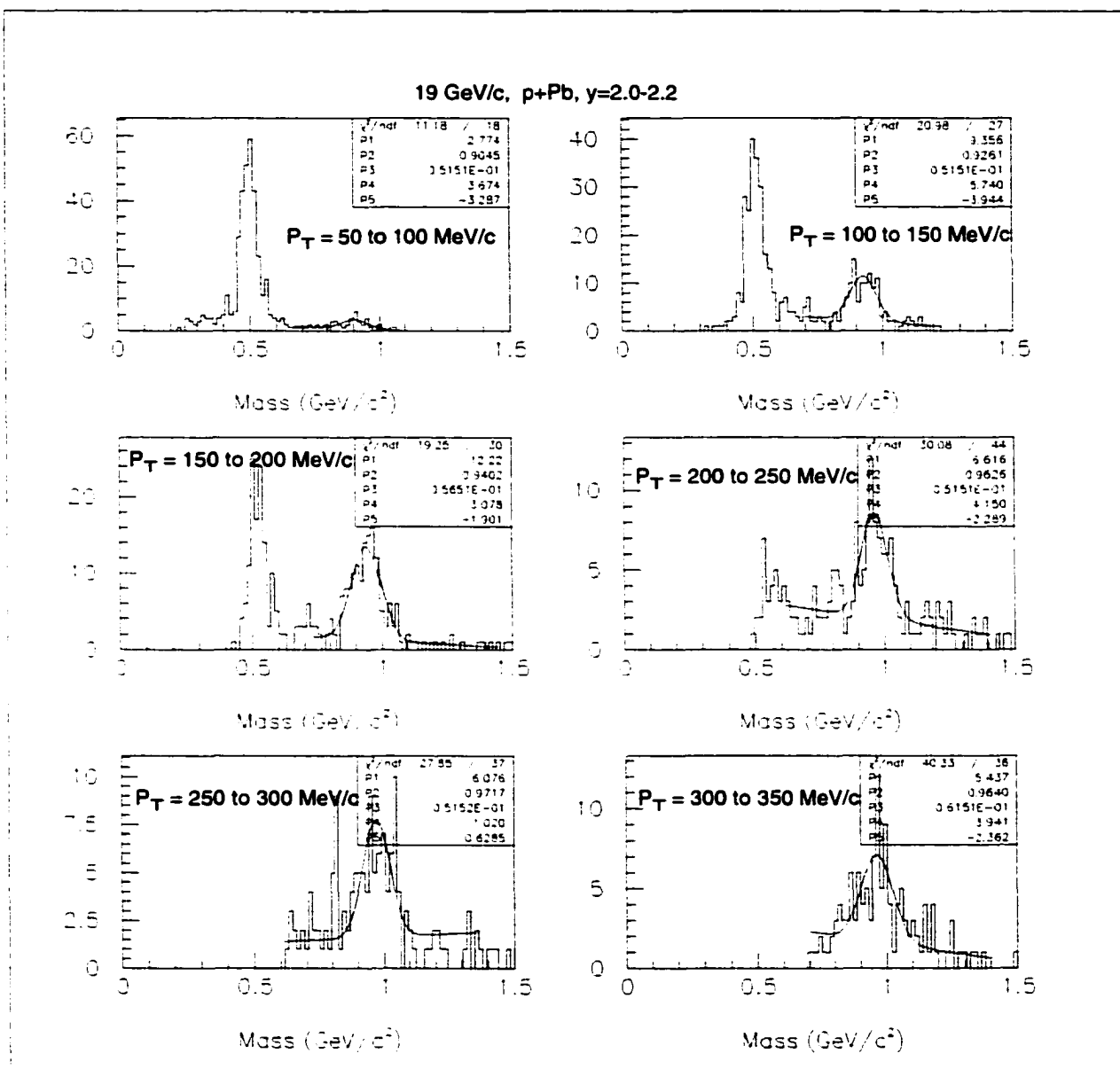


Figure 4.7 Mass histograms and fits for \bar{p} 's with rapidities from 2.0-2.2 and transverse momenta of 50-100 MeV/c through 300-350 MeV/c in 50 MeV/c increments. These fits are for the 19 GeV/c, -0.2 T data with the Pb target.

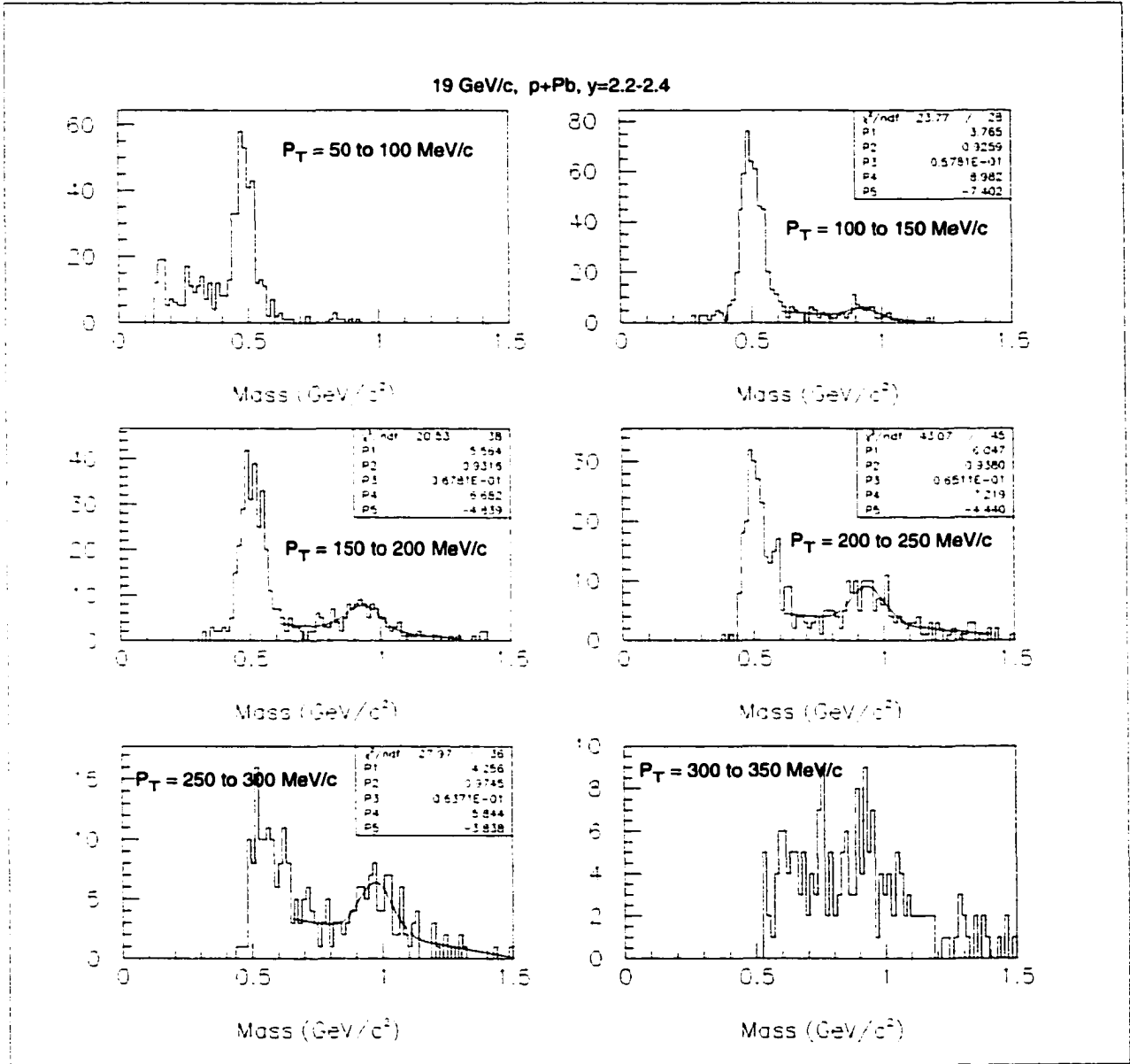


Figure 4.8 Mass histograms and fits for \bar{p} 's with rapidities from 2.2-2.4 and transverse momenta of 50-100 MeV/c through 300-350 MeV/c in 50 MeV/c increments. These fits are for the 19 GeV/c, -0.2 T data with the Pb target.

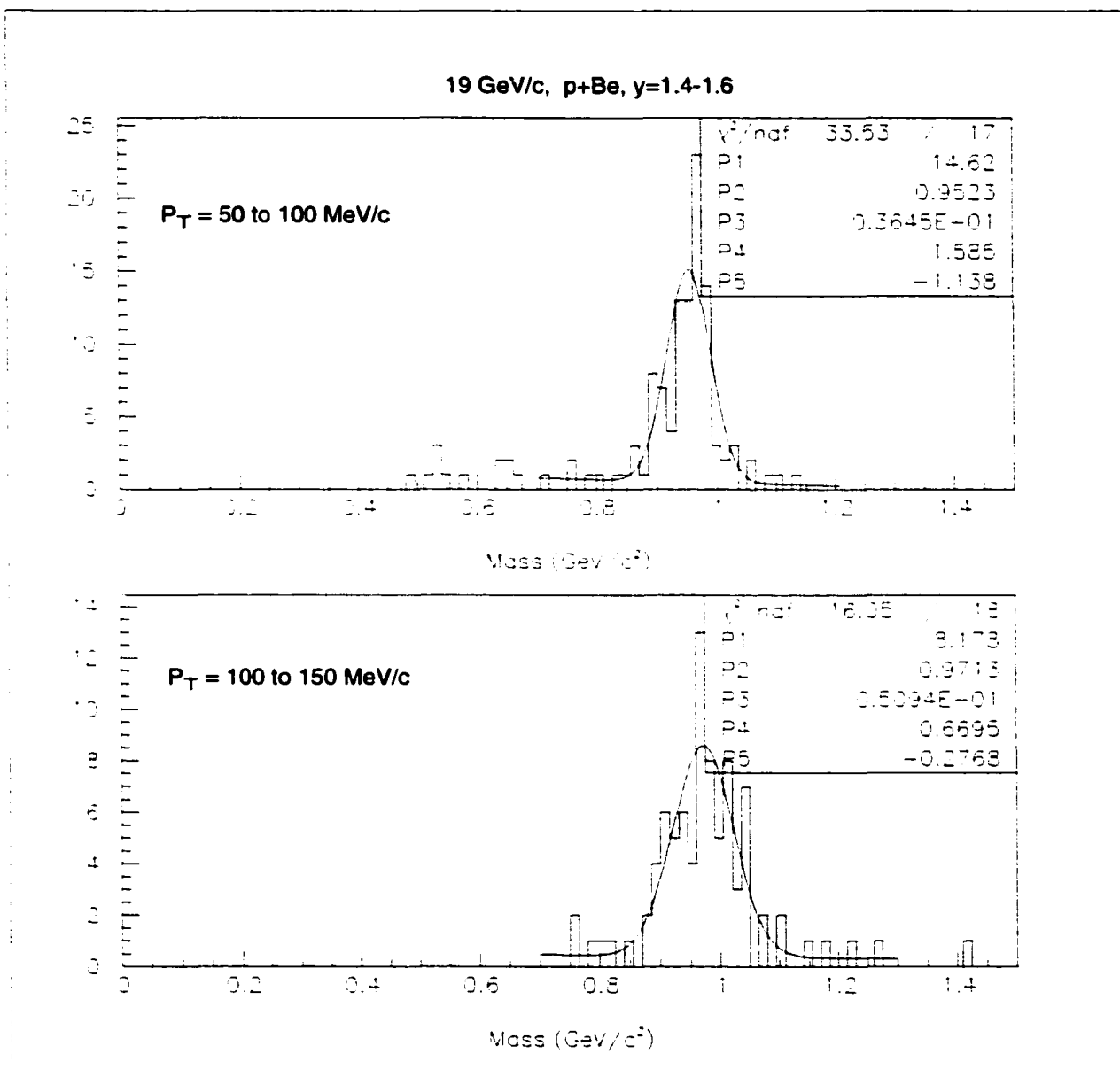


Figure 4.9 Mass histograms and fits for \bar{p} 's with rapidities from 1.4-1.6 and transverse momenta of 50-100 MeV/c and 100-150 MeV/c. These fits are for the 19 GeV/c, -0.2 T data with the Be target.

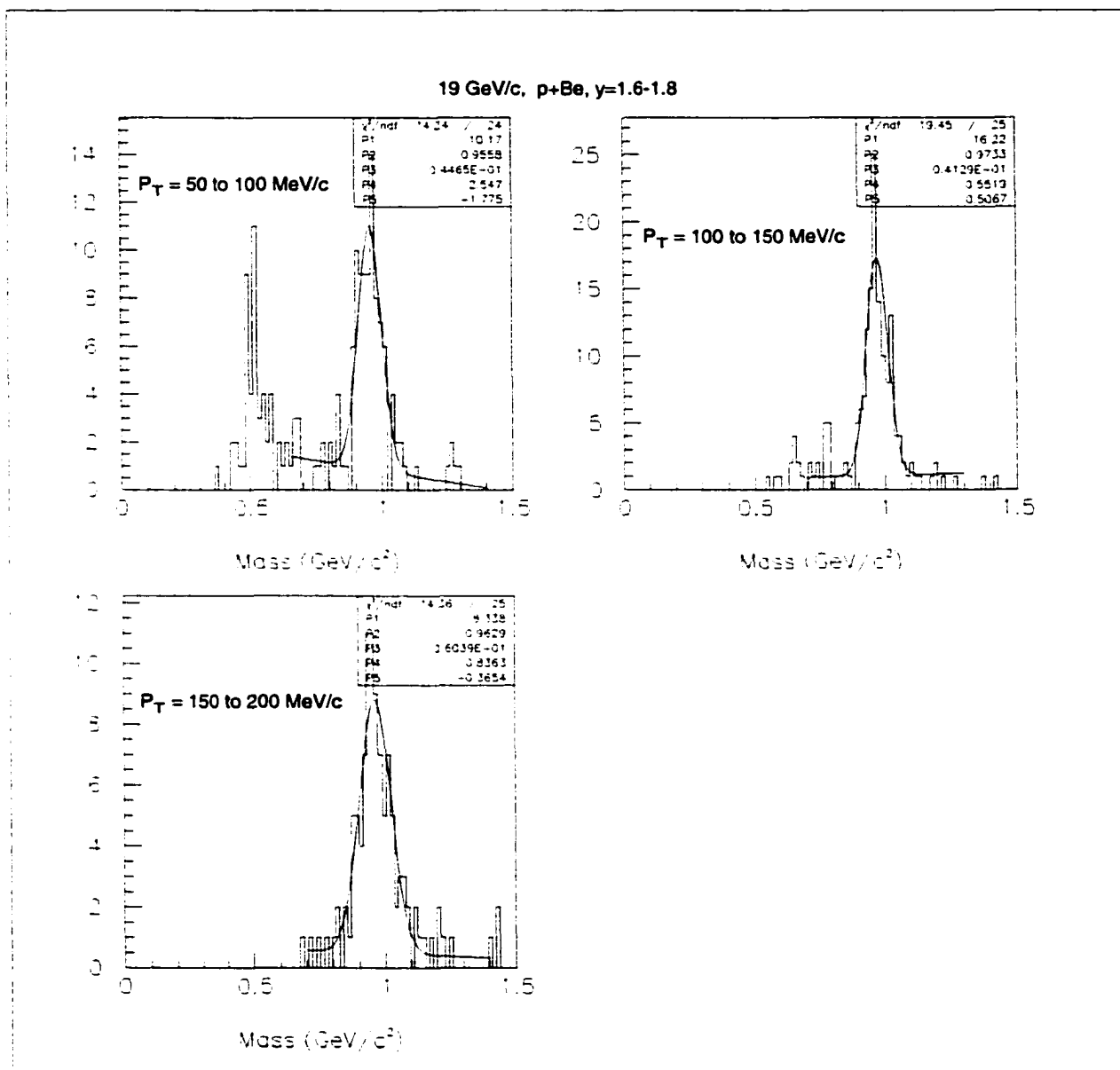


Figure 4.10 Mass histograms and fits for \bar{p} 's with rapidities from 1.6-1.8 and transverse momenta of 50-100 MeV/c, 100-150 MeV/c, and 150-200 MeV/c. These fits are for the 19 GeV/c, -0.2 T data with the Be target.

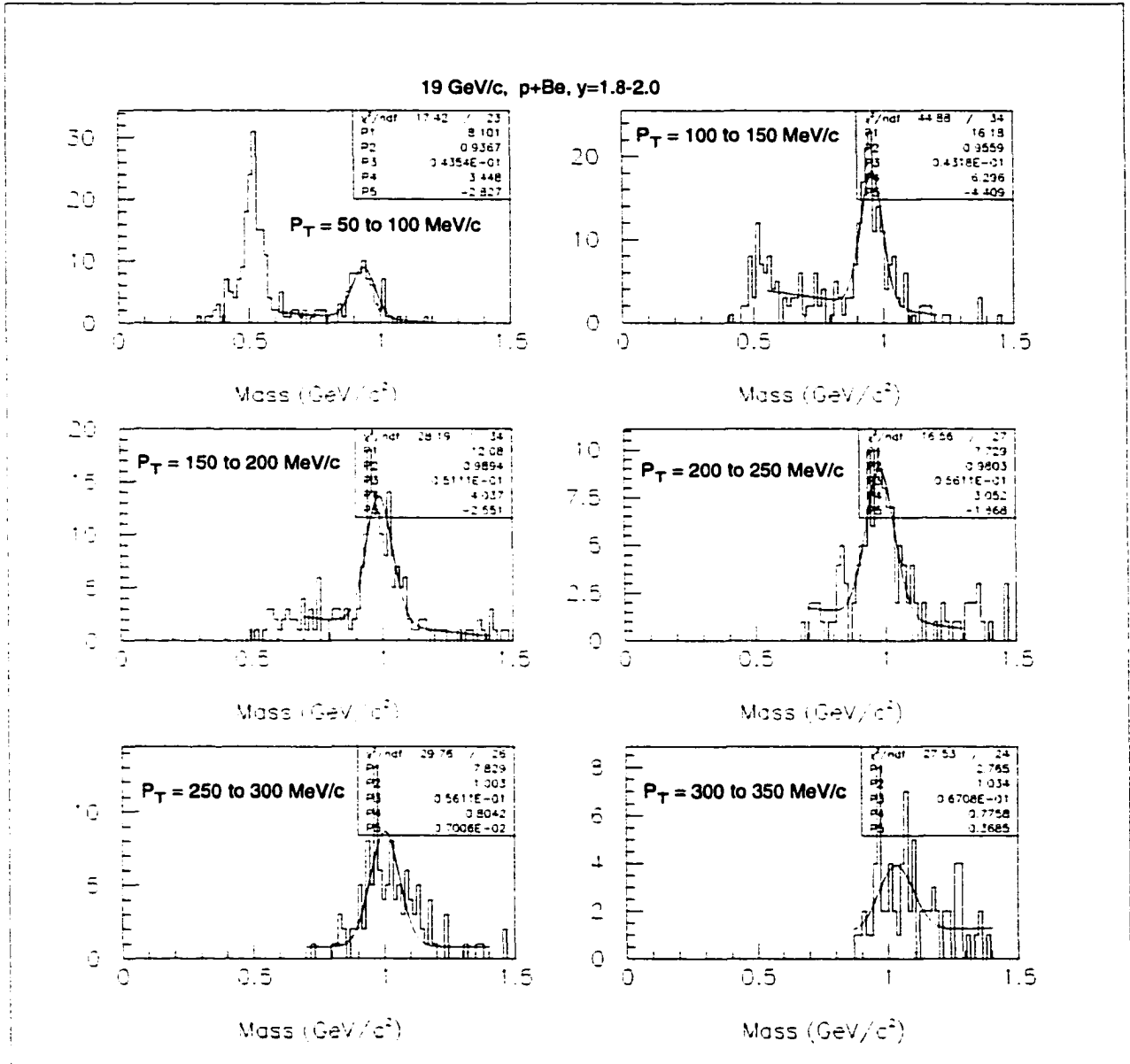


Figure 4.11 Mass histograms and fits for \bar{p} 's with rapidities from 1.8-2.0 and transverse momenta of 50-100 MeV/c through 300-350 MeV/c in 50 MeV/c increments. These fits are for the 19 GeV/c, -0.2 T data with the Be target.

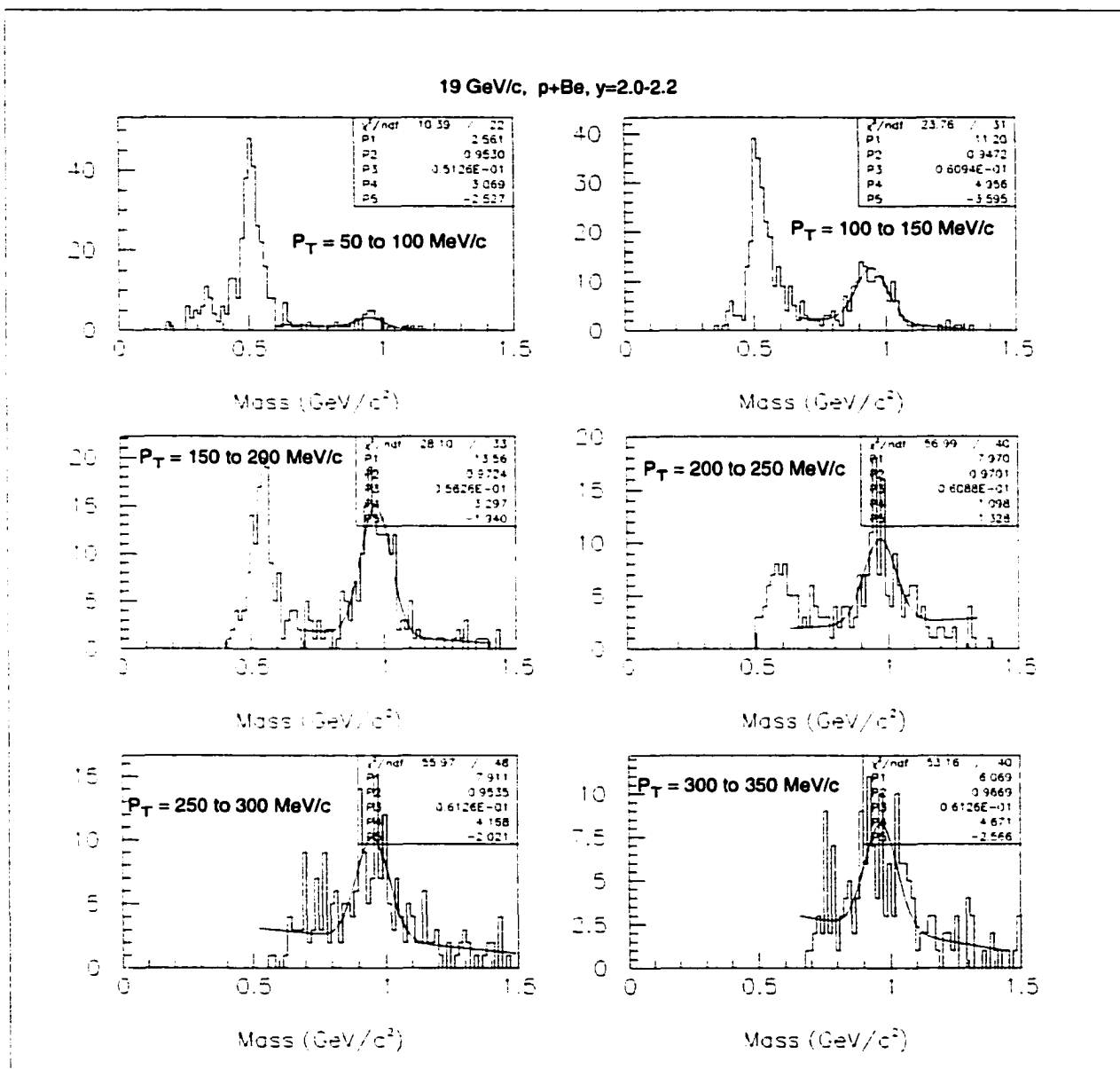


Figure 4.12 Mass histograms and fits for \bar{p} 's with rapidities from 2.0-2.2 and transverse momenta of 50-100 MeV/c through 300-350 MeV/c in 50 MeV/c increments. These fits are for the 19 GeV/c, -0.2 T data with the Be target.

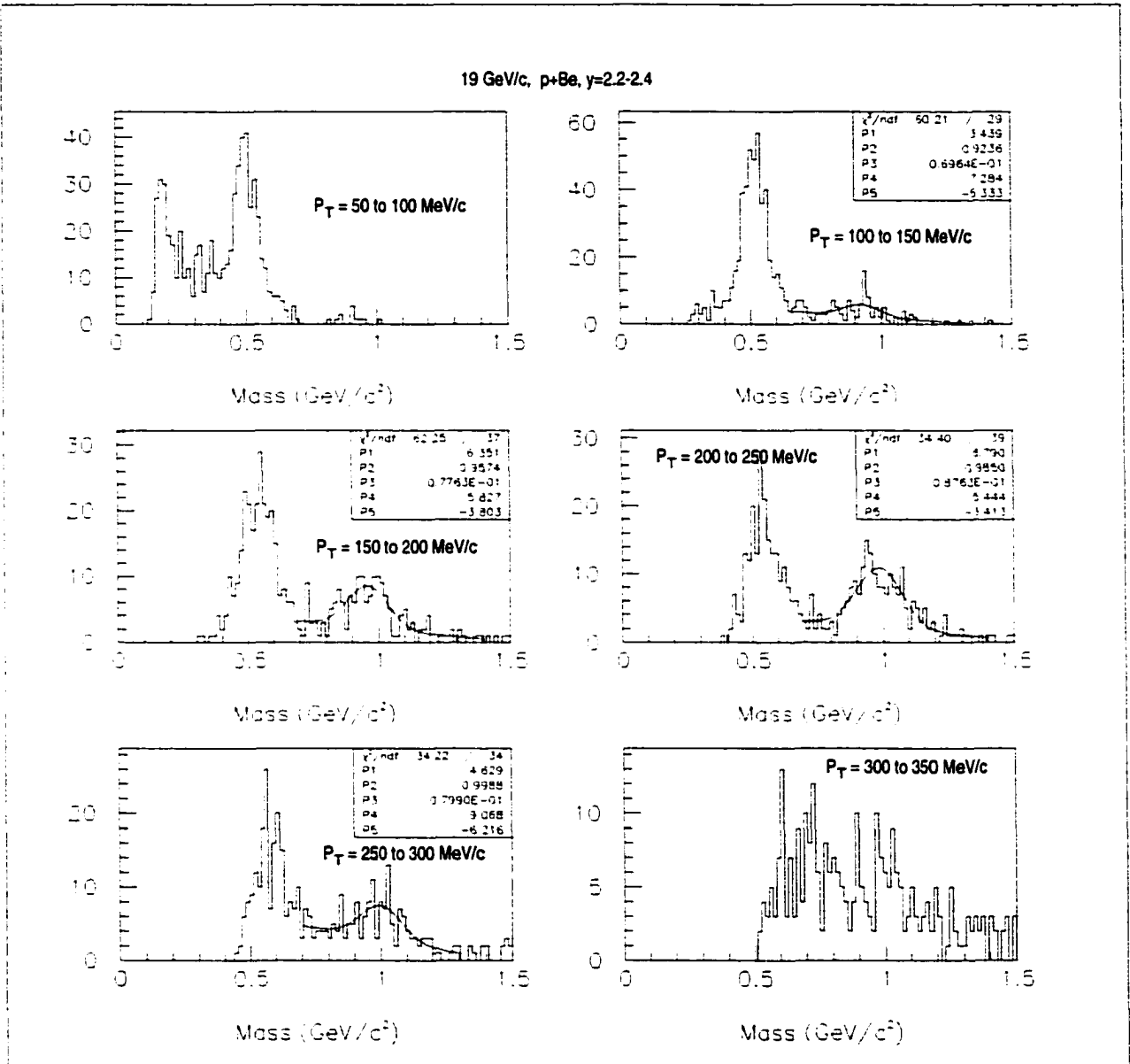


Figure 4.13 Mass histograms and fits for \bar{p} 's with rapidities from 2.2-2.4 and transverse momenta of 50-100 MeV/c through 300-350 MeV/c in 50 MeV/c increments. These fits are for the 19 GeV/c, -0.2 T data with the Be target.

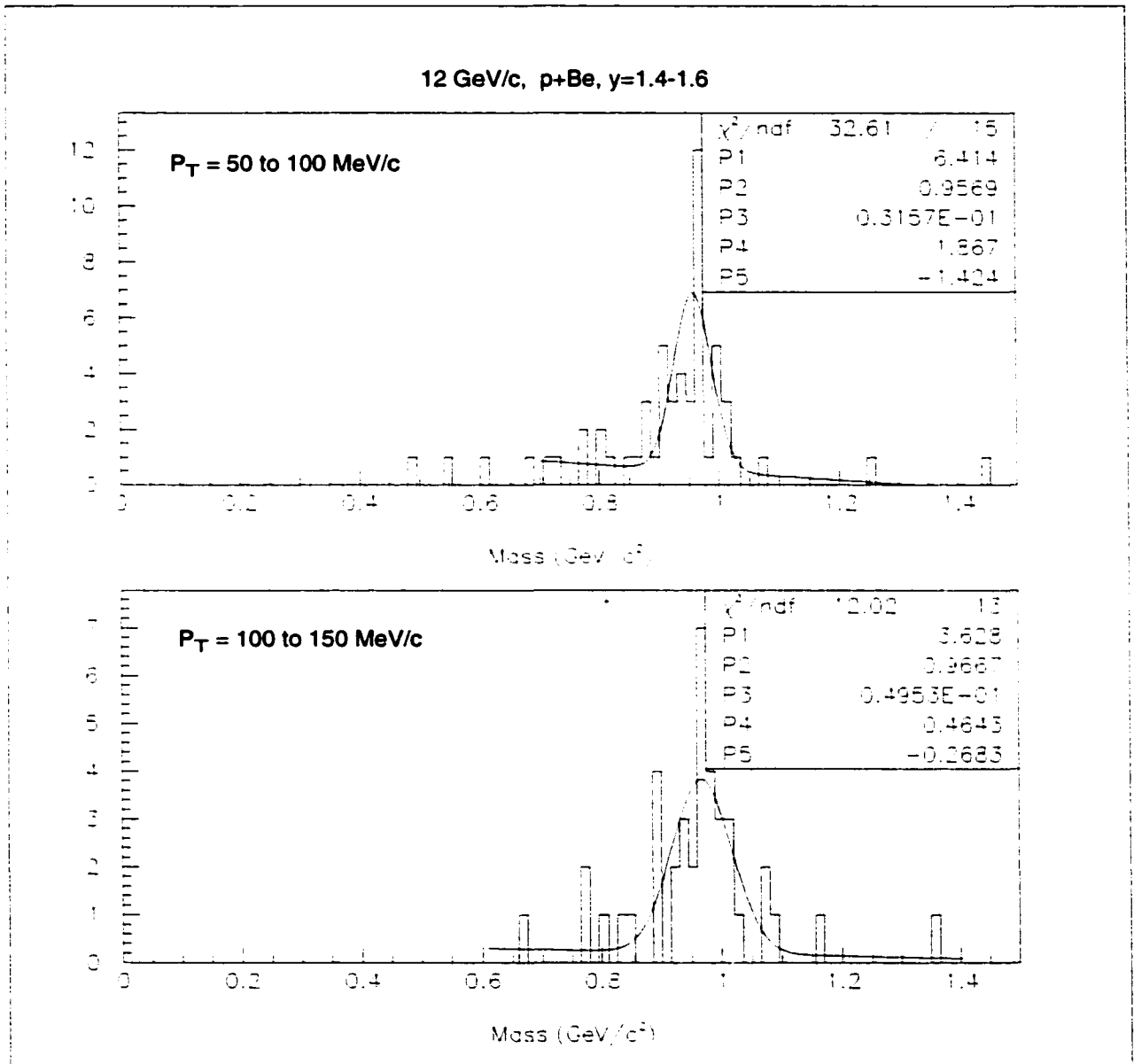


Figure 4.14 Mass histograms and fits for \bar{p} 's with rapidities from 1.4-1.6 and transverse momenta of 50-100 MeV/c and 100-150 MeV/c. These fits are for the 12 GeV/c, -0.2 T data with the Be target.

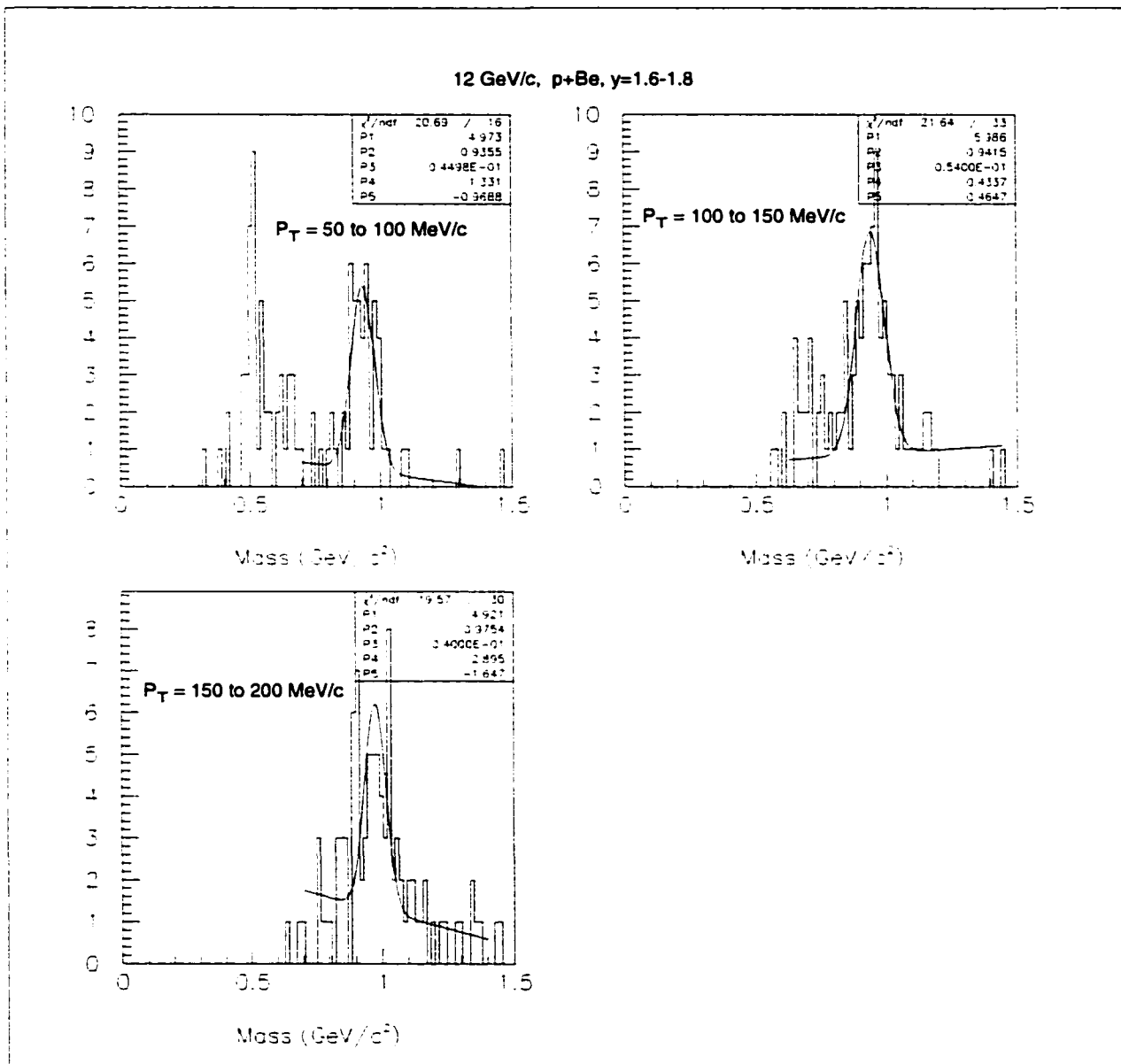


Figure 4.15 Mass histograms and fits for \bar{p} 's with rapidities from 1.6-1.8 and transverse momenta of 50-100 MeV/c, 100-150 MeV/c, and 150-200 MeV/c. These fits are for the 12 GeV/c, -0.2 T data with the Be target.

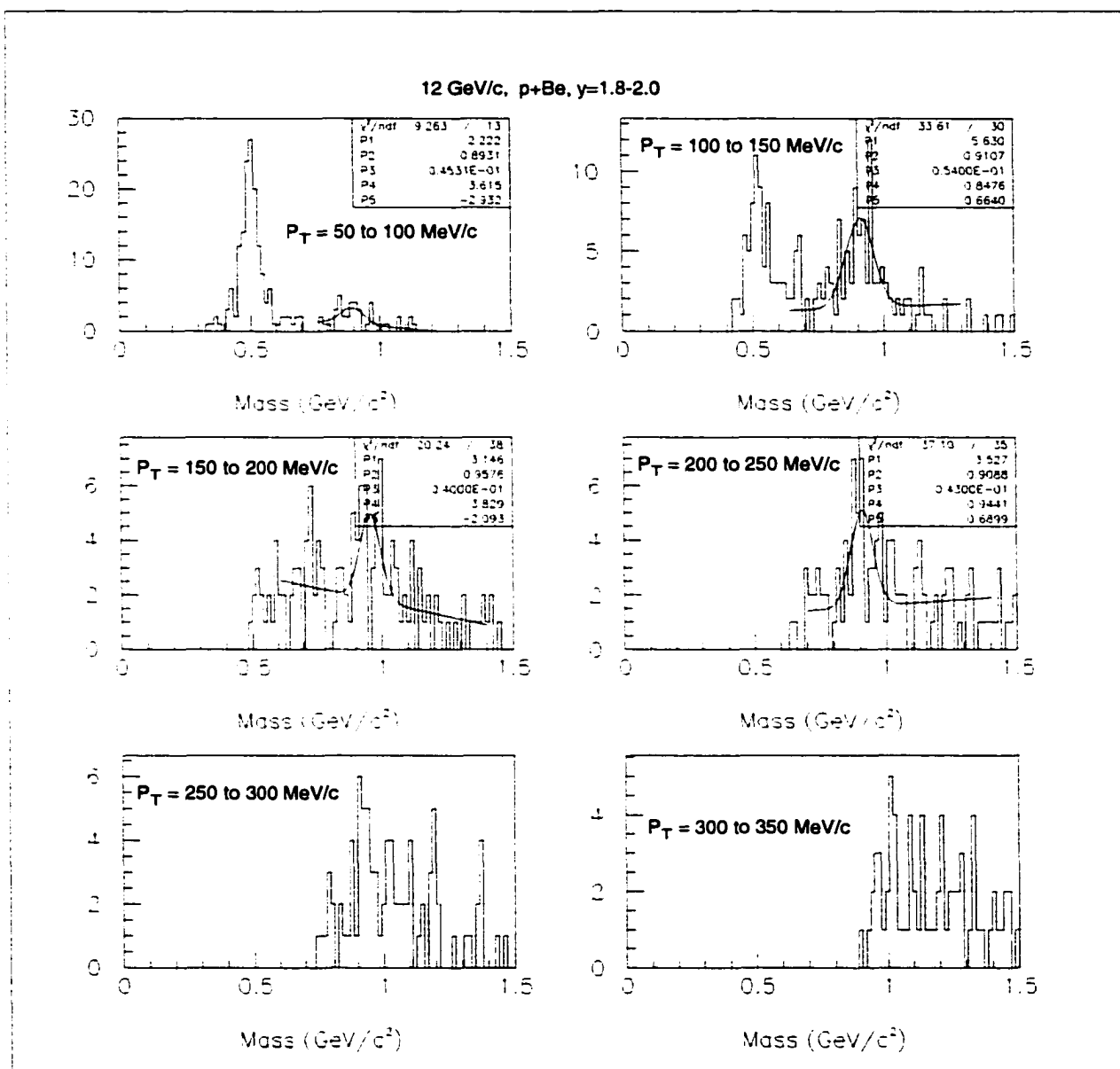


Figure 4.16 Mass histograms and fits for \bar{p} 's with rapidities from 1.8-2.0 and transverse momenta of 50-100 MeV/c through 150-200 MeV/c in 50 MeV/c increments. These fits are for the 12 GeV/c, -0.2 T data with the Be target.

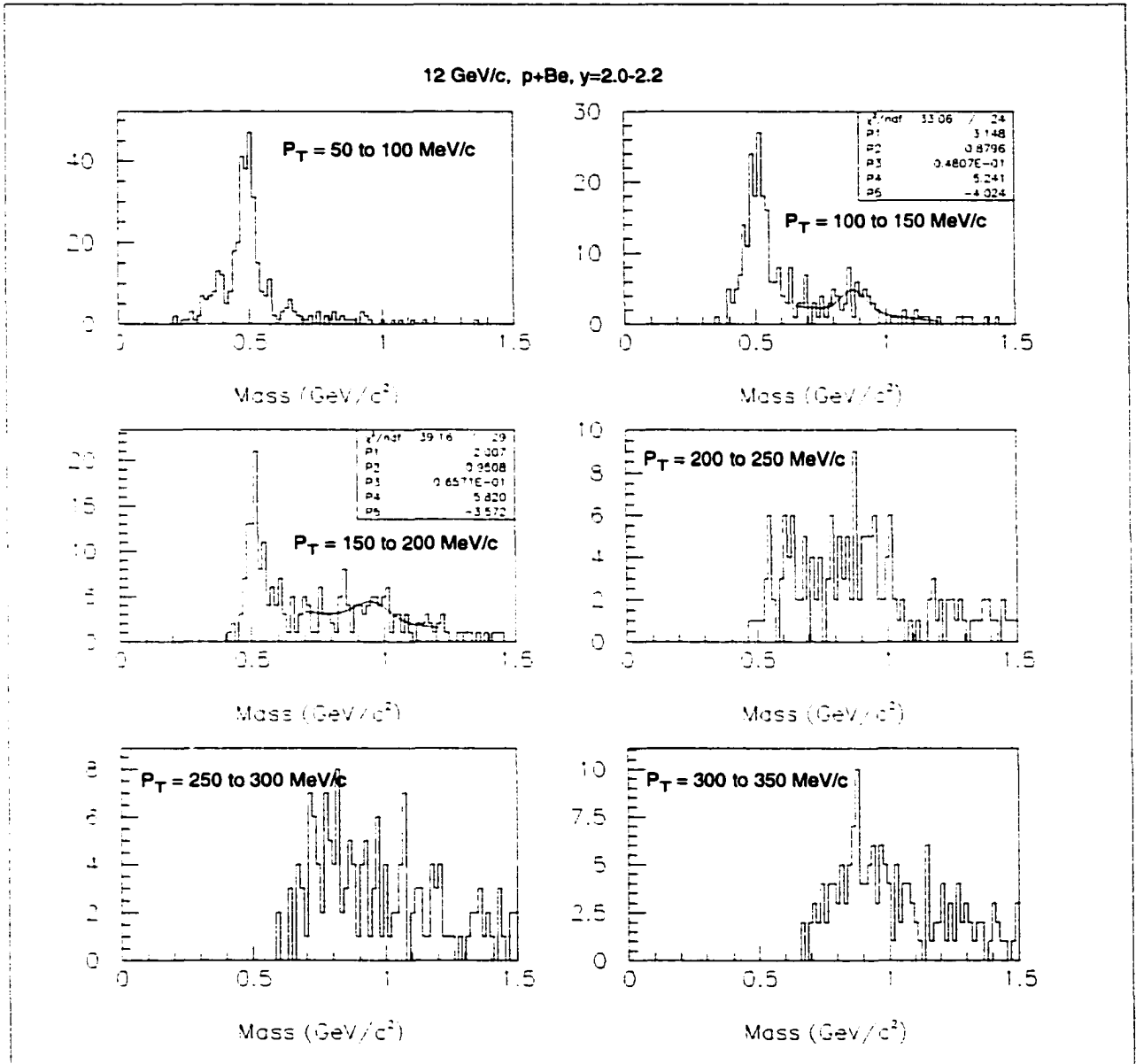


Figure 4.17 Mass histograms and fits for \bar{p} 's with rapidities from 2.0-2.2 and transverse momenta of 100-150 MeV/c and 150-200 MeV/c in 50 MeV/c increments. These fits are for the 12 GeV/c, -0.2 T data with the Be target.

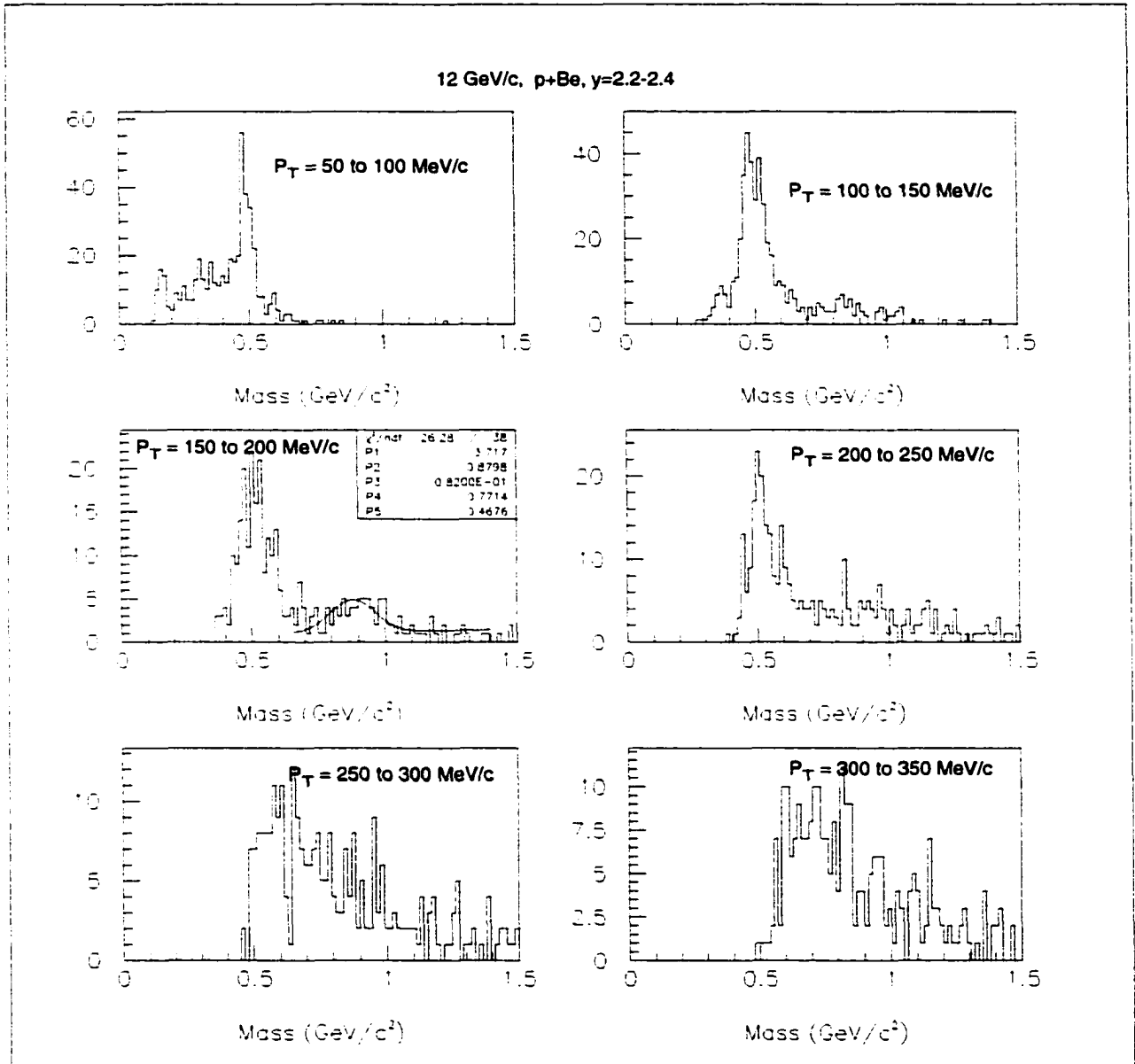


Figure 4.18 Mass histograms and fits for \bar{p} 's with rapidities from 2.2-2.4 and transverse momenta of 150-200 MeV/c. These fits are for the 12 GeV/c, -0.2 T data with the Be target.

Mass Peak Shifts

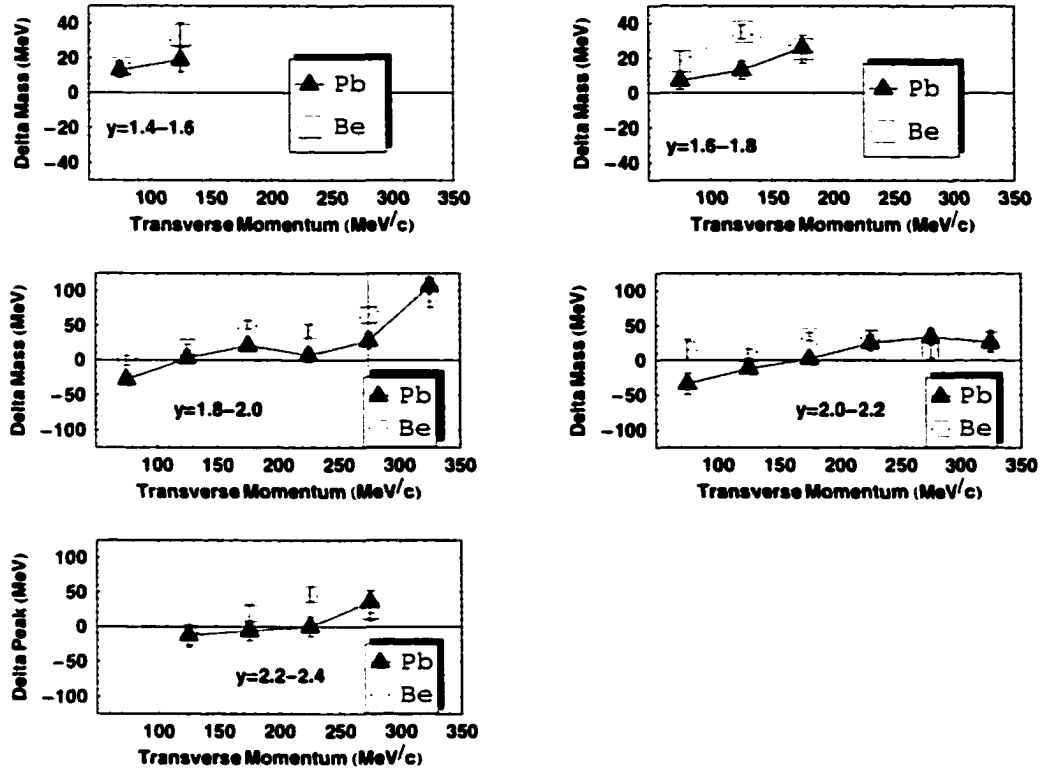


Figure 4.19 Position of the mass peaks in the various histograms.

transverse momenta. Since the transverse momentum acceptance opened up at high rapidity, the effect diminished because the p_T bins did not correspond to particles on the edge of our kinematic acceptance.

Since the Monte Carlo simulations don't precisely reproduce the mass shifts at high p_T , most of the assertions that will be made in this thesis will use the measurements that sample data taken in the middle of our p_T acceptance. The data at $p_T = 125$ MeV/c will be used the most extensively. Fig. 4.19 shows that the shift in the position of the mass peaks was small at that p_T .

Since the target dependence in the data is of crucial importance to the results, we tried to make sure that the measurements were not corrupted by artificially biased target dependent constraints on the widths of the mass peaks. The widths were arrived at in the following

manner: For each target, the p_T bin with the highest statistics for each given rapidity was chosen. The widths of the peaks in the low statistics bins were constrained to be as close as possible to the width of the highest statistics bin. In order to estimate a systematic error associated with this process, the mass peaks were also fit with widths that were first 2 to 3 σ times narrower and then 2 to 3 σ wider than the constrained width. σ was the error associated with the width of the fit to the highest statistics p_T bin at that rapidity. The error associated with it was used because it was the bin that constrained the fits at that rapidity. The difference in the number of counts using the narrower width vs. the constrained width usually became the negative estimate of the systematic error in the fitting process, and the difference in the number of counts using the greater width vs. the constrained width usually became the positive estimate of the systematic error of the fitting process. Fig. 4.20 shows that the Be data sometimes exhibited larger widths than the Pb data. They do not differ very much however, and were successfully constrained to be roughly constant for each p_T range at a given rapidity.

4.4 Corrections

There were several effects that, without correction, would have lead to inaccurate results. One of the major effects in the p-A running was the presence of “delta rays” from collisions of the projectile with electrons in the target. Delta rays are relativistic electrons that are produced in the collision of projectiles with atomic electrons. Even if a nuclear reaction has not occurred, delta rays often set off the detector’s minimum bias trigger which is used to indicate a nuclear inelastic collision. A correction was made for false triggers in which a delta ray caused a minimum bias trigger but no inelastic collision occurred. While these delta rays were responsible for sizable numbers of minimum bias triggers, they were not expected to have caused a “level 2” trigger, because this trigger was linked to our downstream calorimeter, which was unlikely to be occupied in these delta ray events. Another sort of contamination comes from interaction of beam particles with objects other than the target. We conducted several target-out runs to enable us to quantify this effect.

Widths of Mass Peaks

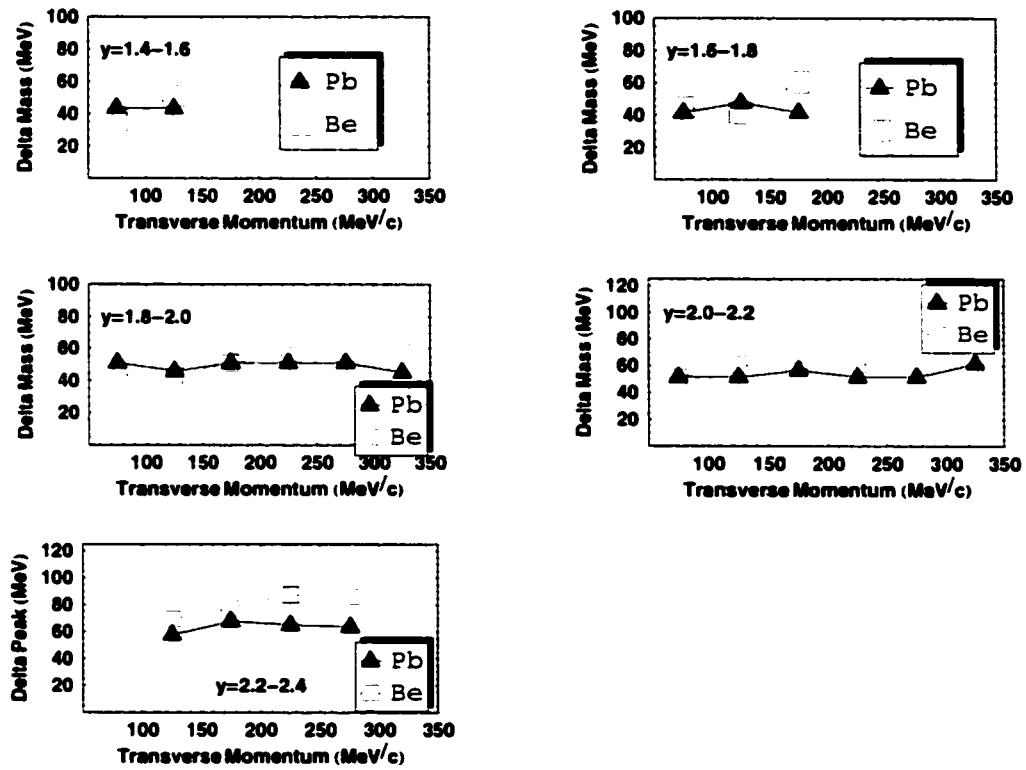


Figure 4.20 Widths used to create fits.

In all (aside from the standard corrections described in the previous section) there were two classes of corrections that were applied to the data. The first were corrections to the estimated total number of events sampled, which ultimately affected the overall scaling of the invariant multiplicities. The second were corrections to the invariant multiplicities on a bin by bin basis. For example, if we were calculating the invariant multiplicity as a function of p_T at fixed rapidity, we might make a separate correction for each p_T bin. Empty target corrections, that is, corrections for events created not in the target, but by collisions with the experimental apparatus itself have components that fit into both of the above classes. To start, we determine a formula to calculate the total number of events sampled.

4.4.1 Events sampled

Let “ n ” denote the total number of counts of a particle for a particular y and p_T bin. Then, we might decide that the total number of counts observed is described by eqn. 4.4

$$n = n_t + n_{em} + n_\delta \quad (4.4)$$

where n_t are those counts caused by interactions of the projectile with the target, n_{em} are the counts caused by empty target contributions and n_δ are the counts from delta ray class events. Likewise, one might describe the total number of minimum bias events by eqn. 4.5

$$N = N_t + N_{em} + N_\delta \quad (4.5)$$

Here, capital “ N ”s denote contributions to minimum bias triggers. N_t are the minimum bias triggers caused by projectile interactions with the target, N_{em} represent the contributions from target out events, and N_δ denote minimum bias triggers caused by delta rays. To reiterate, the capital “ N ”s represent minimum bias events over all phase space, while the small “ n ”s represent the number of counts of a particular particle in a particular region of phase space. Now, while what we measure directly is $\frac{n}{N}$, what we must attempt to determine is $\frac{n_t}{N_t}$. We can write this as eqn. 4.6

$$\frac{n_t}{N_t} = \frac{\frac{n_t}{N}}{\frac{N_t}{N}} \quad (4.6)$$

Let us evaluate the numerator and denominator separately. Using eqn. 4.4 on the numerator, we get

$$\frac{n_t}{N} = \frac{n}{N} - \frac{n_{em}}{N} - \frac{n_\delta}{N} = \frac{n}{N} \left(1 - \frac{n_{em}}{n} - \frac{n_\delta}{n}\right) \quad (4.7)$$

For the denominator, using eqn. 4.5, we get

$$\frac{N_t}{N} = \left(1 - \frac{N_{em}}{N} - \frac{N_\delta}{N}\right) \quad (4.8)$$

Plugging eqns. 4.7 and 4.8 into eqn. 4.6, we get eqn. 4.9.

$$\frac{n_t}{N_t} = \frac{\frac{n}{N} \left(1 - \frac{n_{em}}{n} - \frac{n_\delta}{n}\right)}{1 - \frac{N_{em}}{N} - \frac{N_\delta}{N}} \quad (4.9)$$

We should isolate each of these ratios and determine how each is determined: $\frac{n_{em}}{n}$, $\frac{n_\delta}{n}$, $\frac{N_{em}}{N}$, and $\frac{N_\delta}{N}$. To dispense with one of these, $\frac{n_\delta}{n}$, was found to be small because very few \bar{p} events corresponded to events when hits were discovered in the end counters. The effect was smaller than 1 percent.

4.4.2 Delta ray corrections: $\frac{N_\delta}{N}$

In order to estimate the fraction of events that were delta ray events for any one target and beam momentum, we analyzed pre-scaled minimum bias or gint0 (or INT0) triggers. This sample was qualitatively indistinguishable from the gletint2 sample. Examining 10,000 of these events, we estimated the delta ray correction by seeing how many of these events resulted in a hit in our end-counter for uninteracted beam (MAC). If a hit was recorded in MAC for a minimum bias event, then one might assume that the minimum bias trigger was caused by a delta ray. Of course, some other secondary particle, other than the uninteracted beam particle may have triggered the detector and, there are times when beam particles miss the end counter altogether. Both these eventualities were, to some extent, quantified, and both turned out to be small.

To estimate the number of times that some other secondary particle hit the MAC counter, we counted the number of times that the beam particle clearly interacted but the MULT detector went off anyway by looking at the coincidence of LET events and MAC hits. In LET triggers (as opposed to min bias triggers) we are fairly confident that an inelastic event has occurred, so the MAC counter should never have gotten hit. The number of coincidences between MAC hits and LET triggers turned out to be small. For pBe data at 12 GeV/c, the fraction of times that an LET trigger coincided with a delta ray event was 0.4%.

4.4.3 Empty target correction.

To estimate the fraction of events in which \bar{p} 's were created (and subsequently tracked) away from the target, several target out runs in the 19 GeV/c -0.2 T data were analyzed. Although a very small peak could be discerned in the combined data set, when split up into y and p_T bins, the count rate was often below the noise level in the mass plots. In this event, an upper limit on the number of \bar{p} 's was estimated, and this rate was subtracted from the counts for the various targets. In most cases, the rate was about 5 % or less. For the 12 GeV/c data, the count rate in the target in runs was so low, it was impossible to separate out an empty target contribution, so the correction was not made for the lower momentum data.

4.4.4 Acceptance and efficiency corrections.

There were two other major corrections that need to be considered. The first was a correction for the fraction of \bar{p} trajectories that would, in the absence of background, leave tracks in the detectors. The second correction was for the fraction of particle trajectories that reconstructed into tracks in the presence of backgrounds. The first correction is termed an acceptance correction while the second is called the efficiency of the detector. Of course, the magnitude of these corrections was dependent on the kinematic properties of the \bar{p} 's (the acceptance correction being particularly sensitive to the kinematic range, since particles with certain kinematic properties will never even traverse the physical space of the detectors). In order to perform these corrections, the following steps were taken:

1. A Monte Carlo simulation of \bar{p} 's created in our target was performed using Geant. The trajectories of the \bar{p} 's was modeled in the presence of the E941 detectors and accompanying apparatus. Among other things, scattering of the \bar{p} 's was allowed. The trajectories of the particles were stored in a file.
2. "Data faking" code was applied to the particle trajectories, simulating the detector response to those \bar{p} 's that strike detectors, and fake single \bar{p} events were written to 8mm tape.
3. Tracking was performed on the 8mm tapes, and tracks were reconstructed. The main reason a Monte Carlo trajectory might fail to reconstruct to a track was simply because it doesn't traverse the physical region of all the necessary detectors, but trajectories that hit the hodoscopes between the slats, or that scattered too wildly off of material in the experimental hall also failed to reconstruct tracks. Therefore, the "acceptance" calculation accounted not only for the fiducial acceptance of the detector, but also for these other effects as well. It did not, however, account for the possible confusion caused by multiple tracks, and other evident backgrounds. Some of these effects, as well as the efficiency of the LET trigger were accounted for by the efficiency calculation.
4. The acceptance is the fraction of trajectories that actually reconstructed to tracks in the absence of any background. An acceptance number was generated for each y and p_T bin in phase space. Consistent with the rest of the analysis in this thesis, the rapidity bins were of size 0.2 and the p_T bins were of size 0.050 GeV/c. The acceptance was strongly dependent on the magnetic field settings of the dipole analyzing magnets, and very weakly dependent on the beam momentum. The weak dependence on beam momentum was due to the fact that while the beam momentum affected the absolute phase space distribution of \bar{p} 's, the acceptance correction is a fractional quantity. One can get the input distribution of \bar{p} 's wrong as long as the statistics for each y and p_T bin are high enough. In the case of the \bar{p} 's used for this calculation, they were distributed as a Gaussian in rapidity and an exponential in p_T – conventional choices.

5. Those trajectories that were successfully reconstructed to tracks were written to a file. This file was overlayed with a file of real events, and the combination was run through tracking and all the remaining cuts were enforced as in the actual analysis. The fraction of tracks that were reconstructed this second time form the efficiency number. A separate number was again generated for each y and p_T bin.

Finally, the detector efficiency was estimated using the efficiencies measured from E864's A-A runs. These efficiencies varied little from year to year in the A-A physics program.

4.5 Invariant Multiplicities.

The plots of the tables presented are given in Fig. 4.21 thru Fig. 4.24. It would be difficult to ascertain inverse slope parameters for these data because the range of p_T is so small. However, such inverse slope parameters have been measured before at similar energies, and these data can be used to fix the overall normalization of the parameterization of these data, so an overall $\frac{dn}{dy}$ can be estimated for the purpose of comparison to other data.

The \bar{p} invariant multiplicities from the collision of 12 GeV/c protons on Be are presented in Table 4.5. Similarly, the invariant multiplicites from the collision of 19 GeV/c protons on Be, Cu, and Pb are presented in Table 4.4. All the data presented comes from analysis using the -0.2 T magnetic field setting on the analyzing magnets.

Table 4.4 Invariant multiplicities for the three targets analyzed at a 19 GeV/c beam momentum: Pb, Cu, and Be. For each invariant multiplicity listed, the statistical error and lower and upper systematic errors are also listed. The invariant multiplicities and errors are multiplied by 10^4 in units of GeV^{-2} .

Rapidity	1.5	1.7	1.9	2.1	2.3
Pb					
p_T MeV/c					
75	$16.06 \pm 2.37-0.69+0.13$	$12.45 \pm 2.67-0.49+0.00$	$11.56 \pm 1.40-0.80+0.32$	$7.55 \pm 3.82-0.38+0.44$	
125	$11.79 \pm 4.56-0.42+0.32$	$15.01 \pm 2.19-0.30+0.23$	$8.99 \pm 1.58-0.35+0.24$	$6.12 \pm 1.15-0.22+0.02$	$2.88 \pm 0.61-0.15+0.10$
175		$7.99 \pm 1.95-0.21+0.29$	$11.22 \pm 1.22-0.48+0.39$	$6.11 \pm 0.81-0.25+0.21$	$3.10 \pm 0.96-0.40+0.29$
225			$7.66 \pm 1.14-0.47+0.69$	$5.11 \pm 1.30-0.20+0.19$	$2.80 \pm 0.90-0.43+0.56$
275			$7.61 \pm 1.45-0.63+1.11$	$6.68 \pm 1.18-0.45+0.64$	$2.35 \pm 0.50-0.36+0.16$
325			$11.09 \pm 4.97-0.61+0.00$	$5.73 \pm 0.96-0.38+0.73$	
Cu					
p_T MeV/c					
75	$16.03 \pm 2.81-0.44+0.36$	$15.71 \pm 3.03-0.42+0.22$	$11.18 \pm 2.35-0.16+1.26$		
125	$14.31 \pm 1.58-0.64+1.19$	$16.26 \pm 2.70-0.58+0.48$	$11.63 \pm 1.90-0.30+0.15$	$9.59 \pm 1.82-0.37+1.00$	$8.95 \pm 1.24-1.36+0.00$
175		$13.17 \pm 2.73-0.59+1.56$	$9.39 \pm 2.17-0.30+0.23$	$7.80 \pm 1.60-0.41+0.32$	$5.82 \pm 2.94-0.21+0.30$
225			$11.41 \pm 1.89-0.52+0.90$		
275					
325					
Be					
p_T MeV/c					
75	$19.98 \pm 3.43-0.54+0.34$	$17.10 \pm 4.61-0.39+0.72$	$17.50 \pm 3.69-0.66+0.22$	$11.65 \pm 3.64-0.84+0.31$	
125	$19.88 \pm 3.60-0.55+0.48$	$20.74 \pm 3.12-0.54+0.31$	$13.90 \pm 2.37-0.51+0.56$	$14.56 \pm 2.54-0.77+0.00$	$5.32 \pm 1.61-1.09+0.00$
175		$21.41 \pm 4.16-1.46+0.50$	$19.20 \pm 3.27-0.77+0.49$	$11.34 \pm 1.97-0.46+0.31$	$6.80 \pm 1.10-0.49+0.13$
225			$16.39 \pm 3.18-1.89+0.95$	$12.23 \pm 1.80-1.16+0.44$	$9.21 \pm 1.96-1.00+0.59$
275			$18.37 \pm 5.01-1.39+2.08$	$17.38 \pm 2.61-0.89+1.97$	$7.99 \pm 1.39-2.24+0.00$
325			$18.94 \pm 8.18-4.82+3.65$	$10.69 \pm 1.98-0.75+1.44$	

Table 4.5 Invariant multiplicities for the Be target at 12 GeV/c. The invariant multiplicities, statistic, and lower and upper systematic errors are quoted. All numbers are multiplied by 10^5 in units of GeV^{-2} .

Rapidity	1.5	1.7	1.9	2.1	2.3
Be					
p_T MeV/c					
75	$29.96 \pm 5.68 - 0.84 + 1.86$	$33.60 \pm 10.16 - 3.52 + 1.58$	$21.08 \pm 10.33 - 2.92 + 4.18$		
125	$42.63 \pm 14.54 - 4.42 + 3.60$	$40.68 \pm 6.41 - 4.83 + 0.43$	$23.58 \pm 4.29 - 3.21 + 0.00$	$12.23 \pm 7.48 - 1.59 + 0.56$	
175		$33.90 \pm 7.73 - 3.74 + 10.83$	$15.28 \pm 5.06 - 1.51 + 3.82$	$7.63 \pm 3.21 - 0.54 + 0.01$	$17.19 \pm 3.39 - 3.86 + 0.00$
225			$22.85 \pm 6.55 - 3.22 + 0.16$		
275					
325					

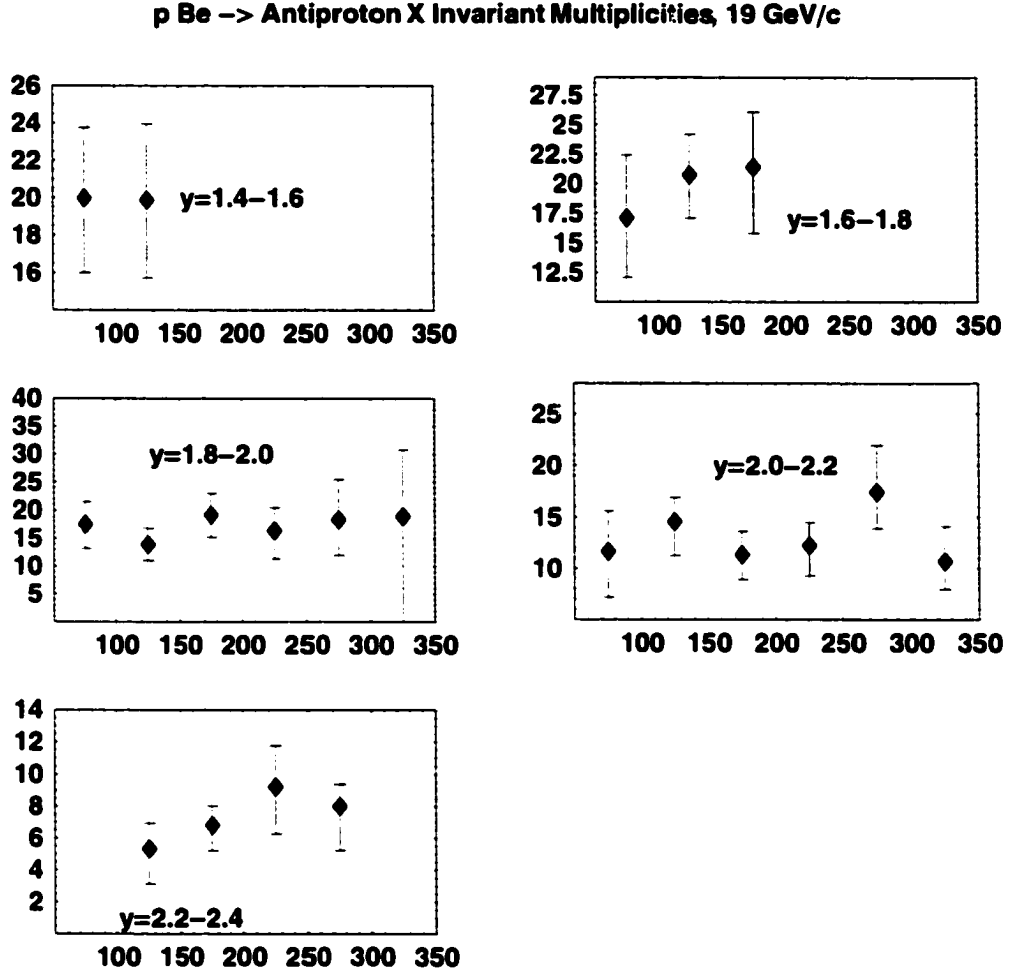


Figure 4.21 Plot of the invariant multiplicities $\frac{d^2\sigma}{\sigma_{\text{inel}}2\pi p_T dp_T dy}$ vs. p_T in MeV of \bar{p} 's from 19 GeV/c protons incident on a Be target. There are six panels. Each panel represents a different rapidity interval, starting with 1.4–1.6 and going to 2.4–2.6. The invariant multiplicities are plotted versus transverse momentum for each plot. Each invariant multiplicity is multiplied by a factor of 10^4

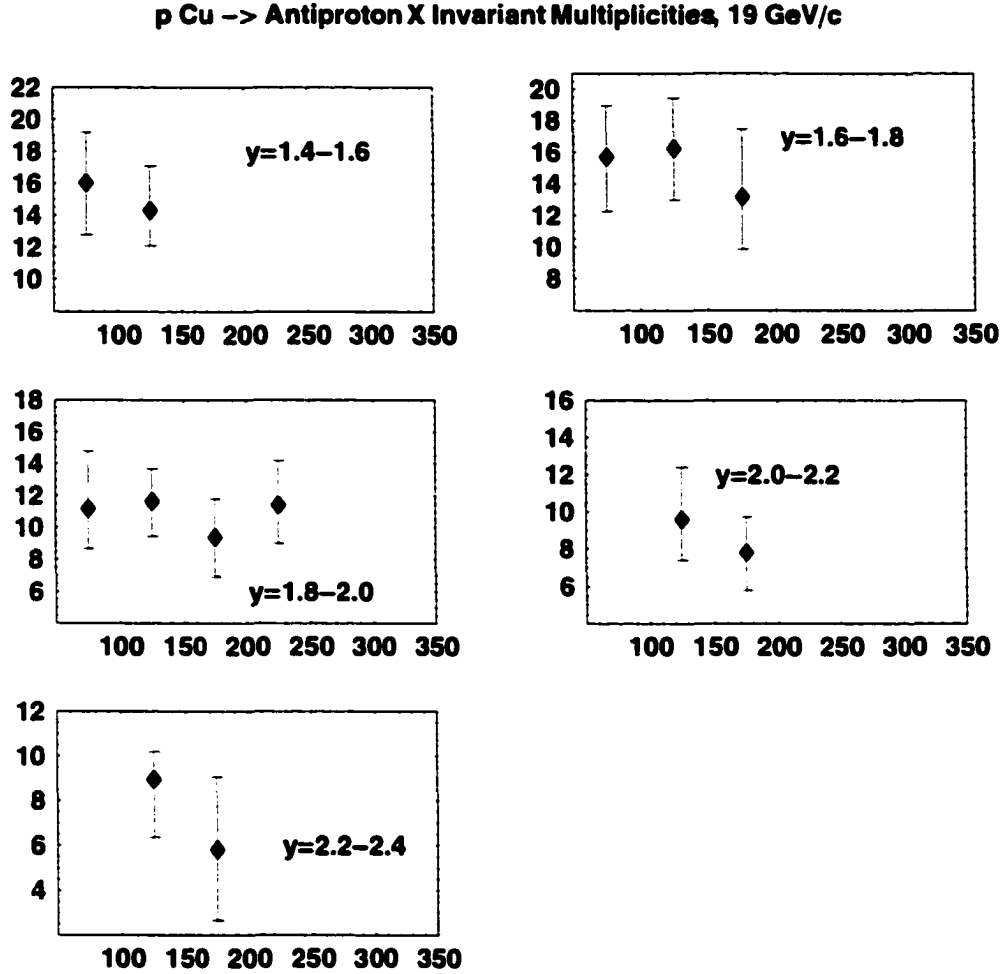


Figure 4.22 Plot of the invariant multiplicities $\frac{d^2\sigma}{\sigma_{inel} 2\pi p_T dp_T dy}$ vs. p_T in MeV of \bar{p} 's from 19 GeV/c protons incident on a Cu target. There are six panels. Each panel represents a different rapidity interval, starting with 1.4-1.6 and going to 2.4-2.6 (moving first across and then down). The invariant multiplicities are plotted versus transverse momentum for each plot. Each invariant multiplicity is multiplied by a factor of 10⁴

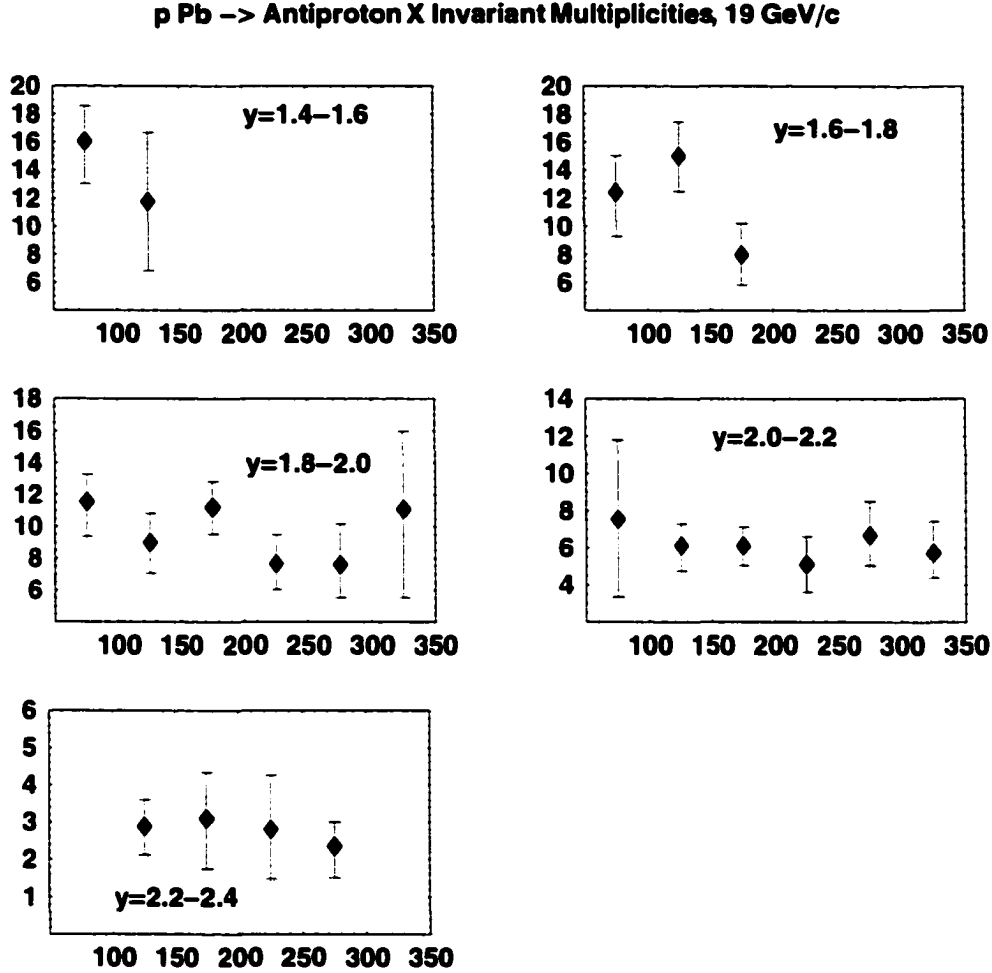


Figure 4.23 Plot of the invariant multiplicities $\frac{d^2\sigma}{\sigma_{inel}2\pi p_T dp_T dy}$ vs. p_T in MeV of \bar{p} 's from 19 GeV/c protons incident on a Pb target. There are six panels. Each panel represents a different rapidity interval, starting with 1.4–1.6 and going to 2.4–2.6 (moving first across and then down). The invariant multiplicities are plotted versus transverse momentum for each plot. Each invariant multiplicity is multiplied by a factor of 10^4

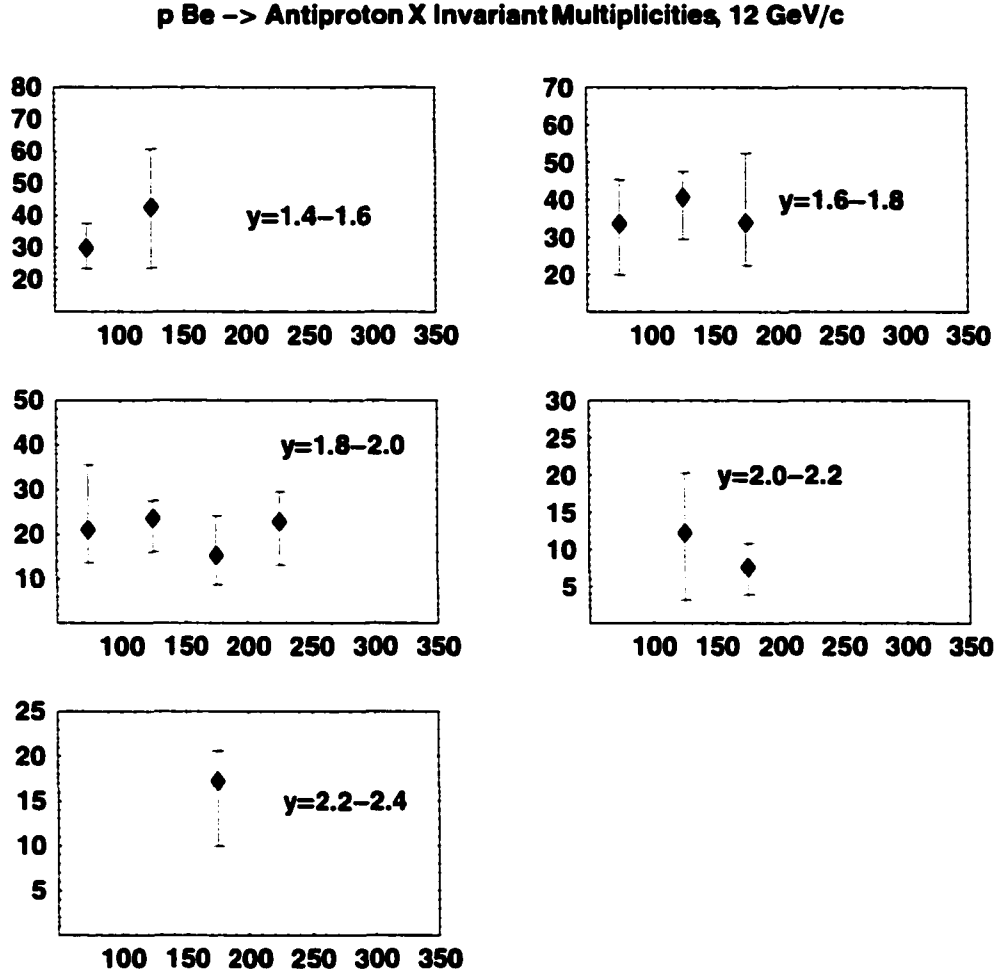


Figure 4.24 Plot of the invariant multiplicities $\frac{d^2\sigma}{\sigma_{inel}2\pi p_T dp_T dy}$ vs. p_T in MeV of \bar{p} 's from 19 GeV/c protons incident on a Be target. There are six panels. Each panel represents a different rapidity interval, starting with 1.4–1.6 and going to 2.4–2.6 (moving first across and then down). The invariant multiplicities are plotted versus transverse momentum for each plot. Each invariant multiplicity is multiplied by a factor of 10^5

CHAPTER 5. MODELING RESULTS

5.1 Quantifying Annihilation.

Using the measured target dependence for \bar{p} yields and a simple model, it was possible to estimate an effective annihilation cross section for the \bar{p} in the nuclear medium. This **effective** annihilation cross section represents the net result of many possible mechanisms, such as the formation time of the \bar{p} (which would screen the annihilation) and the effects of Fermi motion in the nucleus (which might enhance the production). Since these mechanisms were explicitly absent from the model, they contributed to the “effective” annihilation cross section. The model was as simple as dirt but served as a means to interpret these results and compare them to other experiments.

The following assumptions were made in the code that calculates the effective annihilation cross sections:

The model assumes that a p-A collision amounts to a superposition of N-N collisions. Energy loss per N-N collision is ignored, so a \bar{p} has an equal chance of being created in a second or third nucleon-nucleon collision as a first. Only one \bar{p} can be created per event. The normalization of the output of the model was tested to make sure that it predicted a total inelastic cross section for the target that agreed with data.

In accordance with these guidelines the following parameters were set:

The nucleon-nucleon inelastic cross section was set to 30.24 mb for the 18.56 GeV/c beam momentum and to 29.40 mb for 11.56 GeV/c proton beam momentum. These cross sections, with errors of ± 0.21 mb and ± 0.13 mb respectively, were derived from experimental data on the total and elastic cross sections for p-p collisions (30). The data were fit in a small enough beam momentum range so that a linear fit to the data would yield reasonable chi squareds.

Once the nucleon-nucleon inelastic cross section was set using the method in the last paragraph, the \bar{p} creation cross section was obtained from the parameterizations of $p - p \rightarrow \bar{p}X$ cross sections discussed previously in chapter 1 (12). The number was set to 0.061 mb. This number was obtained by choosing a value midway between the values given by the two parameterizations. The two parameterizations differed by 0.002 mb. It could be argued that the Costales parameterization is best suited to the E941 19 GeV/c p-A data, because that parameterization was developed using the Allaby data, which were taken at a similar beam energy. The difference between the two parameterizations is quite small, however, so the point is not very important.

The kinematics for the created \bar{p} 's were chosen to fit spectra for \bar{p} 's created in p-p collisions at similar energies (17). This resulted in \bar{p} 's fit to a Gaussian in rapidity with mean at mid-rapidity ($y = 1.85$) and a σ of 0.51, and an exponential in transverse momentum with a temperature of 120 MeV (12). These numbers were obtained from reference (12), in which the p-p data collected in Reference (17) were analyzed. Allaby's inverse slopes turned out to be between 110-130 MeV. Plots of the input distributions to the model as a function of rapidity and transverse momentum are shown in Figs. 5.1 and 5.2.

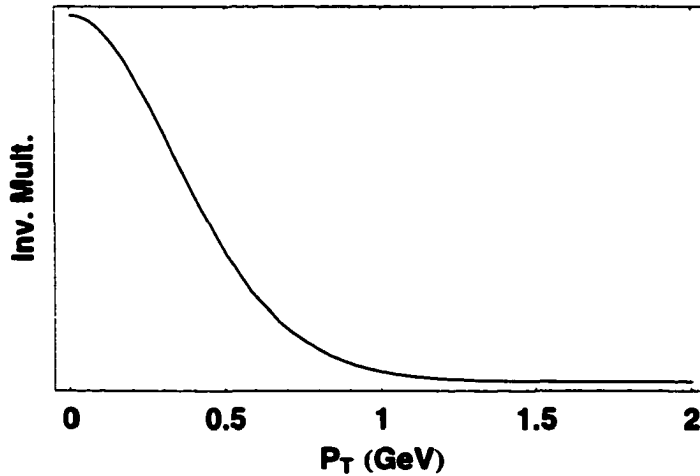


Figure 5.1 Primordial distribution of \bar{p} 's in transverse momentum. The inverse slope parameters were taken from Allaby data.

As for the target nuclei, the nucleons in beryllium were distributed according to a modified

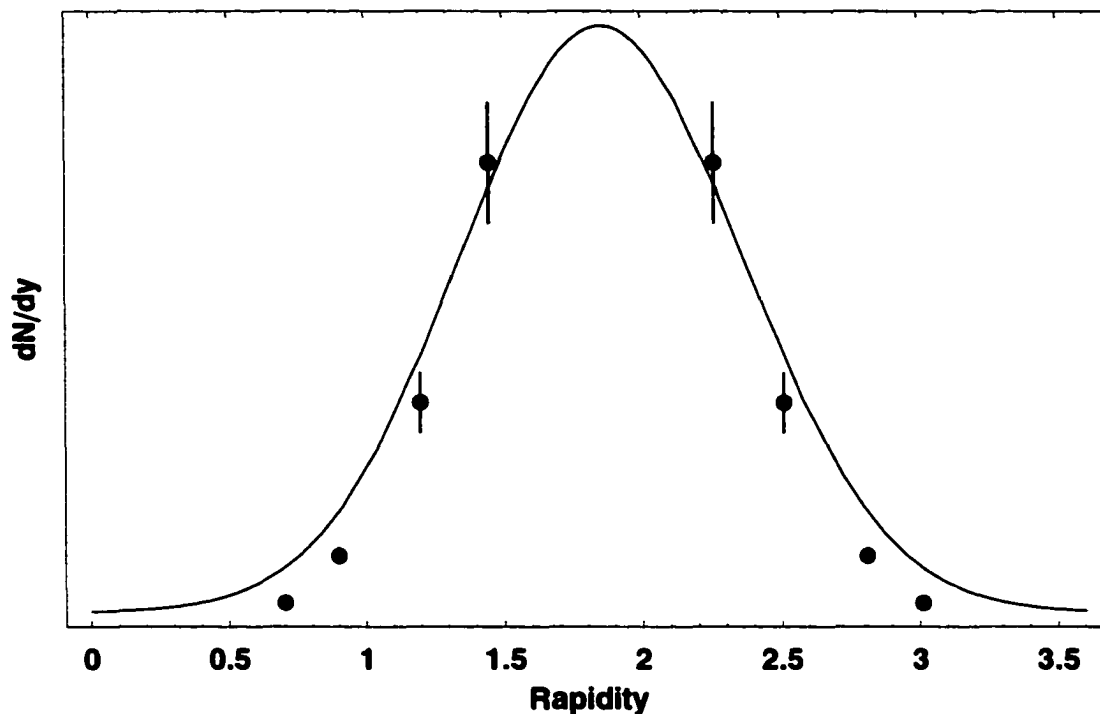


Figure 5.2 Primordial distribution of \bar{p} 's in rapidity. Fit to E802's estimate of Allaby's dn/dy distributions. The points are the estimates of dn/dy from Allaby.

Gaussian, while those in the lead were distributed according to a three parameter Fermi distribution (31). When shooting projectiles at these nuclei, the maximum impact parameters were set to 4 fermis above a 'maximum inelastic' impact parameter given by Ref (34). For beryllium, this turns out to be 6.649 fm, and for Pb the maximum impact parameter was 12.105 fm. In choosing these numbers, it was, of course, important to make sure that the entire nucleus was sampled while avoiding too many instances in which the incoming projectiles didn't interact.

As mentioned above, to test the reliability of the algorithm that created the \bar{p} 's and counted the number of inelastic collisions, the algorithm was used to calculate the total inelastic cross section of the target nuclei. In the context of the model, an inelastic collision was defined to be one in which at least one nucleon-nucleon collision occurred per incident proton. The number of inelastic collisions divided by the number of incident protons times the cross-sectional area sampled is the inelastic cross section. The results were encouraging and increased my confidence in the method (See Table 5.1). The Monte Carlo simulation was able to reproduce the total

Table 5.1 Model calculated total inelastic cross sections as compared to those found in the literature.

Target	$\sigma_{inelastic}$ model	Reference (32)	Reference (33)
Be	190 mb	180 mb	
Pb	1,700 mb	1692 mb	1730 ± 52 mb

inelastic cross section of the beryllium and lead nuclei.

Now that the N-N inelastic cross section, the \bar{p} creation cross section (in N-N collisions), and the distributions of nucleons in the nucleus were set, random impact parameters over a constrained region were chosen. If the projectile came close enough (where "close enough" was set by the \bar{p} creation cross section") to a target nucleon, an \bar{p} was created. By keeping track of whether the projectile came close enough to any target nucleon for any kind of inelastic interaction as well, the model yielded the number of 'primordial' \bar{p} 's per inelastic collision.

In order to optimize the running speed of the code, a file was made containing 5000 configurations of proton impact parameter and target nucleon locations that would result in the production of \bar{p} 's. By keeping track of the number of inelastic collisions required to create these 5000 \bar{p} 's (for normalization), the same 5000 events could be used over and over again for various calculations without having to sample the millions of collisions necessary to obtain these 5000.

One interesting question that the model addresses is, "in the absence of annihilation, what is the overall ratio of primordial \bar{p} yields, Pb/Be?" The code predicted primordial yields of 2.98×10^{-3} per inelastic interaction for Be and 7.30×10^{-3} for Pb. This yields a Pb/Be ratio of 2.45. In the absence of annihilation, one would expect to see 2.45 times more \bar{p} 's per inelastic interaction in Pb than in Be. The fact that we see ratios between 0.5 and 0.8 suggest about 3.8 times more annihilation in Pb than in Be.

Having created \bar{p} 's, the next question was whether they made it out of the nucleus. By varying the \bar{p} annihilation cross section (when incident upon a nucleon), we found the annihilation rate for the entire nucleus. The way that this was accomplished was to vary the annihilation cross section until the model predicted the observed ratio of yields between lead and beryllium for each kinematic bin.

Table 5.2 \bar{p} -nucleon in medium annihilation cross section. The error bars of the experimental ratio are not carried through. The model prediction errors listed are simply the errors on fitting the particular experimental ratios to within 0.02.

Rapidity	Ratio (Pb/Be)	Cross section	p_T Range
1.4-1.6	0.593	30 mb	100-150 MeV
1.6-1.8	0.725	23 mb +1	100-150 MeV
1.8-2.0	0.647	27 mb \pm 1	100-150 MeV
2.0-2.2	0.419	47 mb +1	100-150 MeV
2.2-2.4	0.541	34 mb +2-1	100-150 MeV

Since 5000 \bar{p} 's were generated for each kinematic bin in y and p_T , the statistical error of the model was of the order of 1.5 percent.

In order to fit this model to our data, we adjusted only 1 parameter, the effective annihilation. We ran the model for each rapidity at a fixed transverse momentum for both the Pb and Be targets and adjusted the effective annihilation until the Pb/Be ratio matched the target dependence that we had observed experimentally. The results are summarized in Table 5.2.

The free space annihilation cross section for \bar{p} 's has been well measured and parameterized. For that matter, E910 has published an effective annihilation cross section in the nuclear medium. To see how the free space annihilation cross section compares to the effective annihilation cross sections measured by E941 and E910, see fig. 5.3. In this figure, two E941 models were used, one which allowed \bar{p} 's to be created after the first N-N collision of the projectile (model A) and one in which the \bar{p} 's could only be created in the first collision (model B). These 2 values bracket the E910 result, although the E941 result occurs at higher beam momentum. For this comparison, we used the yield of \bar{p} 's summed over our entire acceptance.

5.2 Modeling the Absolute p+Be Yield

Another simple model that can be constructed and compared to the p-Be is the creation of simulated invariant multiplicities using only the total \bar{p} creation cross section and the assumptions about the kinematic distributions for those \bar{p} 's used in the last section. The \bar{p} 's are again distributed as a Gaussian in rapidity and an exponential in p_T (with the same values for the

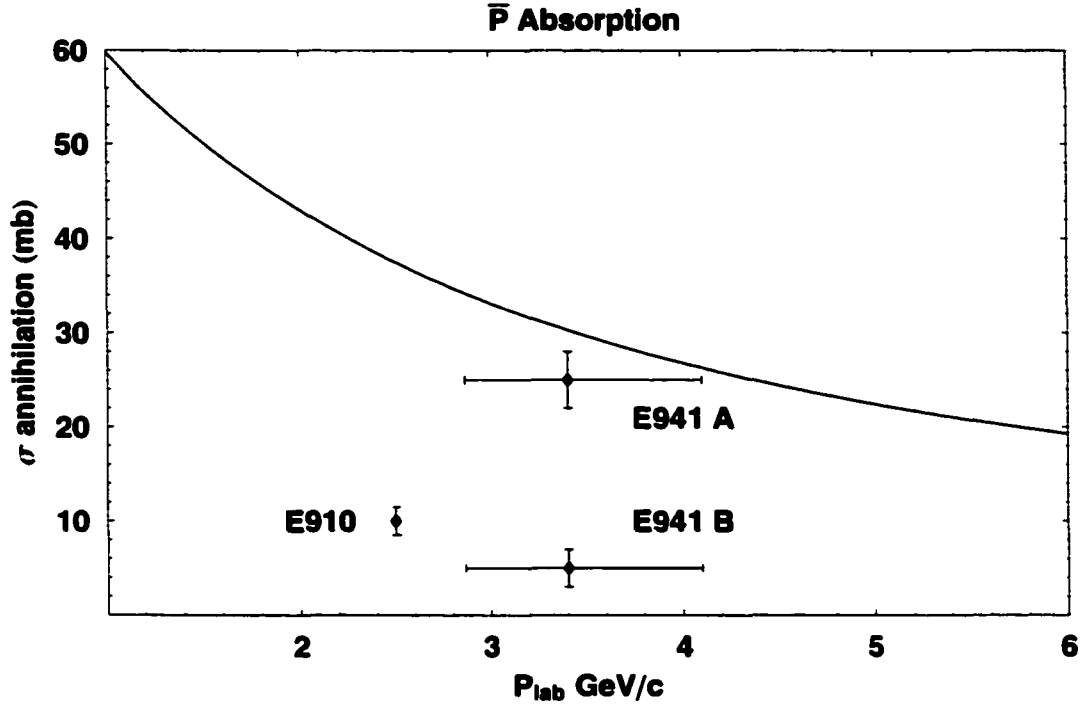


Figure 5.3 A parameterization for the annihilation cross section of \bar{p} 's in free space vs. that same quantity in nuclear matter. There are 2 E941 models employed. In the one with the greater annihilation cross section \bar{p} creation was allowed on collisions subsequent to the first collision of the incident nucleon. In the second, the \bar{p} could only be created in the first N-N collision.

parameters of these functions as described before), and from this, the invariant multiplicities matched to our phase space can be estimated. This is done in Fig. 5.4. In the figure, the model appears to float upwards with respect to the data. This is because the data for p-Be do not turn out to follow a Gaussian in rapidity (the choice for the model). The data vs. the model is plotted in Fig. 5.5. Here, the discrepancy between the Gaussian assumption in the p-p case and that of the p-Be data is notable. It begs the question, "what is happening to the higher rapidity \bar{p} 's one might expect to see?" The \bar{p} 's created in Be may be interacting with other target nucleons after they are created.

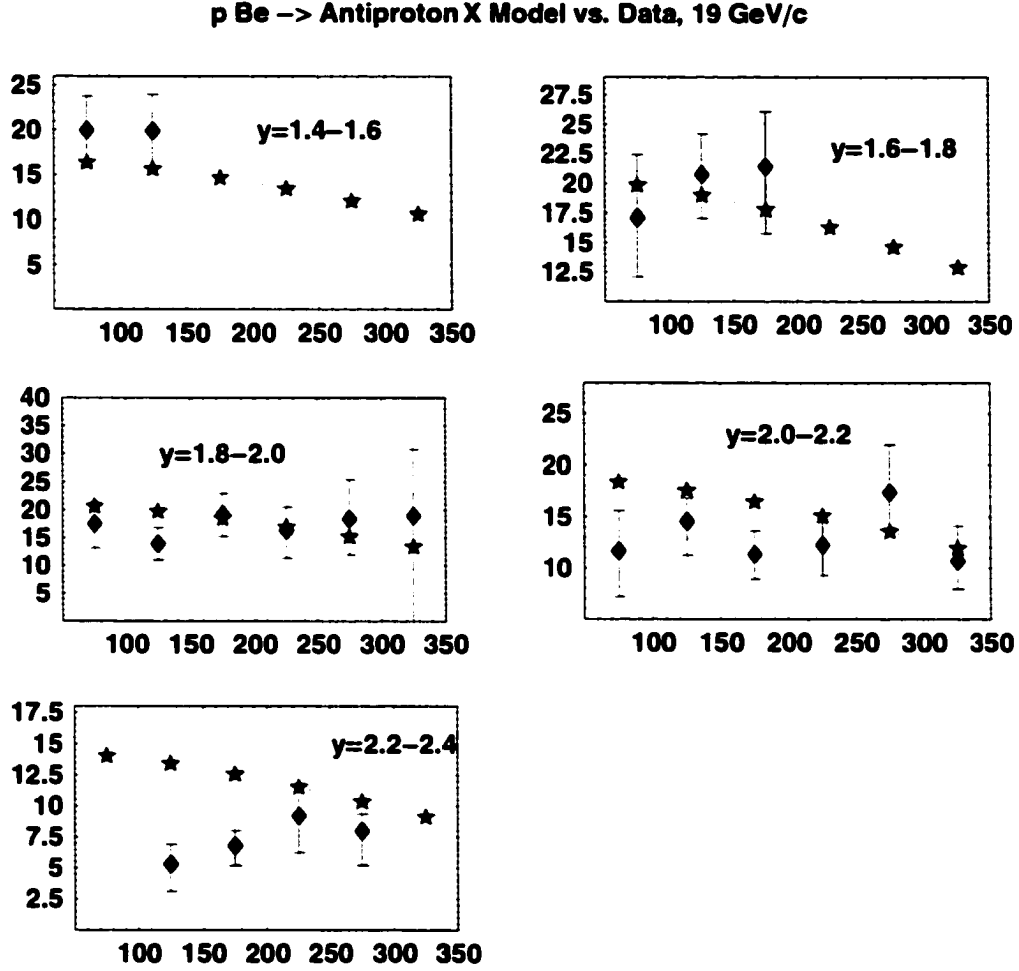


Figure 5.4 Model \bar{p} 's from p-p collisions compared to the actual E941 p-Be data at 19 GeV/c. Invariant multiplicity, $\frac{d^2\sigma}{\sigma_{inel}2\pi p_T dp_T dy}$, is plotted vs. p_T in MeV. The invariant multiplicities are multiplied by a factor of 10^4 . The agreement is quite good. The overall normalization of the model was obtained from Eqn. 1.17.

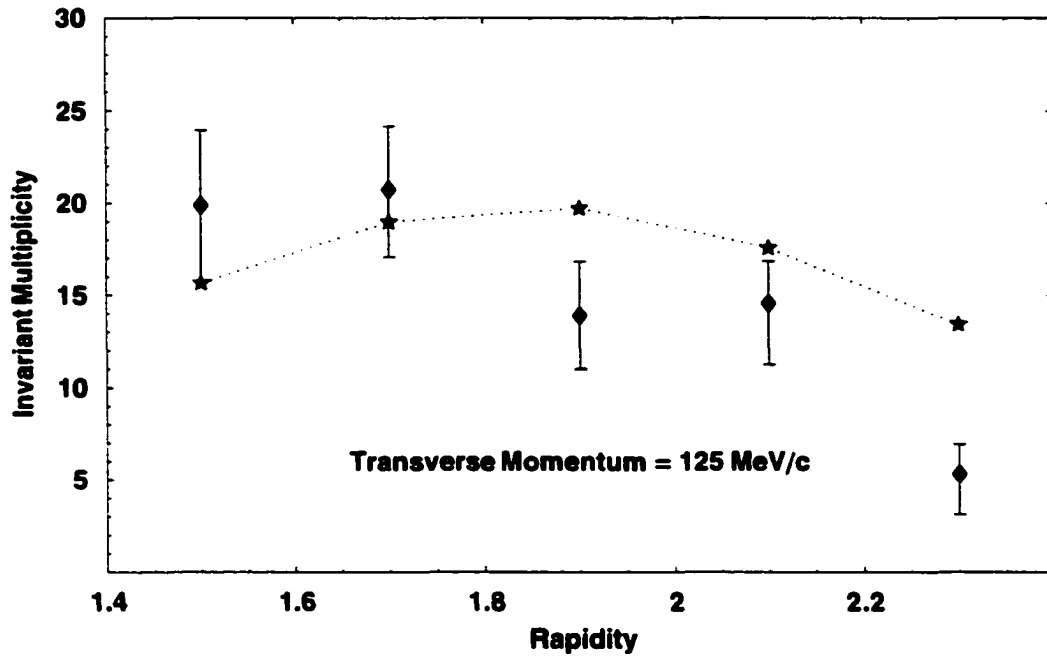


Figure 5.5 Model \bar{p} 's from p-p collisions compared to the actual E941 p-Be data at 19 GeV/c. Invariant multiplicity, $\frac{d^2\sigma}{\sigma_{inel}2\pi p_T dp_T dy}$, is plotted vs. y . Plotting the invariant multiplicities this way suggests that the Gaussian fit to rapidity may not match. The higher rapidity \bar{p} 's appear to be suppressed.

CHAPTER 6. DISCUSSION AND CONCLUSIONS

"I didn't go to evil medical school to be called 'Mister'" - Dr. Evil in Austin Powers

6.1 Energy Dependence.

As explained in the first chapter, E802 parameterized the \bar{p} creation cross section in p-p collisions as a function of the available center of mass energy, $\epsilon = \sqrt{s} - 4m_p$, where s is the total energy in the center of mass frame squared and m_p is the mass of a proton (18). The parameterization was developed using the Allaby p-p data in the range $6\text{GeV} < \sqrt{s} < 10\text{GeV}$. This parameterization was cited in chapter 1, Eqn. 1.17.

$$\frac{\sigma_{pp \rightarrow \bar{p}X}}{\sigma_{inel}} = (0.3696\epsilon + 0.2301\epsilon^2) \times 10^{-3} \quad (6.1)$$

In trying to explain their own Si+Al data using this parameterization with the ARC cascade model, E802 obtained abundances that were 30 percent higher than their p+Be data. Using their p+Be data to adjust the parameterization, they obtained eqn. 1.18.

$$\frac{\sigma_{pp \rightarrow \bar{p}X}}{\sigma_{inel}} = (0.3645\epsilon^2 + 1.478\epsilon^3) \times 10^{-4} \quad (6.2)$$

These parameterizations are plotted as a function of proton beam momentum in Fig. 6.1.

To measure the size of the energy scaling in the E941 \bar{p} data, p-Be collisions were used. These collisions are not identical to p-p, but in the Allaby data, at least, the difference between p-p yields and p-Be yields was quite small. For the Allaby p-p data, the integrated yields were estimated, but for E941, the question of which y and p_T bins to compare is relevant. I chose to scale the rapidity by beam rapidity $\frac{y}{y_{beam}}$ so that both the 19 and 12 GeV/c data would be

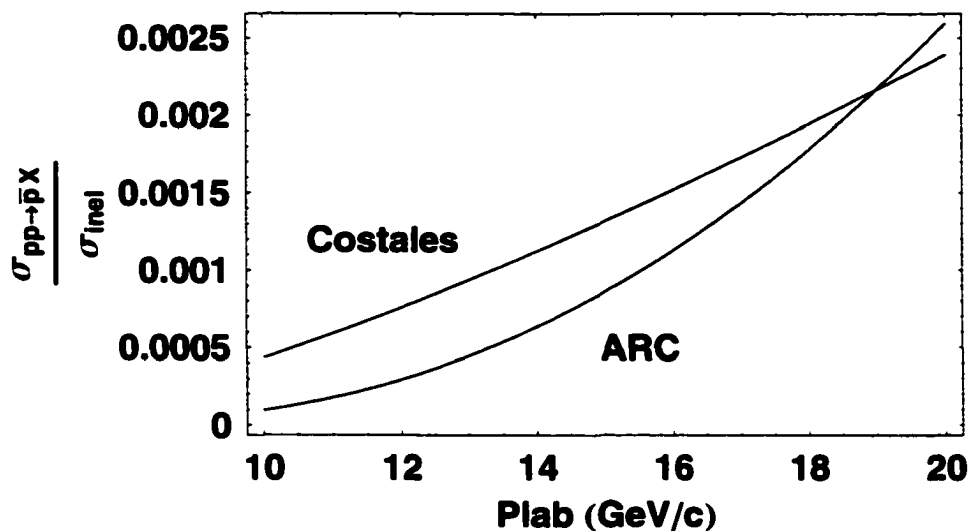


Figure 6.1 Two parameterizations of the energy scaling of the \bar{p} creation cross section in p-p collisions. Notice that these are given with the total inelastic cross sections divided out.

compared in terms of the fraction of beam rapidity. Choosing $p_T = 125$ MeV/c, the results are given in Table 6.1. Apparently, the E941 scaling favors the ARC parameterization, i.e., the parameterization which used the E802 p+Be data at 14.6 GeV/c beam momentum.

Table 6.1 Energy scaling for the \bar{p} cross section in E941 p-Be data, and the predicted scaling using Eqn. 6.1 and Eqn. 6.2. Due to some uncertainty in the E941 beam momentum, scaling for both 12 GeV/c to 19 GeV/c and 11.5 GeV/c to 19 GeV/c are given. Since E941 does not measure the cross section but rather the differential cross section, the E941 data were compared at $\frac{y}{y_{beam}} = 0.57$, and $p_T = 125$ MeV/c for both the 19 and 12 GeV/c beam data.

Source	$\frac{19}{11.56 \pm 0.5}$	19/12	19/11.5
E941	6.94		
Arc		7.34	9.32
Costales		2.86	3.22

6.2 Target Dependence in p-A.

In Fig. 6.2, we plot the \bar{p} yields from three targets using the 19 GeV/c proton beam. These are plotted as a function of rapidity at fixed transverse momentum for the Pb, Cu, and Be targets. The plot indicates that there is some target dependence. The Be invariant multiplicities are largest and the Pb invariant multiplicities are smallest. The Cu invariant multiplicities tend to fall somewhere in between (within experimental errors) as expected. The target dependence is quantified in Fig. 6.3. In this figure, the ratio of invariant multiplicities, Pb/Be, is plotted as a function of rapidity. The error bars represent both the statistical error and the systematic error from the fit. Even with large error bars, the plot drives home the point that no matter how one looks at it, the ratios are less than one. E802 had reported no target dependence, while E941 reported a modest target dependence. The Allaby data, however, shows no target dependence at low rapidity, but a modest target dependence at high rapidity. Therefore, the Allaby data tends to suggest that the target dependence is a function of rapidity. E802 measured at low rapidity, and their finding of no target dependence was consistent with Allaby in that kinematic range. E941's acceptance was maximized close to mid-rapidity and measured modest target dependence, as did Allaby (and E910). Although one can draw no conclusions from the E941 data regarding rapidity dependence, given the target dependence of each of the various experiments as a function of rapidity, rapidity dependence would reconcile the results. If this dependence turned out to be real, it would be difficult to explain because one expects that the \bar{p} annihilation would become much weaker at higher rapidities, causing the ratios to increase. One possible explanation is that the \bar{p} often scatters without annihilating in the nucleus and thus is shifted to lower rapidities.

Nevertheless, in the case of the E941 measurement, the fact that the overall ratio of invariant multiplicities is less than one over the entire coverage of the experiment reflects that annihilation is the dominant feature of the ratios. In fact, the model analysis in the last chapter produced a Pb/Be ratio of not 1, but 2.45 for the \bar{p} 's before consideration of annihilation.

If one were to assume that \bar{p} creation scales with the number of nucleons in the nucleus, then it must be concluded that the ratio of invariant multiplicities is greater than one before

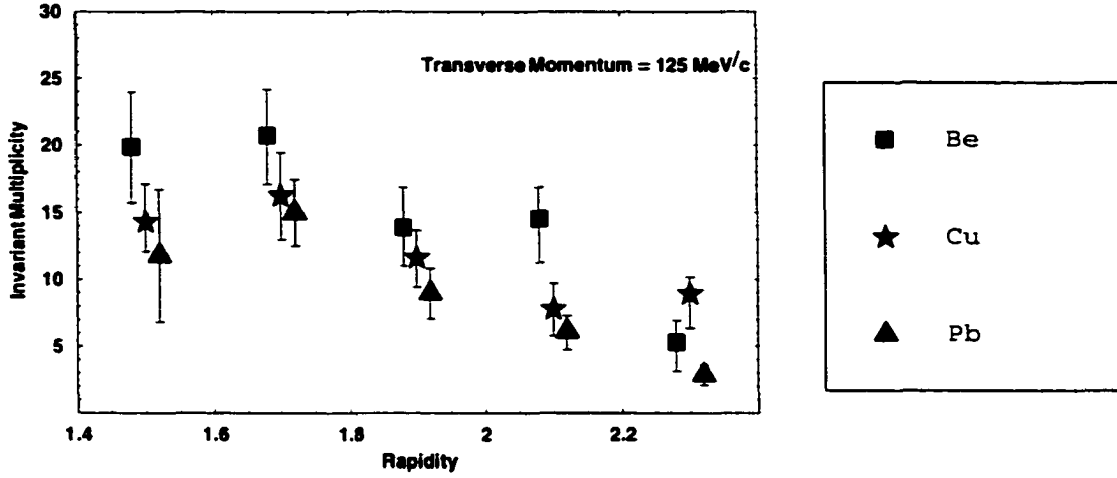


Figure 6.2 Invariant multiplicities for Pb, Cu and Be targets as a function of rapidity at fixed p_T of 125 MeV/c. The beam momentum for all three targets was 19 GeV/c.

annihilation because the invariant multiplicities are divided by the total inelastic cross section which is proportional to $A^{2/3}$, not by the number of nucleons, A . Invariant multiplicity ratios that obeyed such scaling would be greater than one. A Pb/Be ratio as great as one still corresponds to considerable annihilation. The question is how much?

Despite the conclusion that a Pb/Be ratio of one represents a situation in which there is considerable annihilation, the modeling in the last chapter suggested that the annihilation cross section of \bar{p} 's may be suppressed in the nuclear medium. Using a model that allowed the \bar{p} 's to be created after the initial nucleon-nucleon collision gave results that approached the free space annihilation cross section, but allowing \bar{p} production only in the first nucleon-nucleon collision yielded effective annihilation cross sections that were lower than the free space annihilation cross section. E910 also derived an in-medium annihilation cross section that was considerably below that of free space.

6.3 Antiproton Production and Annihilation in A-A.

In the first chapter, it was stated that one of the things that p-A collisions might illuminate is the question of whether the effects of increased production win out over the effects of

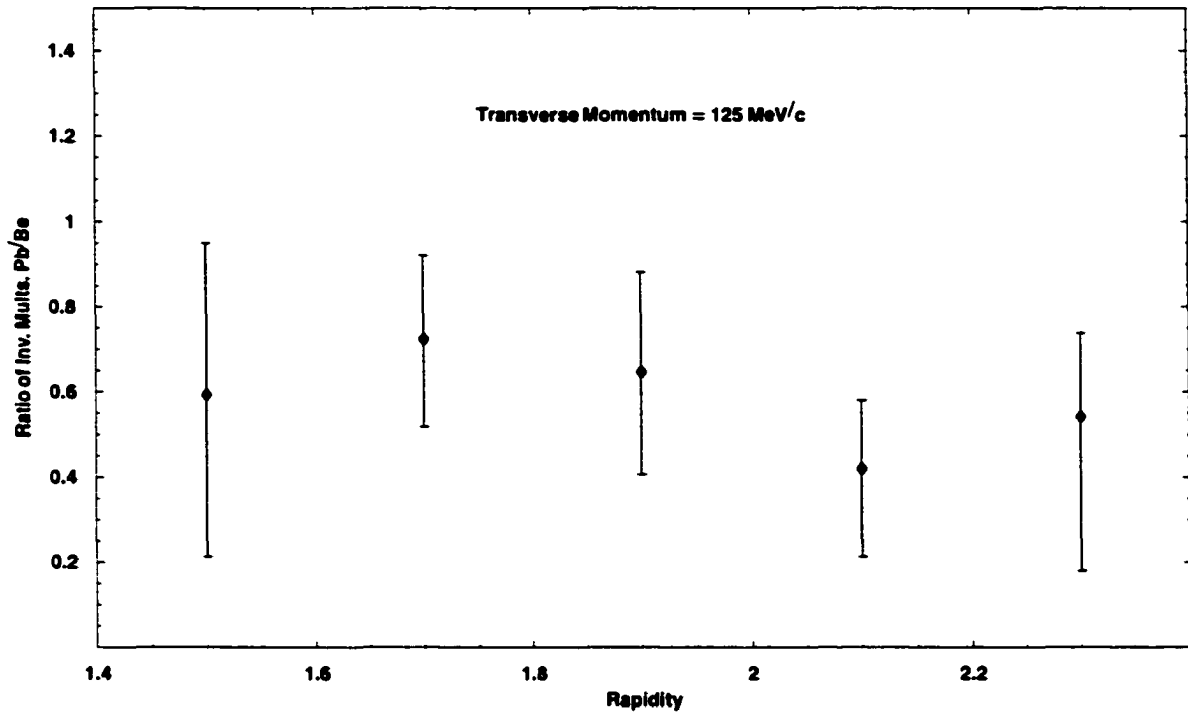


Figure 6.3 Ratio of \bar{p} invariant multiplicities Pb/Be. The data are presented as a function of rapidity. The beam momentum for all three targets was 19 GeV/c, and the transverse momentum for each data point is 125 MeV/c. The error bars include both statistical and systematic contributions. The data are consistent with an Pb/Be ratio that is at most one, and in all likelihood less than one.

increased annihilation in the A-A scenario. A convenient way to make this comparison would be to compare the E864 A-A data to the E941 p-A data. One virtue of this comparison is that both sets of data were taken with the same detector, so many of the possible sources of systematic error are avoided.

In the p-A regime, we noticed that as the target got bigger, there was a decrease in the \bar{p} yields, and we attributed this to the effects of increased annihilation. When we compare to the A-A data, we do not, to the precision of the data, see this trend. In Fig. 6.5, E941 p-A data at 19 GeV/c are plotted in the top panel, and E941 p-A and E864 A-A data, at 12 and 11.6 GeV/c respectively, are plotted in the bottom panel. The E864 data is broken up into 4 centrality bins: 0-30%, 30-70%, 70-90%, and 90-100%. The 0-30% bin is for the most peripheral collisions and the 90-100% bin is for the 10% most central. The data for each centrality bin are divided by the mean number of estimated first collisions for that bin, so the Au-Au numbers are scaled by the estimated number of first collisions. To the extent that one can draw a flat line through all the points, first collision scaling is obeyed. Again, to the precision of the data, first collision scaling appears to be obeyed. The largest source of error in the Au-Au data is the error associated with the model estimation of the number of first collisions.

If the measured particle had been K's or π 's, one might have expected the first collision scaling, because no target dependence for the production of these particles is observed in p-A. This is shown in Fig. 6.4 using p-A data for the production of these particles from another experiment. The \bar{p} 's are the only particles that show target dependence, perhaps due to their high annihilation cross section.

The significance of Fig. 6.5 is difficult to ascertain given the size of the error bars. If they were smaller and one took the downward trend of the first three points seriously, then it seems that some particular enhancement mechanism kicks in as the A-A collisions become more central, such that whatever annihilation is taking place is balanced by the level of enhanced creation and first collision scaling is maintained. This conclusion can not be maintained, however, due to the lack of precision in the data.

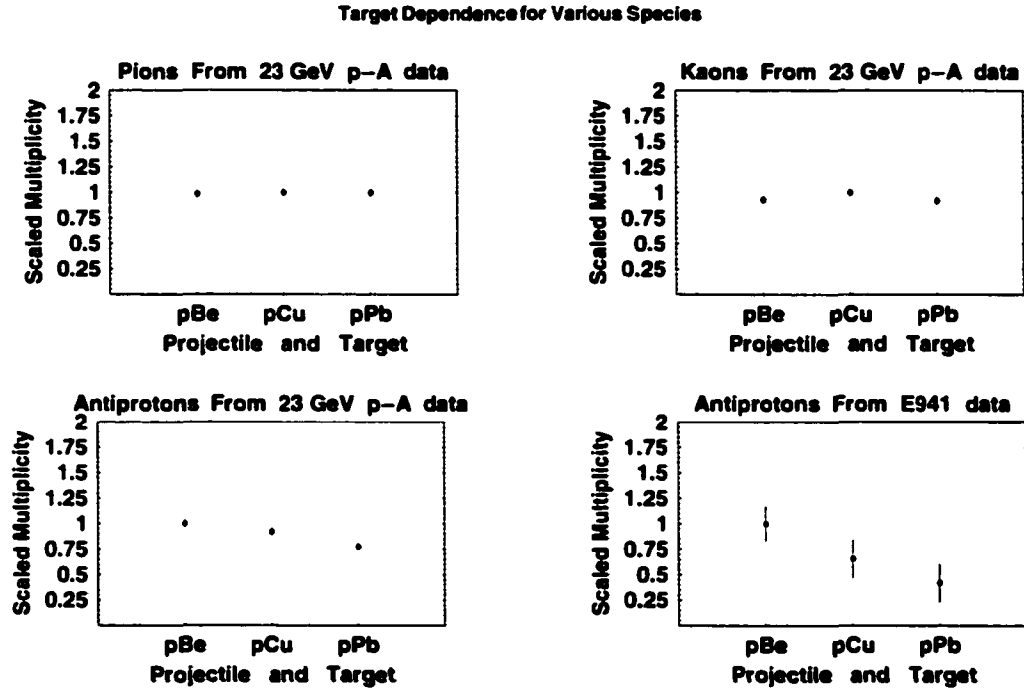


Figure 6.4 Comparison of the production of other species of particles in p-A collisions to the production of \bar{p} 's. These data were taken from Reference (22) and from E941. In the plots there is no target dependence in the π spectra or K spectra, but \bar{p} 's show at least a small target dependence in both the Eichten data and E941.

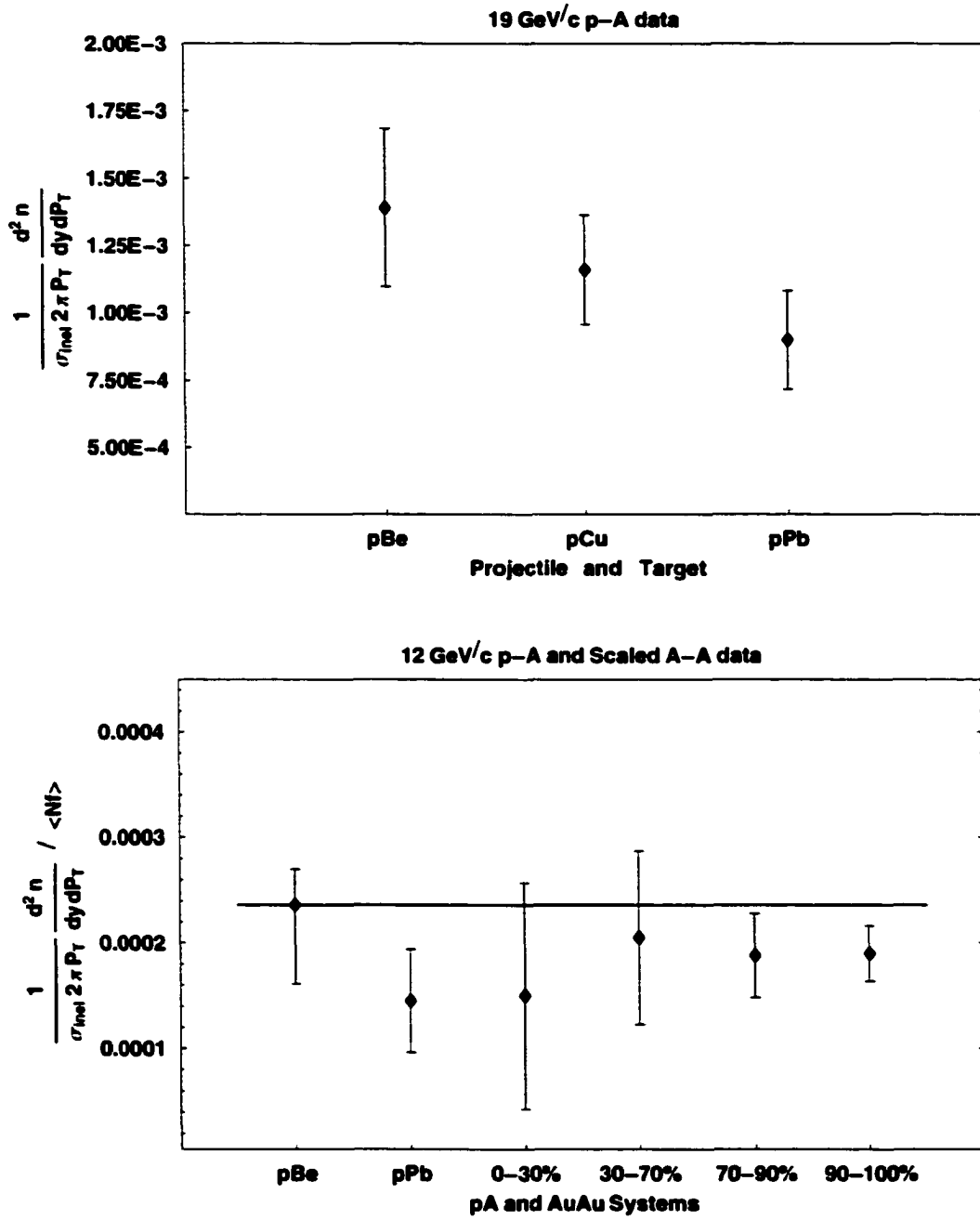


Figure 6.5 On the top panel, the target dependence of the invariant multiplicities for \bar{p} 's produced in p-A collisions is shown. Below that, the invariant multiplicities for p + several targets is compared to Au+Au collisions in 4 centrality bins. The Au-Au data are divided by the estimated number of first collisions. The plots are for data at $y=1.9$ and $p_T = 125 \text{ MeV}/c$

6.4 Conclusions

\bar{p} invariant multiplicities have been measured using 19 GeV/c protons incident on Be, Cu, and Pb, and 12 GeV/c protons incident on Be and Pb. There is strong energy dependence that is well described by previous parameterizations of the \bar{p} production cross section, and moderate target dependence. The yields measured for p-Be collisions match up well with estimates from previous p-p data and reasonable assumptions about the shape of the distributions. The target dependence is modest, but the model used in this analysis, however, seems to indicate that even modest target dependence indicates that a great deal of annihilation is taking place in the heavier target. On the other hand, the annihilation is not as great as one would expect using the free space annihilation cross section and a simple geometric model (at least under the assumption that \bar{p} 's are created after the first nucleon-nucleon collision. Suggestions that screening mechanisms shield the \bar{p} 's or that changes in the mean fields enhance \bar{p} creation as the target increases in size are not ruled out from the data. The apparent enhancement in yields in the p-A regime only becomes more evident as one goes to the A-A regime and discovers that first collision scaling for the \bar{p} 's is apparently obeyed. The possibility of additional enhancement mechanisms or suppression of annihilation must again be considered.

BIBLIOGRAPHY

- [1] O.W. Greenberg, *Quarks: Resource Letter Q-1*, Am. J. Physics, 50 (1982) 1074-1089.
- [2] T.D. Lee., *RHIC and QCD: An Overview*, Nucl. Phys. A, 590 (1995) 11c-28c.
- [3] J.B. Kogut, *Quark Matter '83: Conference Summary of Theory*, Nucl. Phys. A, 418 (1984) 381c.
- [4] R. Hagedorn, *Statistical Thermodynamics of Strong Interactions at High Energies*, Nuovo Cimento Suppl., 3 (1965) 147-186.
- [5] T.D. Lee, G.C. Wick, *Vacuum Stability and Vacuum Excitations in a Spin 0 Field Theory*, Phys. Rev. D, 9 (1974) 2291.
- [6] T.D. Lee, *A Possible New Form of Matter*, Report on the Workshop of BeV/nucleon Collisions of Heavy Ions and Why, Bear Mountain (1974 BNL No. 50445.1)
- [7] Gross, Pisarski, Yaffe, *QCD and Instantons at Finite Temperature*, Reviews of Modern Physics, 53, 43 1 (January, 1981).
- [8] Alford, Bowers, Rajagopal, *Crystalline Color Superconductivity*, Phys. Rev. D, 63, 074016 (2001).
- [9] Rajagopal, *Mapping the QCD Phase Diagram*, Nucl. Phys. A, 661 (1999) 150-161.
- [10] Shor *et al.*, *A Measurement of 'Subthreshold' Production of K^- , and Antiprotons in Relativistic Nuclear Collisions*, Phys. Rev. Lett., 48, 159 (1982).

- [11] P. Koch, C.B. Dover, K^\pm , \bar{p} , and Ω^- *Production in Relativistic Heavy-Ion Collisions*, Phys. Rev. C, 40, 1 (July, 1989).
- [12] T. Abbott *et al.*, *Antiproton Production in $p+A$ Collisions at 14.6 GeV/c* Phys. Rev. C, 47, 4 (April, 1993) R1351.
- [13] S.H. Kahana, Y. Pang, T. Schlagel, C.B. Dover, *Antiproton Production from Heavy-Ion Collisions at 14.6 GeV/c*, Phys. Rev. C, 47, 4, (April, 1993) R1356.
- [14] Jahns, Spieles, Stöcker, Joiner, “*Antiflow*” of Antiprotons in Heavy Ion Collisions, Phys. Rev. Lett., 72, 22 (1994).
- [15] L.D. Landau and E.M. Lifshitz, *Classical Theory of Fields, Fourth Revised English Edition, Course of Theoretical Physics, Volume 2*, Published by Butterworth-Heinenann (1975) Reprinted with Corrections (1999)
- [16] C.B. Dover, T. Gutsche, M. Maruyama, and A. Faessler, Prog. Part. Nucl. Phys. 29, 87 (1992)
- [17] J.V. Allaby *et al.*, *High-Energy Particle Spectra from Proton Interactions at 19.2 GeV/c*, CERN report No. CERN 70-12 (1970).
- [18] J. Costales, Ph.D. Thesis, MIT (1990), unpublished.
- [19] U. Amaldi *et al.*, Nucl. Phys. B86, 403 (1975).
- [20] C. Spieles, M. Bleicher, A. Jahns, R. Mattiello, H. Sorge, H. Stöcker, and W. Greiner *Antibaryons in massive heavy ion reactions: Importance of potentials*, Phys. Rev. C, 53, 2011 (April, 1996).
- [21] I.G. Bearden *et al.* *Proton and antiproton distributions at midrapidity in proton-nucleus and sulphur-nucleus collisions* Phys Rev C, 57, 2 (February, 1998)
- [22] Eichten *et al.*, *Particle Production in proton Interactions in Nuclei at 24 GeV/c*, Nucl. Phys. B, 44 (1972) 333-343.

- [23] T.A. Armstrong *et al.*, *Search for strange quark matter produced in relativistic heavy ion collisions*, Phys. Rev. C, 63, 054903
- [24] J. Hill for the E864 Collaboration, *Search for strange quark matter*, Nuclear Physics A **675**, 226c-229c (2000)
- [25] T.A. Armstrong *et al.*, *A Spectrometer for the Study of High mass Objects Created in Relativistic heavy Ion Collisions*, Nucl. Instr. and Meth. A, 437 (1999) 222-246.
- [26] K.N. Barish *et al.*, Nucl. Instr. and Meth. A **406**, 227 (1998)
- [27] John Lajoie, Doctoral thesis at Yale University, June (1997).
- [28] LeCroy Corporation, *PCOS4 Models 2748CAM Quad Stream Controller and Model 2749CAM PCOS4 System Driver* user's manuals.
- [29] LeCroy Corporation (700 Chestnut Ridge Road, Chestnut Ridge, NY 10977-6499), operators manuals for the 1881 and 1881M 64 channel Fastbus ADC, and for the 1872A Fastbus time-to-digital converter.
- [30] The European Physical Journal C, Volume 3, Number 1-4, 1998. Web page: <http://pdg.lbl.gov/xsect/contents.html>. The numbers were updated for the year 2000.
- [31] Barshay, Dover, and Vary, *Nucleus-nucleus cross sections and the validity of the factorization hypothesis at High Energies*, Phys. Rev. C, 11, 2 (1975) 360.
- [32] D. Dekkers *et al.*, *Experimental Study of Particle Production at Small Angles in Nucleon-Nucleon Collisions at 19 and 23 GeV/c*, Physical Review, **137**, 4B, B962-B978 (1965).
- [33] A.S. Carroll *et al.*, *Absorption Cross Sections of π^\pm , K^\pm , p and \bar{p} on Nuclei Between 60 and 280 GeV/c*, Physics Letters, 80B, 3 (1979) 319-322.
- [34] Benesh, Cook, and Vary, *Single Nucleon Removal in Relativistic Nuclear Collisions*, Phys. Rev. C, 40, 3 (1989) 1198.

ACKNOWLEDGEMENTS

I never would have gone to college and therefore would never have pursued a graduate career were it not for the unbelievable kindness and generosity of Ute and Roy Tellini. They paid for my education at Grinnell college (one of the more expensive liberal educations in the country) and gave me every opportunity that is now before me. I could never thank them enough, and they have my eternal gratitude. There are two other things that they have given to me which I value even more highly. First, their love, and second, an example of the sort of life people can live when they are at their best.

I would also like to thank two 'Johns' for their help. John Hill and John Lajoie. Professor Hill has been something of an anchor to me in this research. Many times, when I was lost in daydreams he would me down to earth by asking simple questions that focused my thinking. He has always been practical where I am not, and his insistence on being concrete has helped me to finish this thesis so quickly – or rather, at all. John Lajoie gave me most of the code that allowed me to conduct this analysis, and a great deal of help in both understanding technical details in the analysis and the physics. I am extremely grateful to him for his time and consideration, and attribute the fact that he was forced to interact with someone as disorganized, scattered and undisciplined as me to bad karma on his part. He must have done something unconscienably bad to another person in a previous life, and his punishment was having to deal with me in this one.

My two main collaborators in E941, An Tai, and Andrew Rose have been a real pleasure with whom to work. As the senior physicist amongst us, An Tai set a great standard for Andrew and I, both in his work ethic, and his competence as a physicist. He taught me a lot. In addition, the three of us had many very enjoyable conversations about both physics and

topics having nothing to do our profession (Andrew, I apologize for anything I ever might have said in any of those conversations that was obnoxious– what can I say, it comes far too easily to me).

There are many other people in the collaboration who gave a great deal of their time to help me understand the experiment. In particular, Zhangbu Xu, Evan Finch, Gene Van Buren, Nigel George, and Tim Miller all went above and beyond with their help.

I am also indebted to other senior physicists in the collaboration: Huan Huang, Dick Majka and Jack Sandweiss. Huan has always been both kind and gracious, Dick has suffered every stupid question I've ever posed to him with patience and forbearance, and Jack sets an example that I, for one, could never hope to follow – so I'm glad that there are people like him out there, so that we as a community can go places and learn things we might never have been able hope for otherwise.

At Iowa State University, Craig Ogilvie, who arrived later in my graduate student years has been a great motivator and a great help. I have also benefitted from Marzia Rosati's intelligent insights and comments.

A recent roommate and current friend, Jong Woo Kim, has always been a great friend, and a great person with whom to discuss physics.

Nathan Grau is a newer grad student in the Iowa State group, and he has also helped me quite a bit, particularly with running UrQMD simulations. I am in his debt. The other officemates I've had, Paul, and Robert Hoversten also helped me a lot – Robert at the beginning of this research and Paul at the end.

On a more personal note, I would like to thank my best friend, Dan Wesson. A life without Dan would have infinitely less colorful. If laughing and having fun are two of the main gifts that life has to offer, then I owe a great deal of whatever joy I have had to this friendship. It means the world to me.

In addition, I'd like to thank my brother and sister for all their love and support (and thanks for the winter jacket this year Paul). I love you both with all my heart.

I'd also like to thank Sara Quinn for all her love and support here at the end of the process, both with this thesis and in life in general.

Finally, there are the two people to whom I have dedicated this thesis, my mother and my daughter. I am grateful for the past that my mother has so enriched and the future that my daughter has yet to encounter.